From stock to floc: an investigation into the
physical/chemical processes controlling
aluminum sulfate and polyaluminum chloride
behavior in a gravity powered drinking water
treatment plant

Karen Alison Swetland

August 22, 2012

Abstract

Coagulation and flocculation processes have been utilized in municipal scale drinking water treatment plants for many decades. Coagulation mechanisms have been defined and flocculation parameters have been tested in many studies. However, this knowledge has not been successfully aggregated into an overarching theory of coagulation and flocculation that can be applied to the design, construction, and operation of drinking water treatment plants. To this end, a prototype chemical dose controller was designed and tested to be used in conjunction with a linear flow meter for the accurate and consistent dosing for coagulant chemicals into the influent water in a plant. Scalable, physically based algorithms for the automated design of the flow meter and dose controller are available online at *aguaclara.cornell.edu.*

A bench-scale water treatment plant apparatus with a hydraulic flocculator was created and validated to quantify flocculation performance for a wide array of conditions. Extensive data processing was also carried out to characterize the sedimentation of the flocculated suspensions. This powerful combination of bench-scale reactors and data analysis was used to study the rate of formation of PACl aggregates upon mixing with influent water and the effect of aggregate size on the subsequent formation of flocs that can be readily removed by sedimentation. Results show that, under the experimental conditions tested in this research, PACl self-aggregation consistently lowers attachment efficiency of the colloidal suspension, reduces the effectiveness of the flocculator, and reduces turbidity removal. Optimal performance is best accomplished by immediate, rapid, and efficient mixing of PACl with the influent water.

Mechanistically-based scalable algorithms for design and performance of hydraulic flocculators were developed in another study based on observations of residual turbidity for a range of influent turbidities ($5 - 500\,NTU$) and coagulant doses ($0.01 - 0.15\,mM$), for two hydraulic residence times ($800\,s$ and $1200\,s$) and for two coagulant types (polyaluminum chloride and aluminum sulfate). Seemingly disparate results were unified through creation of a composite design parameter that considers collision potential in the flocculator and coagulant surface coverage of colloids. When calibrated properly to the coagulant and source water to be treated, the predictive model is expected to be a powerful tool in the design and operation of hydraulic flocculators.

Biosketch

Karen graduated from Cornell University in August 2012 with her Ph.D. in environmental processes from the School of Civil and Environmental Engineering. She has been playing with the women's water polo team and working with the AguaClara program since beginning her doctoral work in 2009. She leaves the team in Mario's capable hands after two consecutive state championships and one glorious win at nationals. Her time with AguaClara can easily be characterized by cupcakes, research reports and one frustratingly fragile glass column. After receiving a teaching assistantship from the school, all it took was one creepily intense email to Monroe Weber-Shirk to secure her position in the AguaClara program.

Karen prepared for her graduate work by attending Vanderbilt University in Nashville, Tennessee where she earned a Bachelor of Science degree in Civil Engineering and a Master's of Science degree in Environmental Engineering in four years. If you haven't noticed, Karen doesn't waste any time. However, an unfortunate side effect of her accelerated undergraduate career, she is unfamiliar with many liberal arts topics and thus is terrible at Jeopardy. Life is full of compromises.

Before attending Vanderbilt, Karen hung out in the main loggia of Cooper City High School. She wanted to join the math club but her mother wouldn't let her, citing that "we know you're good at math, go do something different. Join the water polo team with your sister." This, as it turns out, was excellent advice.

Karen began her formal education at Pines Lakes Elementary, where she read every note her teachers asked her to deliver and ran in the halls when no one was looking. She was never caught for either offense.

Dedication

I dedicate my doctoral dissertation to my grandfather, William Wade, Cornell CEE Class of 1949. He taught me the importance of life-long learning and the joy of inventing new things that was, and will continue to be, crucial to my success.

Acknowledgments

I acknowledge the inspirational instruction and guidance of Dr. Monroe Weber-Shirk; his tireless imagination and unwavering faith in me and my research helped me push through the rough spots. I must also thank Dr. Len Lion for keeping me grounded in defensible science and for making coffee addiction seem normal. Special thanks to my minor advisors, Dr. Jim Bisogni and Dr. Stephan Schmidt, for providing important context for my work through their distinct expertise.

My time at Cornell was made so enjoyable by my involvement in the AguaClara program. I sincerely thank the students whom I was privileged to teach and from whom I also learned much. I expect great things from all of you, as I always did in class. Do good work and do it often.

Special thanks to Paul Charles and Tim Brock who have solutions for every problem.

To my fellow labmates: Matthew Higgins, Mathew Hurst, Craig Bullington, Drew Hart, Alex Krolick, Tori Klug, Mickey Adelman, and many more, your welcome distractions kept me laughing. Your dedication to AguaClara inspires me.

To my teammates on the women's water polo team: I will never forget our many victories in the pool and our friendships on land. I am honored to have been your goalie.

To my roommates: you're the best support system a girl could have, may the iHOB live on!

To my life long friends: Mike, Christine, Stefanie, Robbie, and Patrick, I value our friendships, and look forward to visiting each of you wherever you are for the rest of our lives.

To my brother and sister: Kristy and Scott, thanks for reminding me that normal people don't want to go to the library.

To my parents: your constant support and faith in me made all of this possible. Thank you for everything.

To Dale: your unflappable demeanor in the face of every research setback kept me moving forward. I am so grateful for your persistence and support; I would have never finished this research in record time without your motivation.

Contents

List of Tables

List of Figures

Chapter 1

Introduction

This research was completed as part of the AguaClara program at Cornell University. AguaClara at Cornell researches and designs sustainable, robust, gravity-powered, municipal-scale drinking water treatment plants. Prominent among the group's many accomplishments to date are the eight AguaClara-designed water treatment plants serving 27,000 people in Honduras. In accordance with the design philosophy, the research presented here was motivated by the need for scalable, optimized treatment processes that are based on defensible science and that are fully functional in the field. While other researchers have focused on particular conditions or theories, strong links to the field kept this research as broadly applicable as possible.

In chapter 2, the journey of a coagulant particle begins as it leaves the chemical stock tank at a water treatment plant and is accurately metered into the entrance tank with the help of two AguaClara inventions, the Linear Flow Orifice Meter (LFOM) and Linear Chemical Dose Controller (LCDC). These technologies have been developed and refined over several years out of necessity; there are no other devices available that meet the criteria in the design philosophy and provide accurate gravity-powered chemical dosing with minimal intervention on the part of the operator. The final designs for the LFOM and LCDC have been expressed in scalable algorithms which allow them to be defined and drawn in AutoCAD (in conjunction with all other treatment processes) by the AguaClara Automated Design Tool (ADT). This tool provides free engineering designs to anyone with an internet connection at *aguaclara.cornell.edu/design*.

In chapter 3, a laboratory scale water treatment plant apparatus is described. Frequently, jar tests are performed to study flocculation. Jar tests are batch systems with nonuniform energy dissipation rates where the only measurable performance parameter is the residual turbidity. The shortcomings of the jar test led to the development of the Flocculation Residual Turbidity Analyzer (FReTA). FReTA can continuously and non-destructively measure the turbidity of the particles that aggregate in a coiled tube flocculator upstream. FReTA also provides the ability to monitor floc settling velocity throughout sedimentation. The combination of non-destructive measurement and powerful computation

lends FReTA to be used in many possible coagulation and flocculation studies.

In chapter 4, FReTA was used to monitor the influence of PACl aggregate size on flocculation performance. When rapid mixing is insufficient to disperse the PACl, it will tend to self-aggregate at neutral pH instead of adsorbing to the surface of the colloids. This results in lower fractional surface coverage of the colloids and higher residual turbidities. These results also suggest that colloid surface coverage by coagulant, more than surface charge, determines the efficiency of flocculation.

In chapter 5, the idea of surface coverage is explored further as part of a predictive flocculation model. Two adjustable model parameters were fit to data from over 136 experiments, entailing 244,800 observations to create a model ($R^2 \approx 0.9$) that is applicable over a range of sedimentation tank capture velocities and that accurately reflects the effects of coagulant dose, raw water turbidity, flocculator residence time, and coagulant type. When calibrated properly to the coagulant and source water to be treated, the predictive model is expected to be a powerful tool in the design and operation of hydraulic flocculators.

Chapter 2

Gravity-Powered Chemical Dose Controller for Sustainable, Municipal-Scale Drinking Water Treatment

2.1 Abstract[1]

Accurate chemical dosing in water treatment plants is imperative to ensure optimal efficiency of flocculation and disinfection. Design algorithms, calibration techniques, and standardized components are presented for a linear flow orifice meter (LFOM) and a linear chemical dose controller (LCDC). These coupled systems allow water treatment plant operators to easily and reliably set and maintain the desired doses of coagulant and disinfectant. The combined system adjusts the chemical flow rate automatically in response to changes in plant flow rate to maintain the target chemical dose. The LFOM maintains a linear relationship between height of water in the entrance tank and plant flow rate. A lever and float are used to create a direct relationship between the plant flow and chemical flow produced by the LCDC. A linear relationship between head loss and chemical flow in the LCDC is created by using the major head loss through a small diameter tube to control the chemical flow rate. Experimental tests are described that minimize minor losses and verify performance of the LCDC.

---

[1] The contents of this chapter have been submitted to *Journal of Environmental Engineering*, with co-authors M.L. Weber-Shirk and L.W. Lion.

2.2 Introduction

The accurate application of coagulant prior to rapid mix and the addition of disinfectant after filtration are essential to the production of safe, clean drinking water at municipal drinking water treatment facilities. Reliable and easily maintained chemical dosing systems are vital. Many municipal water treatment plant chemical dosing systems rely on electronic supervisory control and data acquisition (SCADA) dose control systems to regulate the addition of coagulant and disinfectant. SCADA control systems are complex and require multiple interdependent technology platforms including sensors, signal convertors, microprocessors, software, and variable speed pumps. SCADA-type technology platforms also often rely on proprietary components and require a high level of technical expertise in each platform for maintenance. As a consequence, SCADA dose control systems have many failure modes and a significant number of the ensuing failures can require either replacement of specialized parts or the presence of highly trained technicians. These systems may be appropriate in facilities that have ready access to replacement part suppliers and that have financial capacity to pay the high labor costs for maintenance and technical support. However, SCADA-based water treatment plants perform poorly where replacement parts are not easily obtained and are commonly abandoned in developing countries when critical components malfunction. Simplified chemical dosing systems underpinned by sophisticated designs have been created to promote sustainable operation and are presented in this paper.

2.2.1 *Design Constraints for Sustainability:*

The AguaClara Program at Cornell University has developed a set of design guidelines for the creation of sustainable water treatment technologies. These guidelines embody lessons learned from years of experience inventing new technologies and taking them to full scale implementation through the program's collaboration with Agua Para el Pueblo in Honduras. The AguaClara drinking water treatment plants represent a new paradigm with a focus on the interaction between the plant operator and the technology. The design guidelines used by the AguaClara program that directly influenced the creation of the chemical dose controller and flow measurement systems described here are as follow:

To be operator-friendly, economical, and resilient, municipal scale water treatment plant designs must...

- be optimized for low cost and high performance.

- be easy to construct using low-precision construction techniques.

- minimize use of moving parts.

- operate without electricity.

- be observable (no sealed reactors) so that the plant operator can receive appropriate feedback for performance of every step of the treatment process.

4

- operate without requiring numerical calculations.

- use chemical dosages that can be set directly by the operator.

- be maintainable by one person.

A common method of chemical dosing employed in developing countries is the drip feed system consisting of a chemical stock tank with a small orifice through which the chemical exits (WHO, 2008). These systems are unable to maintain a constant chemical feed rate since the chemical flow rate decreases as the liquid level in the chemical stock tank drops. A floating bowl chlorinator is an example of a dosing system that addresses this problem and maintains a constant flow rate by maintaining a constant driving head even as the liquid level varies (Brikke and Bredero, 2003). However, this system and other stand alone chemical flow controllers regulates the chemical flow rate rather than the chemical dose. Chemical flow controllers require the operator to adjust the chemical flow rate when the plant flow rate is changed and that adjustment is generally by trial and error. Chemical flow controllers represent a level of simplicity that functions reliably but delivers less than what a water treatment plant operator needs.

A different solution to the chemical dosing challenge can be obtained given the goals of maximizing reliability, reducing costs, minimizing the use of components that are not available in the local hardware store, and empowering plant operators to maintain and repair the dosing systems. Reliability can be maximized by reducing the number of components and technology platforms. The number of technology platforms can be substantially reduced by using analog kinematics that connect linearized flow measurement to linearized flow control and completely eliminating the dependence on software, digital electronics, chemical pumps, and electricity. Dose controllers that use a minimum number of components can be described as simplicity on the other side of complexity. This type of dosing system requires sophisticated design methods (complexity), however the resulting device is simple to understand and easy to operate and maintain.

The AguaClara plant dose controller that has been implemented in several water treatment plants by the AguaClara program of Agua Para el Pueblo in Honduras has a minimum number of parts and can be easily repaired if a problem is discovered. The dosing system has two main components: (1) a linear flow orifice meter (LFOM) that creates a linear variation between water height and plant flow and (2) a linear chemical dose controller (LCDC) that provides a chemical flow that is directly proportional to plant flow rate. The design, construction, and testing of these components are described below.
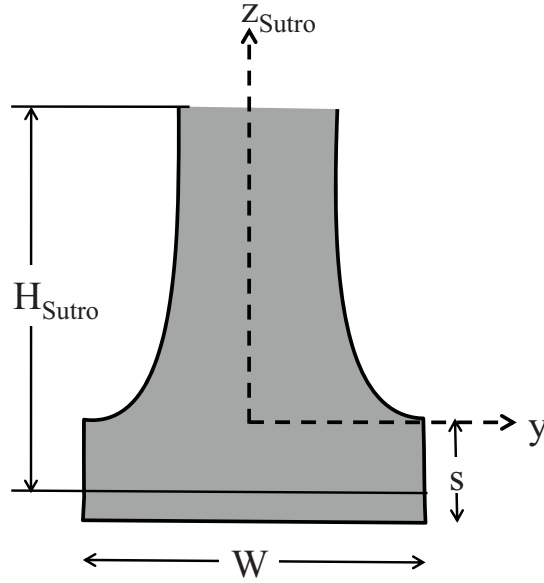
Figure 2.1: Diagram of the Sutro weir

2.3   Theory and Design

2.3.1   Linear Flow Orifice Meter

The Sutro Weir developed by Victor Sutro in 1915 mimics a Stout weir and creates a linear relationship between height of water and flow rate. A Stout weir is a theoretical flow control device in which weir width is proportional to $1/\sqrt{water\ height}$. It is not physically possible to fabricate such a device because the base would be infinitely wide. The Sutro weir, shown in Figure 2.1 serves as a practical alternative to the Stout weir. The width of the base, W, and upper portion of Sutro weir, y, as a function of height can be calculated by Equations 2.1 and 2.2, respectively.

$$W = \frac{Q_{Max}}{H_{Sutro}^{3/2} C_D \sqrt{3g\Pi_{Sutro}}} \tag{2.1}$$

$$y = \frac{W}{2} \left[1 - \frac{2}{\pi} \arctan\left(\sqrt{\frac{z_{Sutro}}{s}} \right) \right] \tag{2.2}$$

where W is the width of the rectangular base of the weir, Q_{Max} is the maximum flow through the weir, H_{Sutro} is the total height of the weir measured from $s/3$ above the bottom of the rectangular weir, Π_{Sutro} is $\frac{2s}{3H_{Sutro}}$, C_D is a discharge coefficient, g is acceleration due to gravity, z_{Sutro} is the vertical distance from the start of a curved section, and s is the height of the rectangular base

(Thandaveswara, 2012). The theoretical flow through the Sutro weir, Q_{Sutro}, is described by Equation 2.3.

$$Q_{Sutro} = \frac{W}{2}\left(2C_D\sqrt{2gsh}\right)$$

(2.3)

where h is the vertical height of water measured from $s/3$ above the bottom of the rectangular weir. Equation 2.3 is only valid when the height of water is above the rectangular portion ($h \geq 2s/3$).

Accurate fabrication of a Sutro weir is somewhat difficult and the Sutro weir has the unfortunate property that the flow rate does not actually go to zero when $h = 0$ because the rectangular opening extends below the datum used for the linear relationship between flow and height. These two disadvantages were addressed in the linear flow orifice meter (LFOM) described in this paper. The LFOM approximates a Sutro weir using a vertical PVC pipe with a pattern of identically sized holes that create a linear relationship between water height and plant flow. The simple construction of the LFOM eliminates the need for skilled labor and uses readily available materials and tools. The LFOM is typically located in the entrance tank of the water treatment plant where water flows through the orifices created by the holes in the vertical pipe on its way to rapid mix and flocculation. The flow through each individual hole, $Q_{Orifice}$, is described by the vertical orifice equation (Equation 2.4). With correct placement of multiple holes, the overall flow can be rendered linear with respect to height of water in the tank, justifying the designation as a Linear Flow Orifice Meter (LFOM).

$$Q_{Orifice} = \Pi_{vc}\sqrt{2g}\int_{0}^{min(D_{Orifice},h)} D_{Orifice}sin\left[acos\left(\frac{2z}{D_{Orifice}}\right)\right]\sqrt{h-z}dz$$

(2.4)

where Π_{vc} is the cross-sectional area of the constricted flow divided by the area of the orifice caused by the vena contracta for the orifice ($\Pi_{vc} = 0.62$ for all cases), $D_{Orifice}$ is the diameter of the orifice, z is integrated from 0 to the minimum of the orifice diameter and height of water ($min(D_{Orifice}, h)$), and h is the height of water above the bottom of the orifice (Franz and Melching, 1997).

There are many potential approaches to the design of an orifice based linear flow meter. The design presented here uses a vertical PVC pipe of appropriate diameter (based on plant flow as described below), a single standard sized drill bit, a minimum number of holes, and a target water level change that is appropriate to drive the dose controller. The algorithm that creates the LFOM hole pattern compensates for the fact that the orifices are all the same size and that there must be an integer number of rows of orifices and an integer number of orifices in each row. The algorithm steps are as follow:

1. calculate the minimum diameter of the vertical pipe required to maintain supercritical flow at the bottom of the LFOM.

7

2. calculate the row spacing to allow use of a large orifice size to minimize the number of holes drilled.

3. calculate the orifice size constrained to be a standard drill bit size, smaller than the row spacing.

4. calculate the number of orifices in each row starting at the bottom row.

The LFOM pipe must be large enough in diameter to ensure that the pressure inside the LFOM at the bottom row of orifices is atmospheric and that the flow inside the LFOM is supercritical. Supercritical flow in the LFOM ensures that it is unaffected by changes in downstream water levels. Each orifice jet accelerates downward due to gravity and the jets collide and exchange momentum. The very bottom of the LFOM has the highest flow rate inside the pipe and this flow velocity must be high enough so that the LFOM pipe is not completely full of water. The average vertical velocity of water at the very bottom inside the LFOM can be obtained by applying free fall acceleration to each orifice jet and then applying conservation of momentum in the vertical direction to obtain the average vertical velocity. This analysis can be simplified substantially by using the Stout weir equation to approximate the vertical velocity of the free falling water at the bottom of the LFOM weir (Equation 2.5). The velocity of water exiting the Stout weir as a function of height when the weir is fully submerged, $h = H_{Stout}$, is:

$$V_{Stout} = \sqrt{2g\left(H_{Stout} - z\right)} \qquad (2.5)$$

The Stout weir equation for the width of the weir as a function of height, z, is:

$$W_{Stout} = \frac{2Q}{H_{Stout}\Pi_{vc}\pi\sqrt{2gz}} \qquad (2.6)$$

where Q is the flow through the Stout weir when the constant water depth is H_{Stout} and Π_{vc} is the vena contracta coefficient, 0.62.

The average velocity of the falling water at the bottom of the Stout weir, $V_{Stout_{z=0}}$, can be obtained by integrating over the depth of the weir to obtain the total momentum in the vertical direction of the falling water when it arrives at the bottom of weir. The average velocity at the bottom of the weir is then obtained by dividing the total momentum by the total mass flux. The water enters the Stout weir with no vertical velocity. The vertical velocity obtained by the time it reaches the bottom of the weir is given by $\sqrt{2gz}$.

$$V_{Stout_{z=0}} = \frac{\int_0^{H_{Stout}} \rho_{Water} V_{Stout} W_{Stout} \Pi_{vc} \sqrt{2gz}\, dz}{\rho_{Water} Q} \qquad (2.7)$$

where ρ_{Water} is the density of water. Substituting equations 2.6 and 2.5 into Equation 2.7 and simplifying gives:

$$V_{Stout_{z=0}} = \frac{4\sqrt{2gH_{Stout}}}{3\pi} \qquad (2.8)$$

Although the total effective width vs height for an LFOM is slightly different than for the Stout weir, Equation 2.8 can be used to estimate the vertical velocity of water at the bottom of the LFOM. For an LFOM with $H_{LFOM} = 20\,cm$, $V_{Stout_{z=0}} = 0.841\,m/s$. A wide range of plant flow rates can be accommodated by a maximum height of $20\,cm$ through the LFOM. The cross-sectional area and diameter of the pipe, can then be found by Equations 2.9 and 2.10 respectively.

$$A_{LFOM} = \Pi_{Safety}\frac{Q}{V_{Stout_{z=0}}} \tag{2.9}$$

$$D_{LFOM} = 2\sqrt{\frac{A_{LFOM}}{\pi}} \tag{2.10}$$

where Π_{Safety} is a safety factor (1.5 used here) that ensures that the velocity at the bottom of the LFOM pipe is more than adequate to ensure that the pipe is not full of water and thus the pressure inside the LFOM is atmospheric. In the design algorithm, the LFOM pipe inner diameter is rounded up to the nearest available pipe size.

Before the surface area of the LFOM can be distributed as a series of orifices, the vertical center-to-center spacing of the rows of orifices, B_{Row} must be found. The design calculation is initialized with two orifices in the top row of orifices (Equation 2.12); however, this number may subsequently be changed as the algorithm progresses. The width of the top of the Stout weir, $W_{Stout_{z=H_{LFOM}}}$, is used to approximate the average width of the weir corresponding to the top row of orifices in the LFOM.

$$B_{RowMax}W_{Stout_{z=H_{LFOM}}} = 2\frac{\pi D_{Orifice}^2}{4} \tag{2.11}$$

orifice diameter, $D_{Orifice}$, is assumed to equal to the maximum row height allowing Equation 2.11 to be solved for the maximum row height.

$$B_{RowMax} = \frac{2}{\pi}W_{Stout_{z=H_{LFOM}}} \tag{2.12}$$

The number of rows of orifices, N_{Rows}, is obtained by dividing the user specified maximum height of the LFOM, H_{LFOM}, by B_{RowMax} and rounding up to the nearest integer with the additional constraint that the total number of rows be between 4 and 10. Linearity between water height and flow is poor when the water level is in the first row of orifices and Equation 2.4 applies. AguaClara water treatment plants use a minimum of 4 rows to provide a linear response down to 25% of the maximum flow rate. Accuracy increases with the addition of more rows and is quite high with 10 rows. There is no advantage to having more than 10 rows as more rows require drilling more holes but does not greatly improve accuracy.

The next design step is to calculate the orifice diameter. The top row of orifices will contain at least one hole. Thus, the orifice area, $A_{TopOrifice}$, in the

top row must be equal to or less than the theoretical stout weir area corresponding to the top row (Equation 2.13). An estimate of the area of the top row of orifices is obtained by integrating Equation 2.6.

$$\frac{\pi}{4} D^2_{OrificeMax} = A_{TopOrifice} = \int\limits_{H_{LFOM}-B_{Row}}^{H_{LFOM}} \frac{2Q}{H_{LFOM}\Pi_{vc}\pi\sqrt{2gz}} dz \quad (2.13)$$

where $D_{OrificeMax}$ is the maximum orifice diameter, Q is the maximum plant rate, g is acceleration due to gravity, and z is the LFOM height over which the equation is integrated.

The diameter of the orifices, $D_{Orifice}$, is constrained to be less than $D_{OrificeMax}$, and also less than B_{Row} and rounded down to the nearest available drill bit size. All orifices in the LFOM design will have this diameter to simplify fabrication. The maximum number of orifices that will physically fit along the circumference of the LFOM pipe, $N_{MaxOrificeperRow}$, is another constraint (Equation 2.14) that is important for high flow rates. The minimum spacing between orifices needed to maintain the structural integrity of the pipe, $S_{MinSpacing}$, is $5\,mm$.

$$N_{MaxOrificeperRow} = \frac{\pi D_{LFOM}}{D_{Orifice} + S_{MinSpacing}} \quad (2.14)$$

If the number of orifices required in the bottom row exceeds the maximum number of orifices that fit in the circumference of the pipe then the design must be modified by either increasing the height of the LFOM or by further increasing the diameter of the pipe.

The final step in designing the LFOM is to calculate the number of orifices in each row. Because the flow rate through the LFOM is linearly proportional to the height of water in the entrance tank, the expected flow rate through the LFOM, $Q_{Nsubmerged}$, when $N_{Submerged}$ rows of orifices are submerged is equal to Equation 2.15.

$$Q_{Nsubmerged} = Q\frac{B_{Row}N_{Submerged}}{H_{LFOM}} \quad (2.15)$$

With an orifice diameter and an expected flow rate per row, the number of orifices per row, $N_{Orifices}$, can be calculated for each row using Equation 2.16 starting at the bottom and incrementing $N_{Submerged}$. The vertical orifice equation (Equation 2.4) is used to find the flow through a single orifice, $Q_{Orifice}$. As the number of orifices in each row is calculated, the flow provided by the lower rows, $Q_{N-1submerged}$, is subtracted from the total expected flow, $Q_{Nsubmerged}$, based on their depth of submergence to obtain flow required through the row of orifices being calculated. The required flow through the row being calculated is divided by the flow per orifice, $Q_{Orifice}$ from (Equation 2.4), and the result is rounded to the nearest integer to obtain the number of orifices required. Once the LFOM pattern of orifices is drilled, the flow rate that corresponds to the

Table 2.1: Summary of Design Specifications for a Linear Flow Orifice Meter (LFOM)

Input	Value		Output	Value
Q_{Plant}	$10\,L/s$		B_{Row}	$2\,cm$
$Drill\,Bits$	$US\,Standard$		D_{LFOM}	$15.2\,cm\ (6\,in)$
H_{LFOM}	$20\,cm$		$D_{Orifice}$	$1.9\,cm\ (0.75\,in)$
$S_{MinSpacing}$	$5\,mm$		$Error_{Max}$	0.34%

water height at each row of the LFOM pattern can be written on the LFOM pipe itself, allowing the operator to read the flow rate directly, avoiding the need for mathematical calculations.

$$N_{Orifices} = \frac{Q_{Nsubmerged} - Q_{N-1submerged}}{Q_{Orifice}} \qquad (2.16)$$

Table 2.1 provides an example of the input and output design parameters for an LFOM for a plant with a maximum design flow of $10\,L/s$. Figure 2.2 shows equivalent designs for the Sutro weir and LFOM with their respective flow profiles. Flow through the LFOM as a function of depth remains linear when orifices are partially full. Custom designs for LFOMs may be obtained at no charge from the AguaClara Design Tool *(aguaclara.cornell.edu/design)*.

2.3.2 Linear Chemical Dose Controller

With the linear relationship between height of water in the entrance tank and plant flow rate provided by the LFOM, the linear chemical dose controller (LCDC) utilizes a float in the entrance tank and a lever to connect the chemical flow rate to plant flow rate. When the plant flow rate increases, the water level in the entrance tank rises proportionally, and the float and lever arm rise as illustrated in Figure 2.3. A stock tank provides a reservoir of the chemical solution (coagulant or disinfectant) and is connected to a constant head tank. The constant head tank is regulated by a float valve which keeps the chemical depth constant. A small diameter tube, referred to here as the dosing tube, leads from the stock tank to a connector tube and then to a vertical drop tube that delivers the chemical to the chemical injection point. The chemical flow rate is controlled by the length of the dosing tube and the elevation head driving the flow - the vertical distance between the chemical surface in the constant head tank and the outlet of the connector tube where it reaches the vertical drop tube. The vertical drop tube is connected to the lever arm via a slider. The plant operator sets the slider at the desired coagulant dose based upon characteristics of the influent water. A locking mechanism holds the slider in place on the lever arm. The float attached to the lever arm changes elevation in response to plant flow rate changes, thus changing the elevation of the dosing tube outlet, and maintaining a constant chemical dose. The LCDC is a semi-automated dosing system that allows the plant operator to set and maintain a
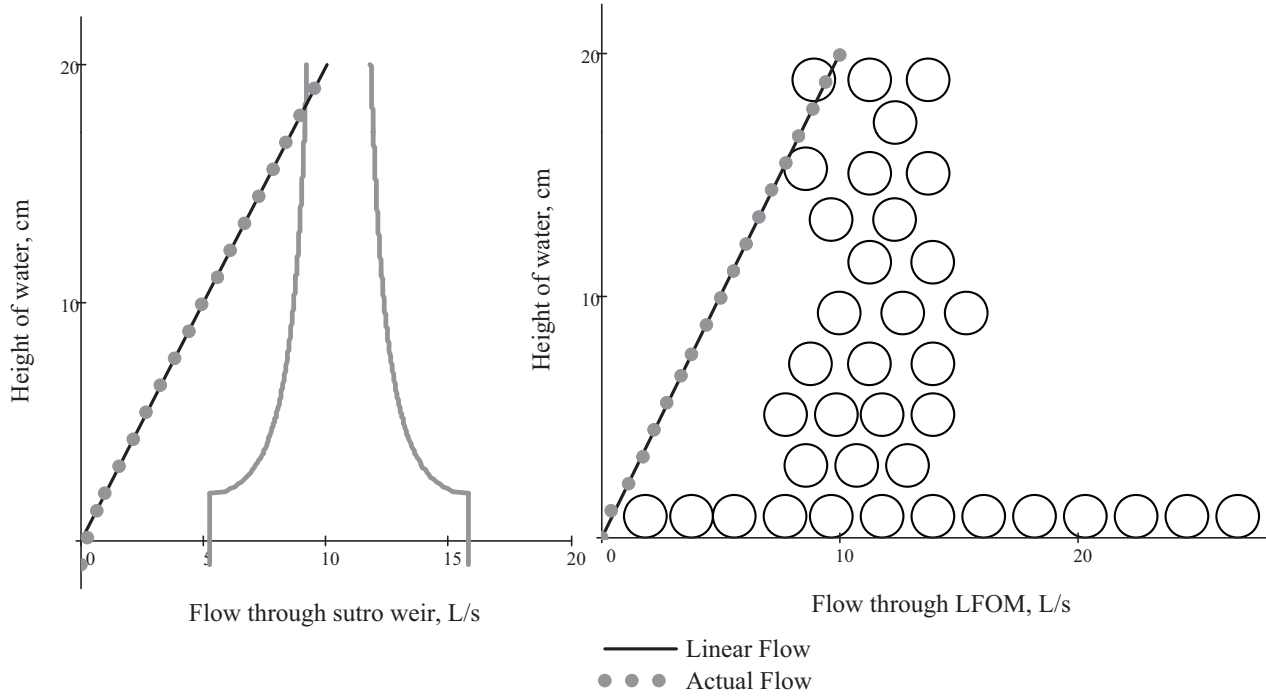
Figure 2.2: Performance of a) a Sutro weir and b) a LFOM designed to provide a $10\,L/s$ flow over a vertical distance of $20\,cm$. Both images are scaled, with the x-axes representing both $0-20\,L/s$ and $0-20\,cm$. The Sutro weir equation is only valid when the height of water is above the rectangular portion. Therefore, the equation for flow over a rectangular weir, $Q_{Rect} = \frac{2}{3}WC_D\sqrt{2g}\,(H_d + s/3)^{2/3}$, was used to calculate the flow for the Sutro weir when the height of water is less than s. The base of the Sutro weir, W, is $9.76\,cm$, the height of the rectangular portion, s, is $4\,cm$. The orifices in the LFOM are $1.905\,cm$ $(3/4\,in.)$ in diameter and the row height, B_{Row}, is $2\,cm$.

chemical dose over time-varying plant flow rates in a visually-accessible system. Dosing changes are made without requiring calculations.

The LCDC uses major head loss in the dosing tube to regulate chemical flow. The linear relationship between major head loss and the chemical flow rate is given by the Hagen-Poiseuille equation (Equation 2.17).

$$Q_C = \frac{h_f g \pi D_{Tube}^4}{128 \nu L_{Tube}} \tag{2.17}$$

where Q_C is the chemical flow rate, h_f is the major head loss, D_{Tube} is the inner diameter of the dosing tube, ν is the kinematic viscosity of the chemical solution, g is the acceleration due to gravity, and L_{Tube} is the length of the small diameter dosing tube. The Hagen-Poiseuille equation assumes that the chemical flow is laminar, viscous and incompressible. The equation also assumes that the flow passes through a straight tube with a constant circular cross-section that is significantly longer than its diameter. Laminar flow in the dosing tube is indicated by a Reynolds number, Re, less than 2100 (discussed below). The assumption that major head loss regulates flow requires that minor losses be minimized. Experiments related to minimization of minor losses are discussed below.

A number of constraints are applied to the design of the LCDC to ensure that the simplest functional solution is chosen. The design algorithm calculates several key parameters for all available dosing tube diameters and chooses the design with the minimum number of tubes and maximum allowable tube length. The algorithm steps are as follows:

1. calculate the maximum flow rate through each available dosing tube diameter that keeps error due to minor losses below 10%.

2. calculate the total chemical flow rate that would be required by the treatment system for the maximum chemical dose and the maximum allowable stock concentration.

3. calculate the number of dosing tubes required if the tubes flow at maximum capacity.

4. calculate the length of dosing tube(s) that correspond to each available tube diameter.

5. select the longest dosing tube that is shorter than the maximum tube length allowable based on geometric constraints.

6. select the dosing tube diameter, flow rate, and stock concentration corresponding to the selected tube length.

For the majority of inputs, limiting the effect of minor losses dictates the design. This constraint is addressed by solving a system of equations where L_{Tube} and the maximum chemical flow rate, $Q_{MaxError}$, are both unknown. Rearranging

13

a)
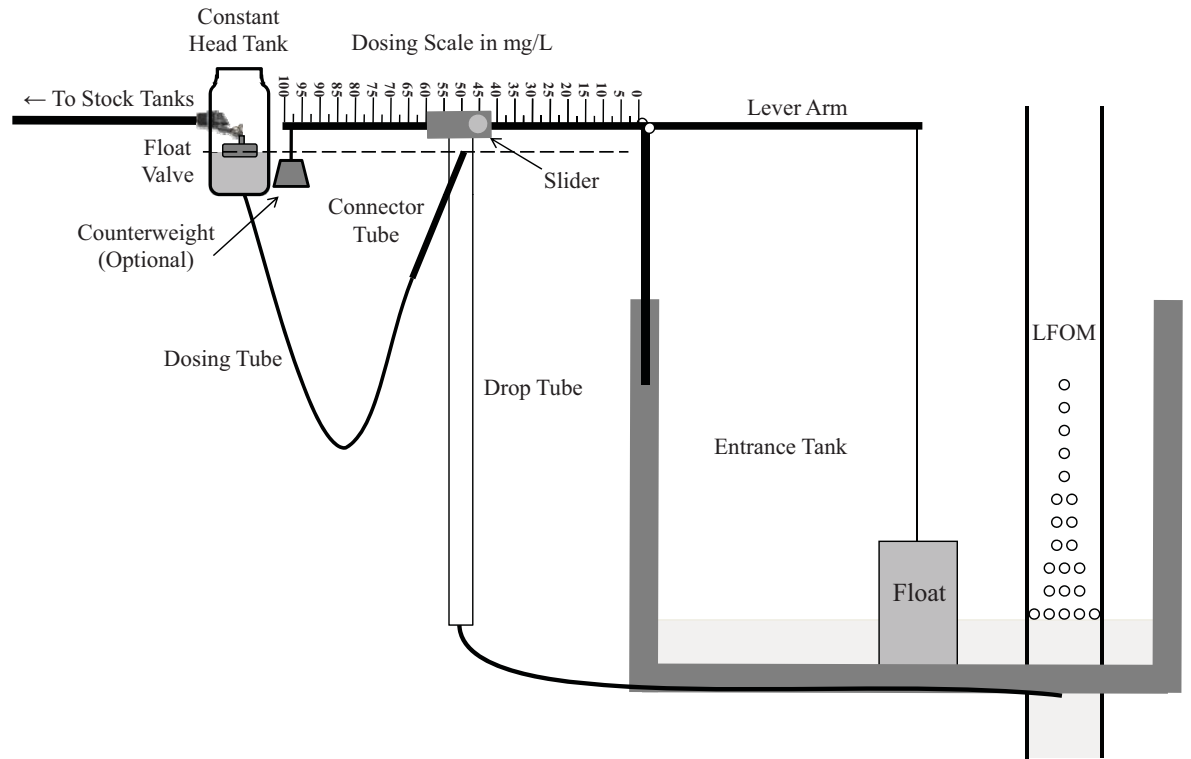
b)
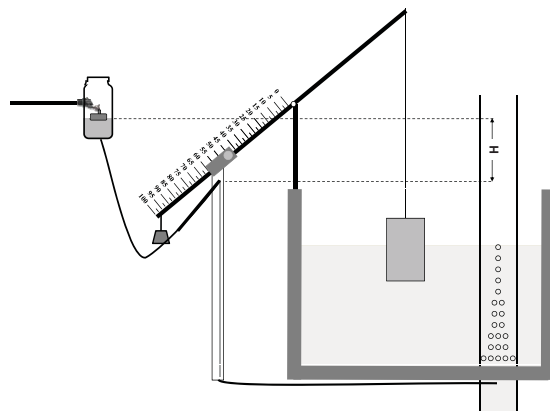
c)
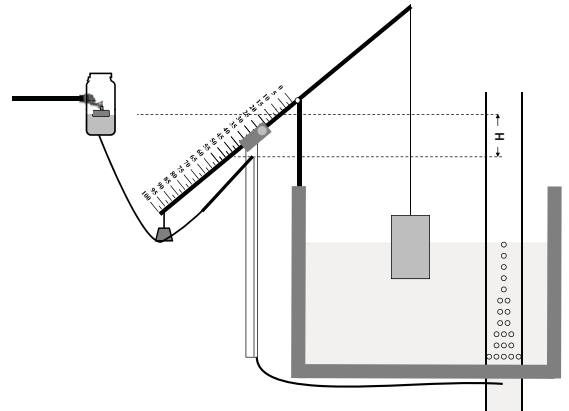
Figure 2.3: Linear chemical dose controller schematic under conditions of: a) no flow, b) maximum flow, and c) maximum flow with a lower chemical dose.

equation 2.17 gives the mechanical energy loss due to shear on the tube wall or major head loss:

$$h_f = \frac{128\nu L_{Tube} Q_C}{g\pi D_{Tube}^4} \tag{2.18}$$

where h_f is the major head loss, which is the lost mechanical energy expressed as a change in elevation. Minor head loss is the mechanical energy loss to deceleration of the fluid caused by changes in the flow geometry and can be calculated by Equation 2.19.

$$h_e = \frac{8Q_C^2}{g\pi^2 D_{Tube}^4} \sum K \tag{2.19}$$

where $\sum K$ is the sum of the minor loss coefficients, all of which use the average velocity in the tube as their reference velocity. The total head loss, h_L, is the sum of the major and minor losses.

$$h_L = h_f + h_e \tag{2.20}$$

The maximum departure from the idealized linear relationship between flow and head loss is equal to the minor loss contribution normalized by the total head loss (Equation 2.21).

$$\Pi_{LinearError} = \frac{h_e}{h_L} \tag{2.21}$$

The maximum flow for a dosing tube will produce an error of $\Pi_{LinearError}$, which is limited to 10% in the design algorithm. This maximum allowable flow rate, $Q_{MaxError}$, based on allowable error can be obtained by substituting Equation 2.19 into Equation 2.21 and solving for Q_C

$$Q_{MaxError} = \frac{\pi}{4} D_{Tube}^2 \sqrt{\frac{2gh_L \Pi_{LinearError}}{\sum K}} \tag{2.22}$$

There is a maximum flow rate for each chemical dosing tube diameter. The array of tube diameters is determined by the available tubes and barbed fittings on the market.

The flow through the dosing tube must be laminar and this sets an upper bound on the tubing diameter that can be used. Equation 2.22 can be solved for the maximum average velocity by dividing by the cross sectional area of the tube.

$$V_{MaxError} = \sqrt{\frac{2gh_L \Pi_{LinearError}}{\sum K}} \tag{2.23}$$

The laminar flow constraint is met when the Reynolds number, Re, is less than the value representing the transition to turbulence, $Re_{Transition} = 2100$,

and prevents the use of large diameter tubes that would also correspond to very long dosing tubes.

$$Re = \frac{V D_{Tube}}{\nu} \tag{2.24}$$

The maximum tubing diameter, $D_{TubeMax}$ than can be used at the maximum flow rate and still maintain laminar flow is obtained by substituting Equation 2.23 into Equation 2.24 and solving for the tubing diameter.

$$D_{TubeMax} = \nu Re_{Transition} \sqrt{\frac{\sum K}{2 g h_L \Pi_{LinearError}}} \tag{2.25}$$

The minimum chemical flow rate required by a water treatment plant, Q_{Min}, given the maximum allowable stock concentration, $C_{StockMax}$, is

$$Q_{Min} = \frac{Q_{Plant} C_{DoseMax}}{C_{StockMax}} \tag{2.26}$$

where $C_{DoseMax}$ is the maximum required dose in the plant and $C_{StockMax}$ is the maximum allowable stock concentration. The number of tubes required to deliver that flow rate, N_{Tube}, for each available tube diameter is calculated and rounded up to the nearest integer.

$$N_{Tube} = \frac{Q_{Min}}{Q_{MaxError}} \tag{2.27}$$

Because the design uses a discrete number of tubes and discrete tube diameters, the actual maximum flow through all tubes, Q_C is calculated for each available tube diameter (Equation 2.28).

$$Q_C = Q_{MaxError} N_{Tube} \tag{2.28}$$

This algorithm maximizes the flow through each dosing tube to reduce the required length of the dosing tubes. If lower flow rates were used, the tubing would need to be made longer to achieve the target head loss. The concentration of the chemical stock, C_{Stock}, is calculated for each available tube diameter because of its effect on the chemical viscosity, ν (Equation 2.29). Variation of coagulant viscosity with concentration was experimentally determined and is discussed below.

$$C_{Stock} = \frac{Q_{Plant} C_{DoseMax}}{Q_C} \tag{2.29}$$

The tube lengths that correspond to the available tube diameters are based on the relationship between the maximum error and major and total losses by combining Equations 2.18, 2.19, 2.20, 2.21, and 2.22 and solving for the tube length.

$$L_{Tube} = (1 - \Pi_{LinearError}) \frac{D_{Tube}^2}{64 \nu} \sqrt{\frac{2 g h_L \sum K}{\Pi_{LinearError}}} \tag{2.30}$$

Table 2.2: Summary of Design Specifications for a Linear Chemical Dose Controller (LCDC)

Input	Value
Q_{Plant}	$10\,L/s$
$Tube\,Diameters$	$US\,Standard$
h_L	$20\,cm$
$\sum K$	4
$\Pi_{LinearError}$	0.1
$C_{StockMax}$	$400\,g/L$
$C_{DoseMax}$	$60\,mg/L$
$L_{TubeMax}$	$2\,m$

Output	Value
D_{Tube}	$3.175\,mm\ (1/8\,in)$
L_{Tube}	$1.03\,m$
N_{Tube}	1
Q_C	$2.3\,mL/s$
C_{Stock}	$260\,g/L\,PACl$

The length of the tube increases with the square of the tubing diameter. This creates a practical upper limit on the tubing diameter that can be used while maintaining a length of tubing that can be accommodated easily in the water treatment plant. The optimal design is chosen by selecting the tube diameter, stock concentration, and chemical flow rate that correspond to the longest tube that does not exceed the maximum length specified by the user.

The parameters noted above are summarized in Table 2.2 for an example plant with a maximum flow of $10\,L/s$ and are implemented in a design algorithm to select a dosing tube diameter and length, chemical stock tank concentration, and number of dosing tubes. The resulting designs for different plant flow rates are shown in Figure 2.4. Custom designs for chemical dose controllers may be obtained from the AguaClara Design Tool *(aguaclara.cornell.edu/design)*.

2.4 Experimental Methods

2.4.1 Determination of minor head loss coefficient

If the major losses dominate minor losses, the linear relationship between the chemical flow rate and the major head loss described by Equation 2.17 would be maintained. Minor head losses caused by flow expansions and contractions as well as tube curvature are proportional to the square of the chemical flow rate. The magnitudes of the minor head losses were modeled in tandem with experimental analysis to minimize their sources. The total head loss through the system (h_L) is the sum of the major (h_f) and minor (h_e) head losses. Therefore, the total head loss through the system can be represented as:

$$h_L = \frac{128\nu L_{Tube}}{g\pi D_{Tube}^4}Q_C + \frac{8\sum K}{g\pi^2 D_{Tube}^4}Q_C^2 \qquad (2.31)$$

There are two terms in Equation 2.31, one with a linear relationship between head loss and chemical flow rate, the other non-linear. The minor head loss coefficient can only be roughly estimated by summing standard values for each

17
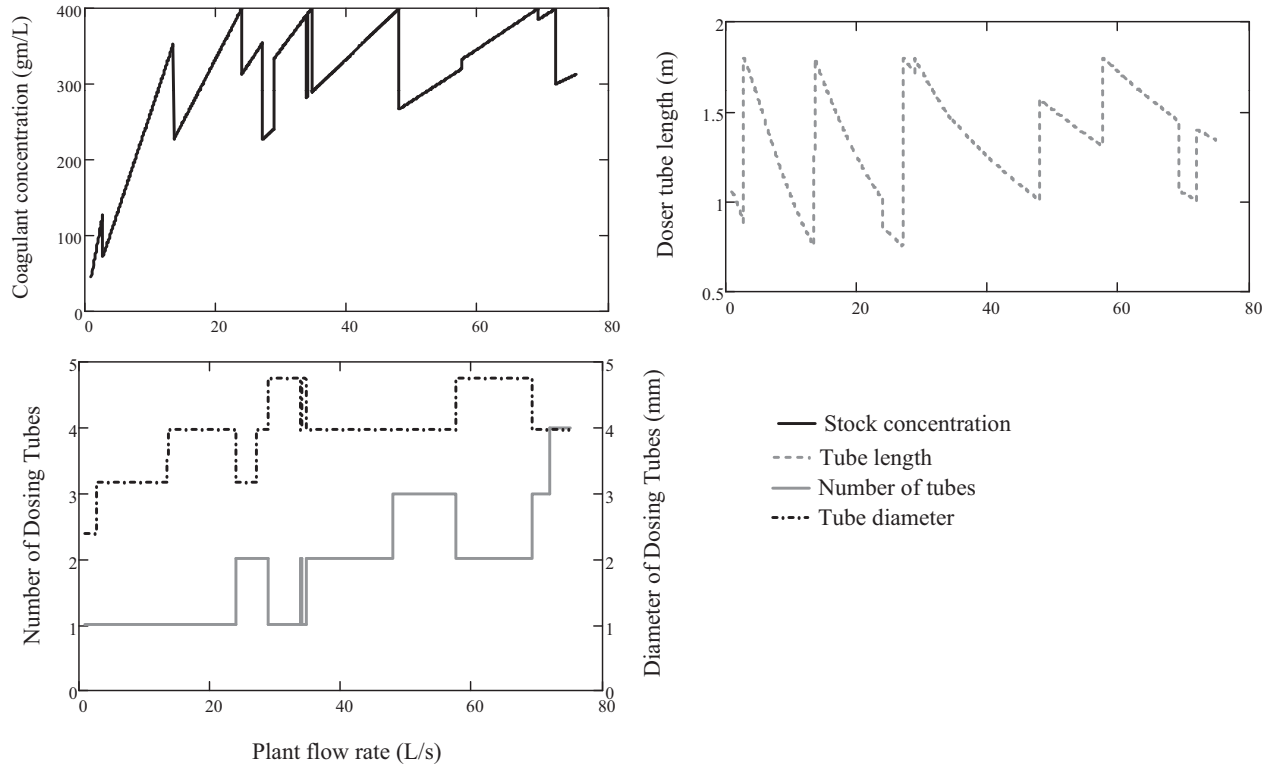
Figure 2.4: LCDC design algorithm results for plant flow rates $1 - 75 \, L/s$. As the flow rate changes, the dominating constraint may change causing the values given by the algorithm to fluctuate. The discontinuities shown are caused by the discrete sizes of tubing and the requirement of an integer number of tubes. For example at approximately $3 \, L/s$ the algorithm changes the specified diameter of the dosing tube from 2.38 mm ($3/32 \, in$) to 3.175 mm ($1/8 \, in$) and the doser tube length and coagulant concentrations must both change to maintain constant dose.

change in flow path, but should be experimentally determined. The minor head loss coefficient for the tested tubing configuration was determined from the array of observed flow rate data and total head loss values using Equation 2.31. Once $\sum K$ is determined for a particular tubing configuration, it can be used to design similar systems for all tube diameters and lengths.

2.4.2 LCDC Prototype Calibration and Testing

LCDC performance tests were conducted in the laboratory using a stationary test stand to simulate changes in plant flow rate. The end of the lever arm that would normally connect to the float was adjusted by inserting a metal pin into holes at specified elevations in the test stand. By setting the driving head directly, deviations from the expected flow rates were attributed to minor losses only. With the slider at the maximum dose, the flow rates through the small diameter dosing tubes and the large diameter connector tubes were measured for tube lengths of $1.32\,m$ to $2.56\,m$ and driving head $0 - 20\,cm$ in $4\,cm$ increments. At each position, three 60 second flow tests were performed and the mean was compared to the expected flow rates. Field tests must ultimately verify that the the maximum desired coagulant flow rate can be achieved.

Calibration of the LCDC system in the field requires adjusting the length of the chain that connects the float to the lever arm to ensure that the lever arm is horizontal at zero plant flow with the slider at maximum chemical dose. Next, with the lever arm still horizontal, the constant head tank must be raised or lowered so that there is no flow through the dosing tube until the lever arm float is raised. The plant flow should then be set to maximum and the chemical flow rate measured. If the flow rate is different than predicted by the algorithm, the length of the dosing tube(s) should be adjusted to achieve less than 5% error at the maximum chemical flow rate (maximum dose and maximum plant flow rate). Guidelines for calibration suggest starting with a dosing tube 10% longer than calculated by the design algorithm and then shortening it in $2\,cm$ increments until a satisfactory agreement wit the maximum flow is obtained.

2.5 Results

2.5.1 Minimizing the Minor Loss Coefficient

Minor losses in the LCDC system cause the flow rate to become increasingly nonlinear with respect to head loss, increasing the errors in dosing. Since minor losses are caused by changes in the flow geometry, several dosing tube configurations were tested to quantify their impact on the sum of the minor loss coefficients (Figure 2.5).

Tube curvature was found to be a significant source of minor losses. Perfectly straight tubing had the lowest $\sum K$ value (2.74). The highest measured loss coefficient (10.36) was observed when the tubing was allowed to drape freely. The optimal tube configuration that allowed the needed flexibility was obtained
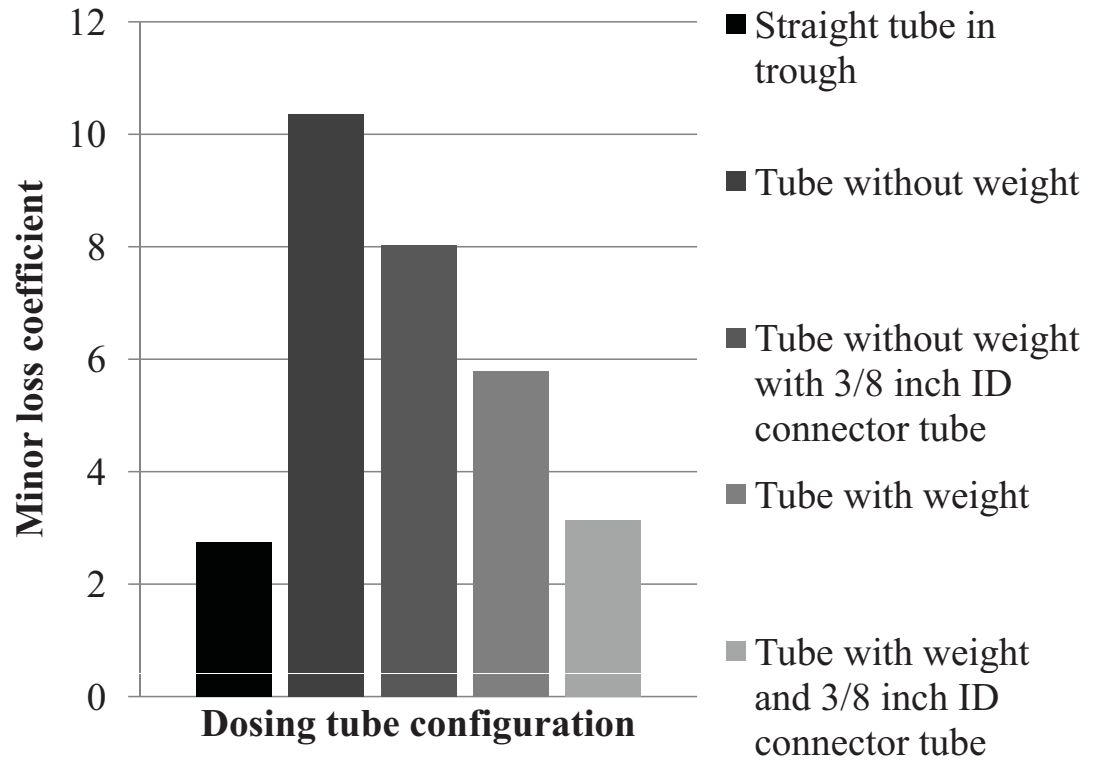
Figure 2.5: Minor loss coefficients for alternative tubing configurations. Values are an average of three trials for a $1.42\,m$ dosing tube over a range of head losses $(0. - 20\,cm)$.

by reducing minor losses associated with curved tubing and connectors. The curved tubing was straightened by attaching a weight to the dosing tube at the low point between the constant head tank and the drop tube, which decreased $\sum K$ to 5.79. The connector losses were also significant and the minor loss coefficient present with straightened tubing was reduced to $\sum K = 3.13$ by providing a $0.952\,cm$ $(3/8\,in)$ connector tube. The connector tube decreases the flow velocity and thus reduces the minor losses in the fittings and at the point where the flexible tube connects to the drop tube. The length of the connector tube can be adjusted without affecting the accuracy of the dosing system.

2.5.2   LCDC Performance Testing

A series of flow tests were carried out for a $1.42\,m$ dosing tube with a weight and a $0.952\,cm$ $(3/8\,in)$ inner diameter connector tube as described previously. The results are displayed in Figure 2.6; also displayed are the flow rates calculated

using the Hagen-Poiseuille equation for major losses (Equation 2.17). By fitting the observed flow rates to the total head loss equation (which includes both major and minor losses) (Equation 2.31) and using a least squares regression, the minor loss coefficient, $\sum K$, was estimated to be 3.13.

2.5.3 Error caused by slider mass

An additional source of error in dose is caused by movement of the slider along the lever arm. Due to the mass of the slider and drop tube on the slider side of the lever arm, there is a variable moment about the pivot point as the slider is moved, which causes a change in the force acting on the float. The change in height of the float when the slider is moved will cause an error in chemical dose. The error resulting from a change in submergence of the float is directly dependent on the total mass of the slider assembly. The vertical displacement of the float, Δh, as a function of float diameter, D_{Float}, is calculated in Equation 2.32.

$$\triangle h = \frac{4M_{Slider}}{\pi D_{Float}^2 \rho_{Water}} \tag{2.32}$$

The lever is leveled at zero plant flow with the slider at maximum chemical dose. Because flow through the dosing tube is linearly proportional to height, the maximum displacement error is $\Delta h / H_{LFOM}$. The maximum allowable error due to changing submergence of the float is given by $\Pi_{FloatError}$, and is set equal to 5% for the calculations presented in this paper. The minimum float diameter that adheres to this constraint, $D_{MinFloat}$, is given by Equation 2.33.

$$D_{MinFloat} = \sqrt{\frac{4M_{Slider}}{\pi \rho_{Water} \cdot \Pi_{FloatError} h_L}} \tag{2.33}$$

With a slider assembly mass, M_{Slider}, of $120\,g$, $D_{MinFloat}$ for the experimental prototype was $12.36\,cm$ ($4.86\,in$); a float diameter of $15\,cm$ ($6\,in$) was used. The prototype has a maximum float displacement of $0.658\,cm$. This error is eliminated by calibration at the maximum chemical dose and then grows to 3.3% for smaller chemical dosages. Moving the slider away from the maximum dose position decreases its moment and decreases the dose which counteracts the increased dose due to minor loss error in the mid dose range. The area of the float at the air-water interface can be increased by using a $20\,cm$ ($8\,in$) diameter float to distribute the volume of displaced water over a larger area, and reduce the maximum displacement error to 1.9%. For plant flow rates large enough to warrant multiple dosing tubes or a larger drop tube, the mass of the slider assembly will increase the dosing error, motivating the switch to a larger float diameter.
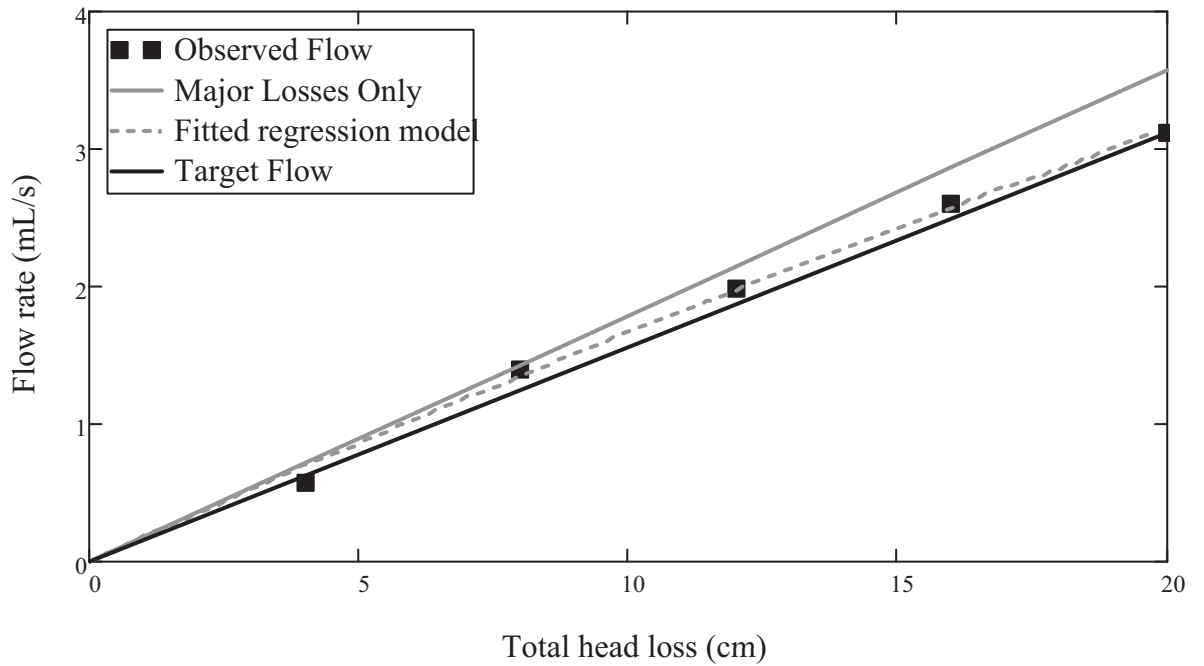
Figure 2.6: Performance test results from a $0.317\,cm$ $(1/8\,in)$ $1.42\,m$ dosing tube with a weight and a $0.952\,cm$ $(3/8\,in)$ connector tube using tap water with $\nu_{Water} = 1\,mm^2/s$. A least-squares regression used the initial observed flow rates to fit a minor loss coefficient, $\sum K$, of 3.13. Field calibration occurs at zero flow and at maximum flow where the deviation from flow expectations based solely on major losses is greatest. Thus, the calibration procedure compensates for minor loses at the maximum flow. Minor losses cause some deviation from the linear relation between the two calibration points but this error is less than 10%.

2.5.4 Coagulant Viscosity

The viscosity of the chemical solution has a considerable impact on the design and performance of the LCDC. Little information is available regarding the viscosity of high concentration coagulant solutions. Therefore, experiments were performed with a Vibro Viscometer to directly measure the kinematic viscosity of alum and PACl solutions with concentrations ranging from $10\,g/L$ to $600\,g/L$ of alum and PACl at $20°C$ (Figure 2.7). To better mimic coagulants used in water treatment practice, industry grade polyaluminum chloride (PACl), (Amuco, Inc.), and technical grade aluminum sulfate, $Al_2\,(SO_4)_3 \cdot 14.3H_2O$, (PTI Process Chemicals) were used as coagulants for all experiments. Each coagulant was diluted with distilled water to make the stock solutions.
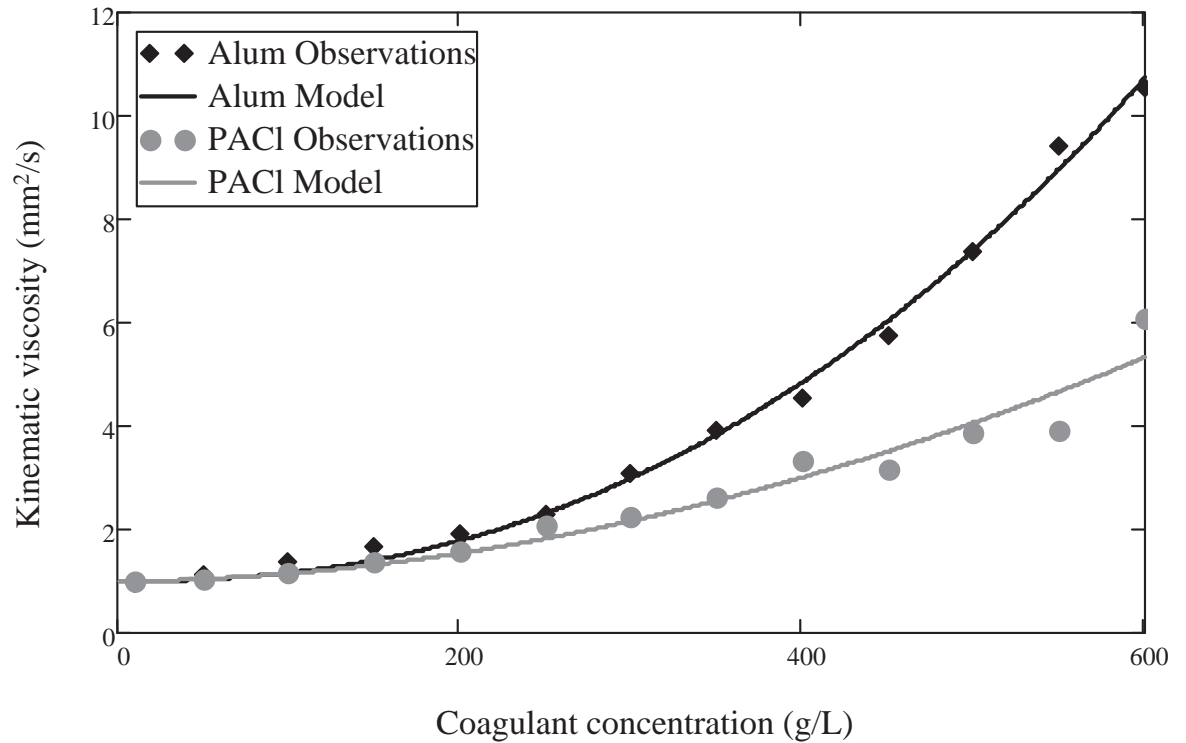
Figure 2.7: Experimentally determined kinematic viscosities of alum and PACl solutions for use as chemical stock concentrations.

Kinematic viscosity must be taken into account when predicting chemical flow rates through the LCDC system. Fits to the experimentally observed relationships were used in the LCDC design algorithms to properly estimate the expected chemical flow through the small diameter dosing tube (Equations 2.34 and 2.35).

$$\nu_{Alum} = \nu_{Water} \left(1 + 4.255 \times 10^{-6} C_{Alum}^{2.289}\right) \qquad (2.34)$$

$$\nu_{PACl} = \nu_{Water} \left(1 + 2.383 \times 10^{-5} C_{PACl}^{1.893}\right) \qquad (2.35)$$

where ν_{Water} is the viscosity of water at $20°C$, $1\,mm^2/s$, C_{Alum} is the alum concentration in g/L alum, and C_{PACl} is the PACl concentration in g/L PACl. The curve fits for Alum and PACl have a sample size, N, of 13 and $R^2_{Alum} = 0.99$ and $R^2_{PACl} = 0.97$. The reader is cautioned that these relationships are for industry and technical grade chemicals, and that other suppliers may provide different compositions. Preliminary tests suggested that viscosity did not vary significantly from ν_{Water} for calcium hypochlorite. Accurate viscosity data is required before designing the LCDC for use with other chemicals.

2.6   Conclusions

The linear chemical dose controller and linear flow orifice meter work in concert to provide a gravity-powered semi-automated chemical dosing system whose function is explained entirely by basic hydraulics, and can be easily fabricated. Through many tests and prototypes, we have converged on a dosing system design that minimizes deviation from the desired linear relationship. Experiments show that use of straight dosing tube segments and connector tube can minimize minor losses. The additional error in dosing created by the variable moment that the slider assembly causes about the pivot point can be minimized by a large diameter float and small mass slider assembly design. Careful component selection and fabrication can ensure that the system will function properly with any chemical solution for a wide range of chemical and plant flow rates (Appendices A and B). The dosing system is versatile, and was designed with the end-user in mind. The design equations have been incorporated into a design algorithm that takes as input the target plant flow rate and outputs all necessary design specifications (available at *aguaclara.cornell.edu/design*). Variation of stock chemical viscosity is considered in the design calculations. The coupled LCDC and LFOM have been tested in six gravity-powered municipal scale drinking water treatment plants designed by the AguaClara Program at Cornell University and built in Honduras. Operator feedback is positive and the systems continue to perform as designed.
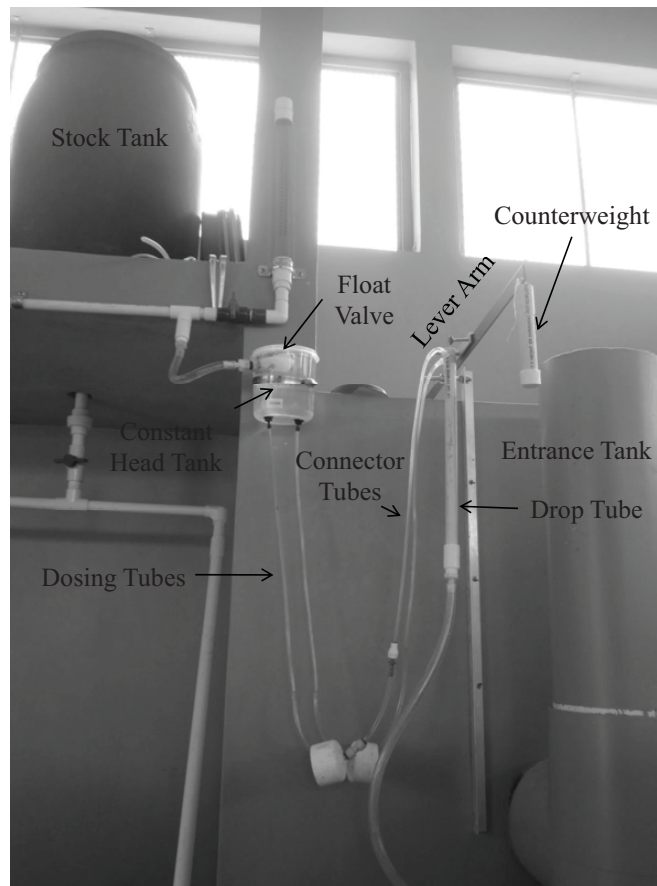
Figure 2.8: LCDC in operation at the Alauca municipal water treatment plant in Alauca, Honduras. Plant flow rate is $12\,L/s$.

2.7 Acknowledgments

2.8 Appendices

2.8.1 Appendix A: Fabrication and Component Selection

In adherence to the sustainable design constraints stated above, the LCDC should, to the extent possible, be made of locally available materials. Therefore, it is important to define the characteristics of each component that are necessary to good performance versus those which are incidental. The system components are designated in Figures 2.3 and 2.8 and their necessary characteristics are as follow:

- The **constant head tank** should have a wide mouth to allow operator access and a diameter that fits the float valve. It should have a cover to prevent debris from entering the chemical solution and one or more small holes in the cover to ensure atmospheric pressure inside. The through-wall bulkhead fittings that connect the dosing tubes to the constant head tank should be barbed and one size larger than dictated by the diameter of the dosing tube to minimize minor losses due to contractions/expansions. A rubber o-ring prevents leaking at the bulkhead connections.

- The **float valve** in the constant head tank (CHT) is the only component that may not be locally sourced in all countries; it is manufactured by Kerick Valves, Inc. and the size used is set by the diameter of the orifice inside the float valve. The orifice diameter needed for the maximum chemical flow rate can be calculated by the orifice equation ($Q = \Pi_{vc}\frac{\pi}{4}D^2\sqrt{2gh}$).

- The **dosing tube** must be kept taut by a weight of approximately $20\,g$ to reduce minor losses due to curvature to maintain straight sections of tubing.

- The dosing tube, attaches to a larger ($0.25 - 0.5\,in$) inner diameter **"connector" tube** with a reducing barbed fitting. Experimental results revealed that attaching the connector tube to the drop tubes rather than attaching the dosing tube directly reduced the minor loss coefficient by 46% (See Figure 2.5). Therefore, the large diameter tube should be used even in plants where additional length is not required. The length of the connector tube is arbitrary and allows the placement of the constant head tank to be more flexible. The connector tube attaches to the drop tube with an NPT-threaded barbed fitting that is also one size larger than the tube diameter.

- The **drop tube** should be transparent to allow the operator to visually confirm chemical flow. The drop tube must be of sufficient length that the bottom of the drop tube is below the lowest water level in the flocculator (zero plant flow). This prevents air from entering the flexible tubing that connects the drop tube to the rapid mix; air in the tubing would create an additional head loss in the flexible tubing which causes intermittent chemical flow to the plant.
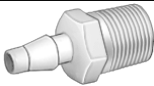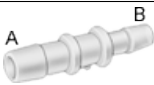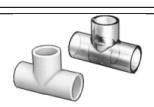
- The **lever arm** should be a three foot long aluminum bar, approximately 2 in wide to provide space for the dosing scale below the slider and to prevent the slider from obscuring reading of the dose. The lever arm should be mounted to the side of the entrance tank at the pivot point.

- The **scale** may be printed on a sticker attached to the lever arm, or stamped directly onto the aluminum lever arm. The scale is to be defined in $\frac{mg}{L}$ of the coagulant or as a percentage of the maximum dose.

- The **slider** should also be aluminum, with one threaded hole for a small screw that acts as a locking mechanism, and another similar screw that holds the drop tube. This connection should be loose, allowing free rotation of the drop tube, which should be vertical at all times. The slider assembly (slider, screws, drop tube, barbed fitting) should be as light as possible because it creates a variable moment about the central pivot that is compensated for by a shift in the height of the float (see *Error caused by mass of the slider* above). To accommodate large flow plants where multiple dosing tubes are needed, a "T"-shaped slider assembly can be used. The "T" is made of the same clear PVC as the drop tubes, and each of the barbed fittings is located along a horizontal bar that adjusts to be level with the ground as the lever arm moves. In the case of multiple tubes, all tubes supply the desired chemical doses simultaneously, allowing the LCDC to dose plants with high flow rates. A counterweight can be used to maintain tension in the chain connecting the float to the lever arm if the variable moment caused by the slider is insufficient (See Figure 2.8).

- The **float** should be as wide and short as possible. The float should not touch the bottom of the entrance tank at zero plant flow and should be water tight. The mass of the float should be high compared to the mass of the slider assembly. The float must have a center of gravity that is below the center of buoyancy to provide stability.
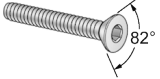
A list of parts used in the LCDC prototype is included in the Supplemental Materials section (Table 2.3).

While chemical compatibility between the aluminum and PVC components and coagulant and chlorine solutions will protect the LCDC from degradation over time, occasional maintenance is required. If calcium hypochlorite is used as a disinfectant, calcium carbonate precipitate forms when the chlorine solution comes in contact with atmospheric carbon dioxide, and the upper, open end of the drop tubes are likely to develop significant calcium carbonate precipitate. Periodically, this will need to be removed or dissolved with vinegar so it does not interfere with the chemical flow.

2.8.2 Appendix B: Components List

Table 2.3: Detailed list of components for the LCDC. This listing is for a LCDC designed for a $10\,L/s$ water treatment plant. Depending on the plant capacity, different quantities or sizes may be required.

Part Name	Picture	Description and Explanation
Barbed Fitting for Constant Head Tank		Durable nylon single-barbed tube fitting through-wall adapter for connecting the dosing tube to the CHT.
Barbed Fittings for Drop Tubes		Allows the chemical/coagulant to enter the drop tube from the $0.952\,cm$ ($3/8\,in$) inner diameter connector tube.
Reducing Barbed Fittings		Reducing barbed fitting that goes from $0.317\,cm$ ($1/8\,in$) inner diameter dosing tube to $0.952\,cm$ ($3/8\,in$) inner diameter connector tube.
PVC Drop Tubes		Clear plastic so that plant operator can observe flow. Should be $1.22\,cm$ ($\frac{1}{2}\,in$) in diameter to keep as lightweight as possible while ensuring free fall of the chemical solution.
PVC Tubes for Counterweight		A short ($5\,cm$) section of PVC pipe can be used as the optional counterweight.
Large Diameter Connector Tubing		Clear plastic tubing with $0.952\,cm$ ($3/8\,in$) inner diameter to be used as a connector to the drop tube.
Small Diameter Dosing Tubing		Attached to the base of the CHT and the connector tube via a reducing barbed fitting. Clear $0.317\,cm$ ($1/8\,in$) inner diameter. Length specified by the algorithm.
PVC Tee		$1.24\,cm$ ($1/2\,in$) PVC tee. Used for a T-shaped slider assembly when the algorithm recommends more than one dosing tube for higher flow systems.
PVC Pipe Cap		Schedule 40 white PVC pipe cap attached to the ends of the "T" and to the bottom of the drop tubes.

Turnbuckle		Connects the float chain to the lever-arm apparatus. Allows for adjustment during calibration.
Constant Head Tank		Translucent plastic jar (2 L), $14.92\,cm$ base diameter, $15.88\,cm$ height with a hole drilled in the bottom center for the through-wall barbed fitting. The cover prevents contamination of the chemical by particles in the air, but does not make the container air-tight. Small drilled holes can be used to allow air flow.
Lever Arm		Aluminum, $0.914\,m$ $(3\,ft)$ in length, $5\,cm$ $(2\,in)$ in width, and $0.635\,cm$ $(1/4\,in)$ in thickness.
Slider		Corrosion resistant aluminum, u-channel, $0.317\,cm$ $(1/8\,in)$ thick, $1.27\,cm$ $(1/2\,in)$ base, $1.905\,cm$ $(3/4\,in)$ legs, $10.16\,cm$ $(2\,in)$ in length. Attached to the top of the lever arm to vary the coagulant dose.
Aluminum shaft collar		$0.952\,cm$ $(3/8\,in)$ bore, $1.905\,cm$ $(3/4\,in)$ outer diameter, $0.952\,cm$ $(3/8\,in)$ width; aluminum shaft collars are secured on either side of each of the lever arms to prevent the lever arms from shifting laterally along the shaft
Hex nut		For use between the drop tube and the slider. Permits the drop tube to swing freely.
Screws		$1.27\,cm$ $(1/2\,in)$ 10-32 screws. One for the slider locking mechanism, one to hang the drop tube
Kerick Float Valve		Attached to the side of the constant head tank, and it keeps the water level constant inside the CHT.
Square head plug		$15.24\,cm$ $(6\,in)$ PVC threaded square head plug for the top of the float. Water tight but removable to allow weight to be added to the float

PVC cap		15.24 cm (6 in) unthreaded PVC cap for the bottom of the float
Threaded adapter		15.24 cm (6 in) threaded adapter to receive the square head plug and convert to unthreaded pipe
PVC pipe		15.24 cm (6 in) pipe is needed to connect the adapter to the PVC cap. Use no more than is necessary for this purpose.

2.9   References

Brikke, F., Bredero, M., 2003. Linking technology choice with operation and maintenance in the context of community water supply and sanitation: A reference document for planners and project staff. Tech. rep., World Health Organization and IRC Water and Sanitation Centre.

Franz, D. D., Melching, C. S., 1997. Full Equations Utilities (FEQUTL) Model for the Approximation of Hydraulic Characteristics of Open Channels and Control Structures During Unsteady Flow. Water Resources Investigations Report 97-4037, U.S. Geological Survey.

Thandaveswara, B. S., 2012. Proportional weirs. Tech. rep., Indian Institute of Technology Madras.

World Health Organization, 2011. Fact sheets on environmental sanitation: fact sheet 2.22- dosing hypochlorite solutions. Tech. rep.

Chapter 3

Method for Quantitative Analysis of Flocculation Performance

3.1 Abstract[1]

The sedimentation rate and the post-sedimentation residual turbidity of flocculated suspensions are properties central to the design and operation of unit processes following flocculation in a water treatment plant. A method for comparing flocculation performance based on these two properties is described. The flocculation residual turbidity analyzer (FReTA) records the turbidity of flocculent suspensions undergoing quiescent settling. The fixed distance across which flocs must travel to clear the measurement volume allows sedimentation velocity distributions of the flocculent suspension to be calculated from the raw turbidity data. By fitting the transformed turbidity data with a modified gamma distribution, the mean and variance of sedimentation velocity can be obtained along with the residual turbidity after a period of settling. This new analysis method can be used to quantitatively compare how differences in flocculator operating conditions affect the sedimentation velocity distribution of flocs as well as the post-sedimentation residual turbidity.

3.2 Introduction

The sedimentation velocity (V_s) of colloidal aggregates (flocs) formed in flocculation with hydrolyzing metal salts and their precipitates is an important parameter to consider in the design and operation of water treatment plants. V_s determines the design of sedimentation clarifiers and plate settlers. The V_s

---

[1]The contents of this chapter are published in the *Water Research*, with co-authors I.C. Tse, M.L. Weber-Shirk and L.W. Lion.

of a floc has been shown to increase with floc size (Tambo and Watanabe, 1979; Adachi and Tanaka, 1997). An ideal flocculator would produce flocs with high V_s and settled water with low residual turbidity after subsequent sedimentation processes. Floc V_s is typically measured in the laboratory using a settling column test (Metcalf and Eddy, 2003). In water treatment plants, coagulant doses are often determined by observing the residual turbidity of jar test samples to identify the dose that produces the most efficient floc sedimentation. Because of floc break-up and the formation of gelatinous precipitates, optical measurement techniques are preferred over particle counters to determine floc size distributions (Ching et al., 1994). Gregory (1985) developed an optical technique based on measurement of turbidity fluctuations in flowing suspensions to monitor floc suspensions, and demonstrated that the ratio of the root mean square of the fluctuating turbidity signal to the mean value is roughly proportional to the size of the aggregates flowing through the detector and to the square root of their concentration.

Two of the most informative parameters for plant designers and operators are floc sedimentation rates and residual turbidity after a period of settling. Thus, an apparatus capable of optically quantifying both V_s and residual turbidity as a method for comparing the performance of different flocculation conditions would be an extremely useful tool for researchers and plant operators alike. The following sections describe an experimental measurement apparatus and process for data analysis that is capable of providing the desired information. An analysis of flocs formed under different conditions is provided as an example application.

3.3   Apparatus

3.3.1   FReTA

The flocculation residual turbidity analyzer (FReTA) is a measurement apparatus designed at Cornell University that measures both the sedimentation velocity and the residual turbidity of the effluent from a flocculator (see Figures 3.1 and 3.3).

FReTA is capable of measuring floc V_s without affecting the structure of flocs that have been formed. FReTA consists of three primary components: an inline turbidimeter, a transparent glass column, and an electrically actuated ball valve. The interaction of these components, as well as the acquisition and the analysis of data were automated using Process Controller software created using LabVIEW by Weber-Shirk (2008). A modified HF Scientific MicroTOL 2 infrared inline nephelometric turbidimeter was used in the apparatus. The plastic housing of the turbidimeter was altered to allow a $2.54\,cm$ (1") outer diameter, $2.06\,cm$ (0.812") inner diameter glass tube to fit vertically through the entire turbidimeter housing and through the measurement area. The glass column provided a quiescent chamber for flocs to settle as turbidity was measured over time. The glass column replaced the factory-standard measurement
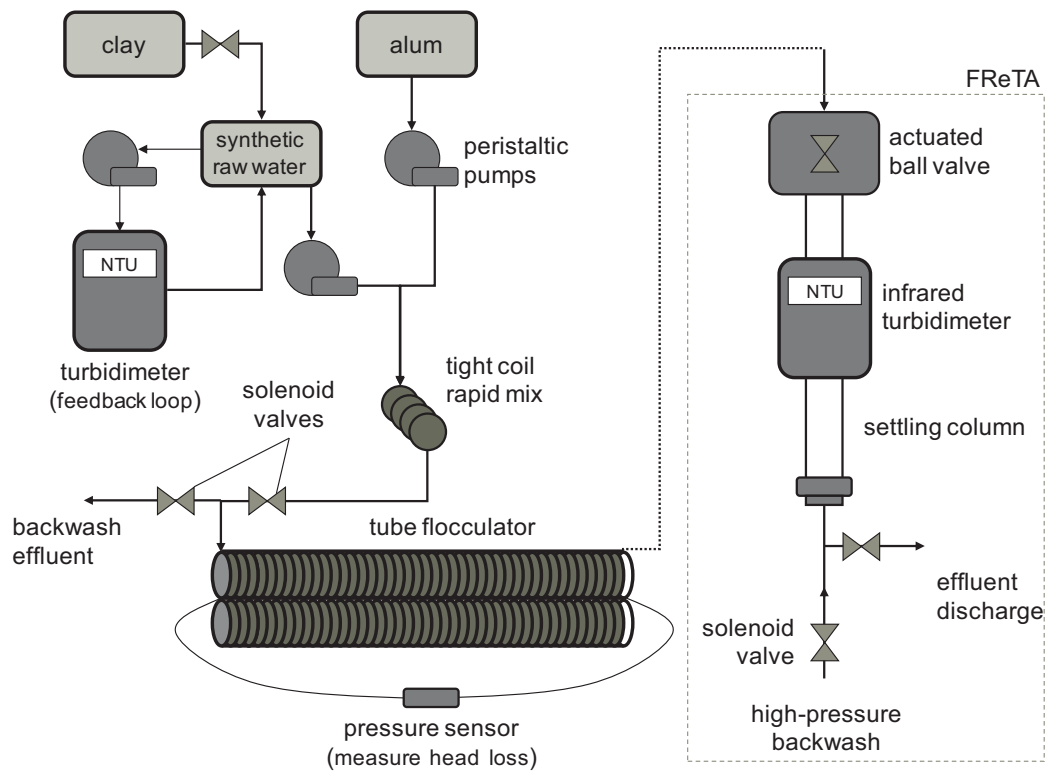
Figure 3.1: Schematic of the complete experimental assembly.

clay

alum

synthetic
raw water

peristaltic
pumps

NTU

turbidimeter
(feedback loop)

solenoid
valves

tight coil
rapid mix

backwash
effluent

tube flocculator

pressure sensor
(measure head loss)

FReTA

actuated
ball valve

NTU

infrared
turbidimeter

settling column

effluent
discharge

solenoid
valve

high-pressure
backwash
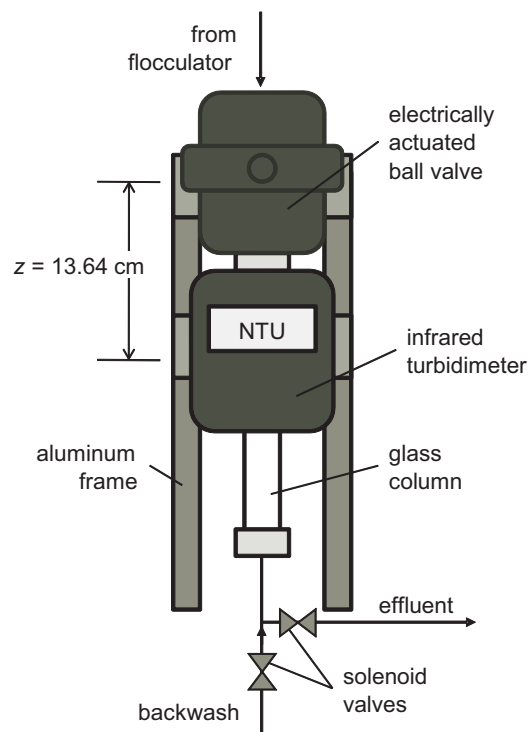
Figure 3.2: FReTA consists of an electrically actuated ball valve at the top and an IR nephelometric turbidimeter fitted with a glass tube and connected by fittings to an effluent line.

cuvette because the standard measurement cuvette had a restrictive inlet that disrupted flocs entering the chamber. A small diameter settling column was used to accommodate the diameter of the turbidimeter sample cell. Calculations using methods described in McNown and Malaika (1950) were performed to ensure that errors produced by wall effects were not significant. Wall effect errors were estimated to be much less than 1% in all cases.

It was important that fluid motion inside the glass column be minimized once measurements had begun. A version of the MicroTOL 2 turbidimeter using a LED infrared light source instead of an incandescent bulb was used to eliminate thermal convection currents that interfered with quiescent settling. The manufacturer-installed heat source and fan used to control condensation in the MicroTOL 2 were also disabled to minimize convection currents.

The HF Scientific MicroTOL 2 turbidimeter was set at its minimum response time of one second, while the data was collected at a rate of 1 Hz. Prior to use, the turbidimeter was carefully calibrated using a HF Scientific, Inc. Primetime Calibration Standards kit, which uses a solution that is more stable and has a longer shelf life than Formazin. According to the manufacturer, the turbidimeter's accuracy for readings below 40 NTU was $\pm 2\%$ of readings or ± 0.02 NTU (whichever is greater) and for readings above 40 NTU, the accuracy was $\pm 5\%$ of readings. The modifications made to the HF Scientific MicroTOL 2 turbidimeter to create FReTA did not affect the accuracy of the instrument. The 95% confidence interval was shown to be within $\pm 2\%$ of the mean reading obtained from bootstrapping a data set containing 1000 turbidity measurements of a stable clay suspension.

An electrically actuated ball valve (Gemini Valve model 630) attached to the top of the glass tube was used to seal the connection between the flocculator and the settling column. It prevented flocs in the flocculator above the valve from entering the settling column once measurements began. The valve defined the top of the settling column. A distance of $13.64\,cm$ separated the bottom of the ball valve and the center of the $5\,mm$ zone illuminated by the LED of the turbidimeter. This distance was used for the calculation of sedimentation velocities as discussed below. An elbow connected the bottom of the glass tube to an effluent discharge line.

The quiescent settling test has been used for decades and the subsequent experimental results accepted for design of sedimentation tanks. The FReTA apparatus simply automates this test and the ensuing data analysis. The settling column and general experimental design has been validated by Adachi and Tanaka (1997), where a square glass settling tube (20 x 20 x 300 mm) was used to observe the settling of flocs through a microscope. The validity of this apparatus was confirmed by observing the sedimentation of standard latex spheres.

A monodisperse suspension of flocs will settle at a single velocity and the time series of measured turbidity would start at some initial value and fall sharply to the residual turbidity of the supernatant as the entire suspension of flocs settled below the turbidity detector. In a sample with heterodisperse floc sizes, the distribution of sizes can be discretized into bins using average V_s. The

time series of turbidity measurements for a heterodisperse sample has a more gradual decrease that asymptotically approaches a final residual supernatant turbidity. Since the maximum distance (z) a floc must settle in order to clear the measurement volume is the distance between the bottom of the ball valve to the measurement volume of the turbidimeter ($13.64\,cm$ in this case), an estimate of the sedimentation velocity of a bin of floc sizes can be made by dividing the distance (z) by the time elapsed since settling began (t).

$$V_s = \frac{z}{t} \tag{3.1}$$

The maximum distance ($13.64\,cm$), duration of the settle state ($30\,minutes$), and turbidimeter response time (one second) dictate that particles with settling velocities greater than $136.4\,\frac{mm}{s}$ or less than $0.076\,\frac{mm}{s}$ will not be detected.

To minimize or eliminate differential settling, the distance between the top of the column to the illuminated zone was minimized to the shortest distance physically permitted by the valve and fittings. In addition, the distance ($13.64\,cm$) used is much less than the 0.5 m interval between sampling ports used in conventional flocculent settling tests and discrete settling is assumed in analysis of data over this distance (Metcalf and Eddy, 2003). Therefore, the assumption of discrete settling in the analysis of FReTA data is consistent with the treatment of data in flocculent settling tests. In this study FReTA was located immediately downstream of the tube flocculator. Thus, the V_s distribution and residual turbidity values obtained by FReTA represent the initial characteristics of the flocculated particles, and do not represent the V_s distribution or residual turbidity that would be obtained deeper in a sedimentation tank after significant particle contact and aggregation through differential sedimentation had occurred. FReTA was positioned immediately after the flocculator to characterize particles exiting this reactor; however, other points in a treatment process stream could also be used for sampling such as different positions within a sedimentation tank or after sedimentation.

3.3.2 Tube Flocculator

The complete experimental assembly consisted of three main parts: a synthetic raw water (SRW) metering system, followed by rapid mix and a tube flocculator (Figure 3.3), and then FReTA. As a mixture of suspended clay and alum flow through the tube flocculator, velocity gradients in the tube cause particles to collide and form flocs.

The tube flocculator consisted of a length of $9.5\,mm$ ($\frac{3}{8}\,in$) inner diameter transparent plastic tubing wrapped in a figure eight shape around two long parallel cylindrical prisms for structural support. A pressure sensor was attached at each end of the tube flocculator to monitor the pressure drop (head loss) across the flocculator. The length of the flocculator could be changed to accommodate different hydraulic residence times (θ). Tube geometry was used for the flocculator because the velocity gradient (G) in laminar tube flow is well defined (Equation 3.2)(Gregory, 1981).

3/8" ID tubing

support cylinders

11 cm

15 cm

influent

effluent

head loss sensor

5 cm OD

rapid mix

synthetic raw water & alum
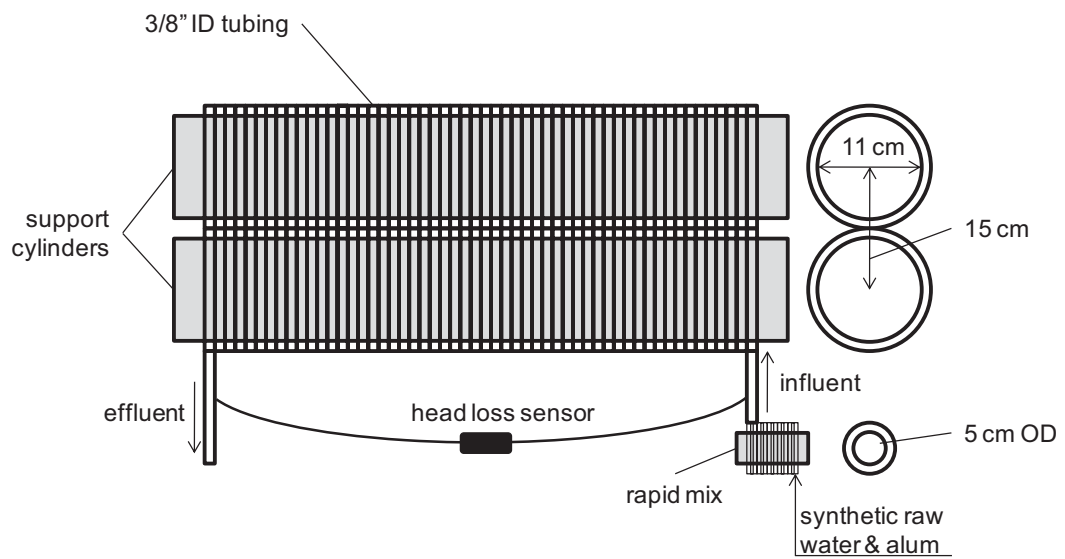
Figure 3.3: Tube flocculator consists of a segment of $\frac{3}{8} \, in$ inner diameter clear plastic tubing wrapped in a figure-8 configuration.

$$G_s = \frac{8Q}{3\pi r^3} \qquad (3.2)$$

where: Q is the volumetric flow rate and r is the inner radius of the tube.

The number of particle collisions per unit time in a laminar flow flocculator is proportional to G and the time available for collision is θ, therefore the product $G\theta$ indicates the degree of flocculation that can be achieved (Cleasby, 1984). Initial calculations showed that the length of tubing needed to achieve adequate flocculation based on the suggested $G\theta$ value of 20,000 necessary for large floc formation (Camp and Stein, 1943) was roughly 28 meters and was too long to maintain as an entirely straight segment, so the tube flocculator was initially arranged into a helical coil. The length of tube flocculator can be increased to two or three times this length, producing $G\theta$ values of 40,000 or 60,000.

The velocity gradient in straight laminar tube flow is axisymmetric about the centerline of the tube and increases linearly from the centerline where the velocity gradient is zero to the maximum value at the wall. While laminar flow can still be achieved in helically coiled tubes, the flow is no longer axisymmetric. The inertia of the fluid in the curved tube causes the highest velocity fluid at the center of the tube to move towards the wall farthest from the axis of curvature (Berger et al., 1983). The resulting flow pattern consists of two rotating cells with the line of symmetry being the radius of curvature of the coil. Because of the parabolic velocity profile found in straight laminar tube flow, both G and θ are functions of radial position, creating a range of $G\theta$ values experienced by particles within the tube. Particles entering a coiled tube flocculator, however, do not maintain a constant radial position in the tube, consequently the distribution of $G\theta$ values experienced by particles is narrower than in a straight tube (Gregory, 1981). It was observed that particles preferentially aggregated inside the two vortical cells throughout the length of the coiled tube flocculator. Furthermore, one of these two cells consistently trapped larger sized flocs over the length of the flocculator than the other cell. Since particles were trapped spinning inside the vortical cells, the helical tube flocculator essentially acted like two separate flocculators. Reconfiguring the helical coils into a figure eight disrupted the two circulating cells and allowed particles to move around in the cross-sectional plane.

While the flow may still be laminar in a curved tube—in that streamlines are continuous and nonintersecting, the velocity gradients are not axisymmetric throughout the cross section and have a non-linear relationship with axial velocity. The axial velocity remains proportional to the flow rate through the tube, but the centrifugal force introduces velocity components perpendicular to the centerline axis. As described below, a correlation factor comparing the friction coefficients of a straight tube (f_s) to that of a curved tube (f_c) (Mishra and Gupta, 1979) was used in the calculation of the average velocity gradient in the curved tube, G. Based on dimensional analysis, the velocity gradient G can be expressed as a function of the average energy dissipation rate (ε) and kinematic viscosity of the fluid (ν):

$$G = \sqrt{\frac{\varepsilon}{\nu}} \qquad (3.3)$$

Using conservation of energy, ε can be expressed as kinetic energy loss over a period of time:

$$\varepsilon = \frac{gh_L}{\theta} \qquad (3.4)$$

where g is gravitational acceleration, h_L is head loss and θ is average hydraulic residence time. The head loss through a straight tube can, in turn, be defined as (Robertson et al., 1998):

$$h_L = f_s \frac{LU^2}{2gd} \qquad (3.5)$$

where L is the length of the flocculator and f_s is the friction factor in a straight tube. For laminar flow, the friction factor $f_s = \frac{64}{Re_d}$, and Re_d is the Reynolds number as defined as:

$$Re_d = \frac{Ud}{\nu} \qquad (3.6)$$

where U is the average axial velocity and d is the tube inner diameter. The formulation for G derived by Gregory (1981) (see Equation 3.2) can also be derived from algebraic rearrangement of Equations 3.3-3.6. A correlation factor (Mishra and Gupta, 1979) can be applied to Equation 3.5 to replace f_s with f_c (Equation 3.7) and correct for the differences in head loss between straight and curved tubes.

$$\frac{f_c}{f_s} = 1 + 0.033log(De)^4 \qquad (3.7)$$

where De is the non-dimensional Dean number and characterizes the effect of curvature on fluid flow:

$$De = \sqrt{\frac{r}{R_c}} Re_d \qquad (3.8)$$

where r is the inner radius of the tube and R_c is the radius of curvature. The average head loss measured as the pressure drop across the tube flocculator was within 2% of the head loss calculated using Equations 3.5 and 3.7 (Figure 3.4).

The figure eight coil configuration used in this research was different from the flow regime modeled by Mishra and Gupta. The fact that our data agrees with their model suggests that the change in direction of the coil had only a small effect on total head loss. The following G value obtained from combining Equations 3.3-3.8 was used to design the experimental runs.

$$G_c = G_s \left(1 + 0.033log(De)^4\right)^{\frac{1}{2}} \qquad (3.9)$$
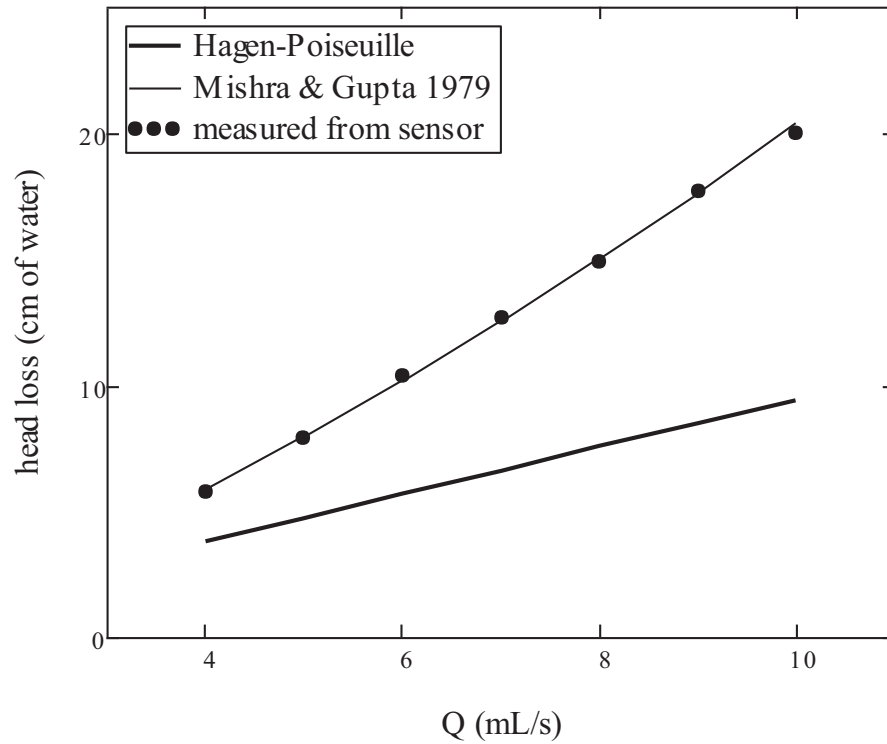
Figure 3.4: Comparing head loss across a $18.64\,m$ tube flocculator measured by a pressure sensor and values computed using the Mishra and Gupta (1979) correlation factor. Hagen-Poiseuille prediction for straight pipe flow is shown for comparison.
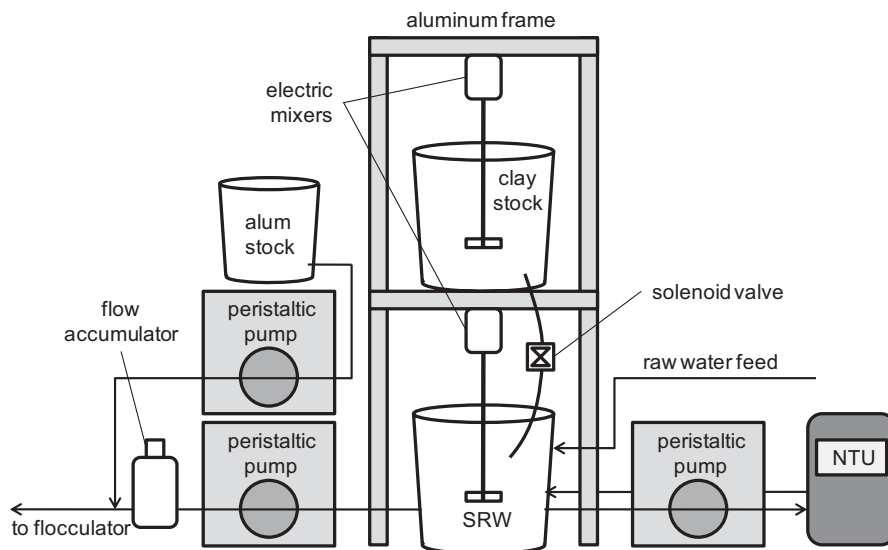
Figure 3.5: Synthetic Raw Water (SRW) and coagulant metering system.

The velocity gradient established in a tube is a function of the fluid flow rate and the cross sectional area of the tube. The cross sectional area of the tube can limit the largest size of flocs the flocculator can produce. The inner diameter of the tube flocculator was $9.5\,mm$ ($\frac{3}{8}\,in$). The expected diameter of the largest flocs was on the order of $1\,mm$, therefore an inner diameter of $9.5\,mm$ was large enough to facilitate the formation of $1\,mm$ flocs. The length of the tube flocculator and flow rate could be varied depending on the goals of a particular experiment. The data given in the paper corresponds to a flow rate of $5\,\frac{mL}{s}$, Reynolds number of 668, and a flocculator length of $56\,m$ (any exceptions are noted).

3.3.3   Raw Water and Coagulant Metering System

The raw water metering system consisted of a concentrated stock suspension of kaolinite clay (R.T. Vanderbilt Co., Inc., Norwalk, CT) mixed with water to produce a feedback-regulated synthetic raw water (SRW) feedstock (see Figure 3.5). The concentrated stock and the SRW feedstock were each stirred by a variable speed mixer to keep the suspensions completely mixed. A Cole Parmer Master-Flex L/S digital controlled peristaltic pump provided a continuous stream of the SRW in a closed loop to a HF Scientific MicroTOL 2 turbidimeter to monitor

its turbidity. If the turbidity reading of the SRW fell below the target turbidity for an experiment, a solenoid pinch valve regulating the flow between the concentrated clay suspension and the feedstock opened to gradually increase the turbidity of the SRW feedstock. A float valve regulated the flow of temperature controlled (25°C) tap water into the SRW tank to maintain a constant water level. Tap water characteristics were approximately: total hardness $\approx 150 \frac{mg}{L}$ as $CaCO_3$, total alkalinity $\approx 113 \frac{mg}{L}$ as $CaCO_3$, pH ≈ 8.05 and dissolved organic carbon $\approx 2.0 \frac{mg}{L}$ (Bolton Point Water System, 2012). The SRW was pumped into the tube flocculator using a peristaltic pump with multiple pump heads. An airtight 1-liter flow accumulator between the pump and the tube flocculator was used to dampen the periodic pulses caused by the peristaltic pump rollers.

Aluminum sulfate (alum) was metered into the SRW flow by a peristaltic pump upstream from the start of the tube flocculator. Flow through a $120\,cm$ segment of $4.3\,mm$ ($0.17\,in$) ID plastic tubing coiled around a cylinder with an outer diameter of $5\,cm$ acted as a mixing unit to ensure that the alum was thoroughly mixed with the influent SRW stream. The Reynolds number (Re_d) in the mixing unit varied from 1200 to 4640 over the 4 to $15.75\,\frac{mL}{s}$ range of flow rates used in experiments. The results from a dye study showed that adequate mixing was achieved at the lowest flow rate used in experiments.

All information needed to replicate the system is available online, including a materials list and link to Process Controller software (*aguaclara.cornell.edu/wiki*). A description of the Process Controller configuration used to operate the FReTA apparatus is given in Appendix A of Tse (2009). Similar results could be achieved using any number of interfaces between the computer and the hardware.

3.3.4 Software and Operational Controls

The apparatus assembly was controlled and monitored by Process Controller (Weber-Shirk, 2008), a software program written in LabVIEW for automated operation of experiments. Process Controller accepts user and sensor inputs to control the output devices such as valves and pumps. Process Controller is also able to compute logic commands to switch between states and can continuously run and log data from the experimental apparatus autonomously. The Process Controller method used to operate the entire tube flocculator/FReTA apparatus contained six operational states. Each of these states consisted of a different set of inputs, commands and rules controlling the apparatus. The operation of the feedback regulated loop used to maintain constant feedstock turbidity was present in all six of the operational states, because it was critical for the feedstock turbidity to be at steady state. The feedstock turbidity had a coefficient of variation less than $\pm 5\%$. The operational states and controls utilized to automate the entire experimental apparatus were as follows:

The first state was "backwash" in which both FReTA and the tube flocculator were flushed with low-pressure tap water to purge the system in preparation for a new run. The backwash line was connected to the effluent tube originating from the bottom end of the FReTA glass settling column. Water flow was directed

backwards through the FReTA apparatus, flocculator, and rapid mix tubing to dislodge clay and air bubbles trapped on the tube walls or in connectors. The backwash was discharged through a waste tube located between the rapid mix unit and the raw water metering system. The duration of the backwash state was set at two times the hydraulic residence time of the backwash stream inside the flocculator. The backwash state exited to the second state after the backwash state duration elapsed.

The second state was the "loading" state in which the raw water and the coagulant were metered into the apparatus to be flocculated. The flow rates of the raw water and coagulant streams were set by user inputs. The user could choose to have the SRW flow rate and/or coagulant dose step up or down between each cycle of states to compare the results of varying these parameters. The duration of the loading state was twice the combined residence time of the flocculator and the rapid mix.

The third state was the "pump ramp down" state in which the water flow in the apparatus was gradually slowed to a stop by incorporating both the deceleration of the raw water and coagulant pumps and a short period of stopped time. Sudden stoppage of the pumps was observed to generate oscillatory flow caused by exchange of energy between the kinetic energy of the fluid in the flocculator and the pressure inside the flow accumulator. While rapid flow deceleration caused flow oscillation, slow deceleration caused fluid entering the settling column to have experienced a significant part of the flocculator with a lower velocity gradient than the target value. Flow deceleration was controlled by a constant that corresponded to a desired rate of flow decrease. A deceleration of $1.25 \frac{cm}{s^2}$ was used in the tube flocculator.

A stop time proportional to the length of the flocculator was experimentally determined based on data from a pressure sensor across the flocculator (Equation 3.10).

$$Time_{Total} = 8\,s \times \frac{Length_{Flocculator}}{28\,m} + Q \times 0.01\,\frac{m}{s^2} \qquad (3.10)$$

The fourth state was the closing of the ball valve. The ball valve had an electric motor actuator that took six seconds to change between open and close states. The flow was completely stopped before this valve was closed to ensure that no flocs were broken by flow through a constricted orifice.

The fifth state was the "settle" state in which the turbidity of the glass settling column was monitored under quiescent conditions. The duration of the settle state was determined by the desired range of sedimentation velocities. Increasing the duration of the settle state captured smaller sedimentation velocities, as slow settling flocs require more time to clear the measurement volume. Plate settlers used in sedimentation tanks are often designed with critical upward velocities of $0.12 \frac{mm}{s}$ ($10 \frac{m}{day}$). In order to measure particles with settling velocities of $0.12 \frac{mm}{s}$, the settling duration was calculated using Equation 3.1 to be at least 23 minutes. Therefore, a "settle" state duration of 30 minutes was used. The sixth and last state was the reopening of the ball valve in preparation for backwash.

3.4 Data Processing

One of the primary motivations for developing FReTA was the need for a more quantitative assessment of flocculation performance. The raw time series turbidity measurements of the settling suspension permitted qualitative comparisons between different runs. However, some data transformation and curve fitting was needed to permit quantitative comparisons.

As noted above, floc settling velocity was calculated by dividing the $13.64\,cm$ distance between the bottom of the ball valve and the center of the zone illuminated by the turbidimeter infrared LED by the time elapsed in settling (Equation 3.1). Since this transformation is equivalent to taking the reciprocal of the time series, the transformed observations are more concentrated at lower velocities. The data in Figure 3.6a through Figure 3.8 and Figure 3.10 were obtained from FReTA during the settle state of an experiment with 30 NTU influent turbidity (± 4.6 coefficient of variation) in a 56 m flocculator at $G\theta = 40,000$. Average background turbidity during backwash was 0.012 NTU. As shown in Figure 3.6a, little additional information was obtained by observing turbidity changes in FReTA beyond 1500 s. Thus, recording sedimentation velocities much lower than $0.12\,\frac{mm}{s}$ was not considered to be worth the extended sample time required.

Data smoothing and normalization were the next two transformations performed on the raw turbidity data. Dividing the raw turbidity data by the mean effluent turbidity during the loading state normalized the data sets to range between zero and one. This allowed comparison between data sets with differing initial turbidities.

Turbidity fluctuations were observed when large flocs (high sedimentation velocities) moved past the measurement area and refracted more light into the light sensor. Cheng et al. (2010) confirms the correlation between turbidity standard deviation and floc diameter. The large fluctuations were often problematic for data fitting routines and required smoothing (Figure 3.6a and Figure 3.6b).

As seen in Figure 3.7, the raw data points were not equally distributed on the log of sedimentation velocity scale. If smoothed by averaging over a certain number of data points on this scale, the resulting values would not accurately represent the points that were smoothed. Therefore, we chose to smooth the raw data using an average with respect to the time scale (see Figure 3.6b). The number of points that are averaged to create a single smoothed point can be input by the user, 36 points was chosen for the smoothed data in the figures in this paper because it produced a standard 50 points in each experimental data set. The smoothed data set was then converted to a log of sedimentation velocity scale. Figure 3.7 shows the smoothed data with error bars representing one standard deviation in either direction. This smoothing technique allowed for the exclusion of outliers while preserving the shape characteristics of the distribution of sedimentation velocities. Figure 3.8 illustrates the reproducibility of results obtained using FReTA under different experimental conditions.

The normalized turbidity curve in Figure 3.8 can be interpreted as a cu-
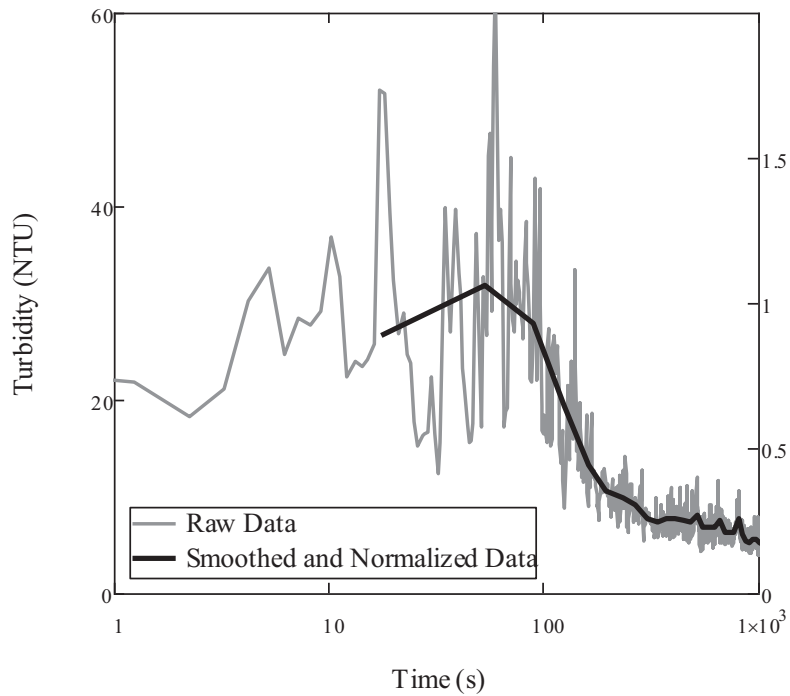
(a) Raw turbidity data and smoothed, normalized data plotted against time (on a log scale). The process for averaging data at regular time intervals is illustrated in Figure 6b.
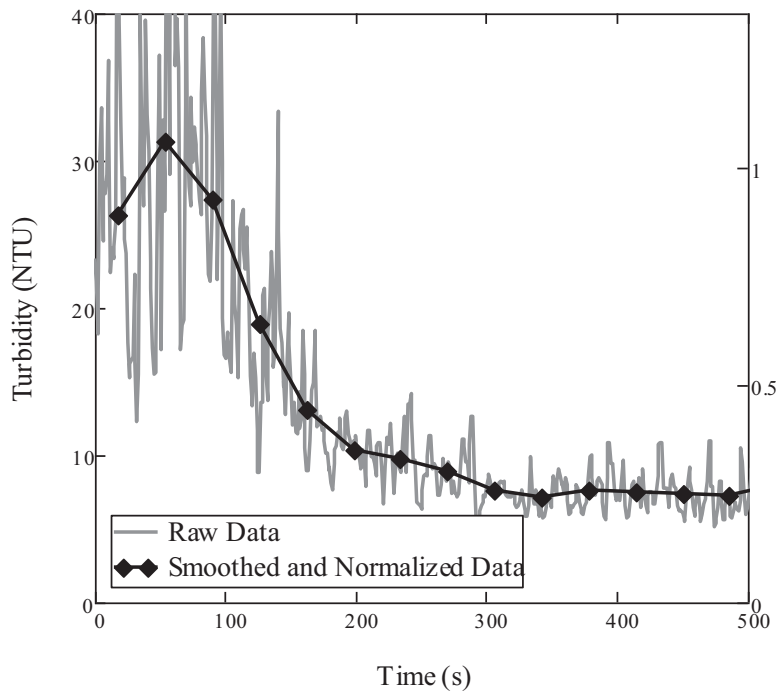
(b) A subset of raw turbidity data and smoothed, normalized data plotted against time to illustrate a sequence of average values calculated at 36 second intervals.

46

Figure 3.6: Data are for a 30 NTU influent turbidity with an alum dose of $5.06 \frac{mg}{L}$ in a $56\,m$ flocculator with $G\theta = 40,000$.
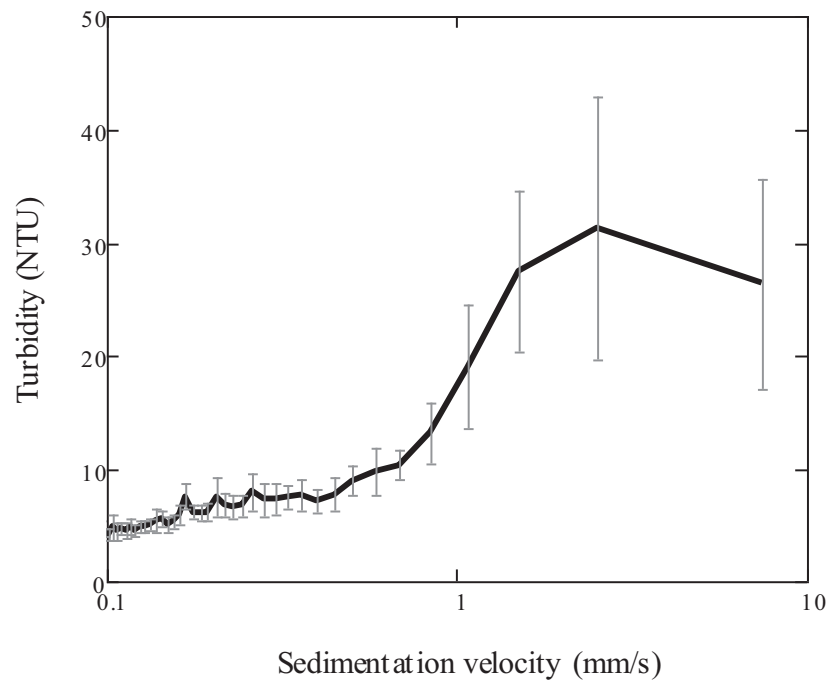
Figure 3.7: Smoothed data with error bars representing one standard deviation above and below the average. Standard deviations are calculated from the 36 data points that are averaged to create each smoothed point.
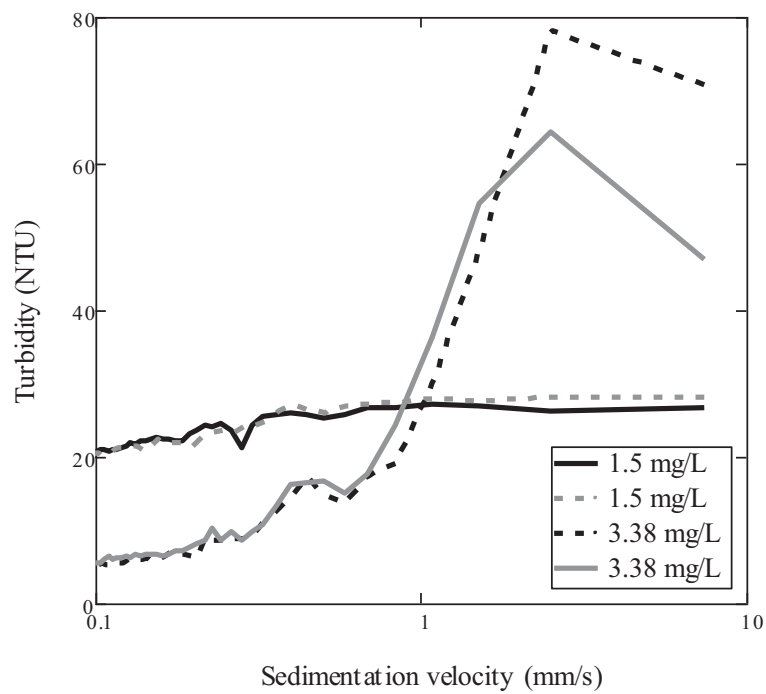
Figure 3.8: Evidence of reproducibility in FReTA experiments at two different alum doses that result in flocculating and non-flocculating datasets. 30 NTU influent water, $82\,m$ flocculator, $G\theta = 60,000$.

mulative distribution function (CDF) of turbidity with respect to V_s. A CDF describes the probability that a variate is less than or equal to some value. Any point on the curve corresponds to a V_s on the abscissa and a value between 0 and 1 on the dependent axis. For instance, if one chooses the point on the curve corresponding to a V_s of $1\frac{mm}{s}$, one can see that it has a normalized value around 0.5—meaning nearly 50% of the particles had a V_s less than or equal to $1\frac{mm}{s}$. Likewise, if one chooses the point on the curve corresponding to a Vs of $0.1\frac{mm}{s}$, it would mean that 15% of the particles had a V_s less than or equal to $0.1\frac{mm}{s}$.

While it is convenient to interpret the plot of normalized turbidity versus V_s as a CDF, there is one aspect of the curve that deviates from the definition of a CDF: the lower bound of the normalized turbidity curve does not approach zero. It is expected that some colloids will never completely settle out even if an infinite amount of time had elapsed. In fact, the final residual turbidity is an important parameter that characterizes how effective flocculation was at sweeping up the raw water colloids. Therefore, in order to interpret the curves as CDFs, an offset equal to the residual turbidity was applied to the fitted distribution curve to allow the lower bound to approach a non-zero value.

This method of analysis becomes more robust if a known type of distribution is fit to the experimental data. Since the turbidity-V_s plot spans multiple orders of magnitude, the curve fit was performed on the base 10 logarithm of V_s in order to make it easier for a regression routine to converge. The gamma distribution was chosen because it provides a flexible shape that can fit many types of distributions with a minimal number of adjustable parameters. The gamma distribution probability density function (PDF) is defined as:

$$f(x, \alpha, \beta) = x^{\alpha - 1} \frac{e^{-x/\beta}}{\alpha^\beta \Gamma(\alpha)} \tag{3.11}$$

where: a is the shape parameter, β is the scaling parameter (both of which must be real and positive), x is the base 10 logarithm of the sedimentation velocity, and the gamma function is defined as

$$\Gamma(\alpha) = \int\limits_0^\infty t^{\alpha - 1} e^{-t} dt \tag{3.12}$$

Therefore, the CDF of the gamma distribution is defined as:

$$F(x, \alpha, \beta) = \int\limits_0^x x^{\alpha - 1} \frac{e^{-x/\beta}}{\alpha^\beta \Gamma(\alpha)} dx \tag{3.13}$$

Equation 3.12 was further modified by an offset parameter (γ) to account for the non-zero lower bound corresponding to non-zero residual turbidity:

$$F'(x, \alpha, \beta, \gamma) = (1 - \gamma) \int\limits_0^x x^{\alpha - 1} \frac{e^{-x/\beta}}{\alpha^\beta \Gamma(\alpha)} dx + \gamma \tag{3.14}$$
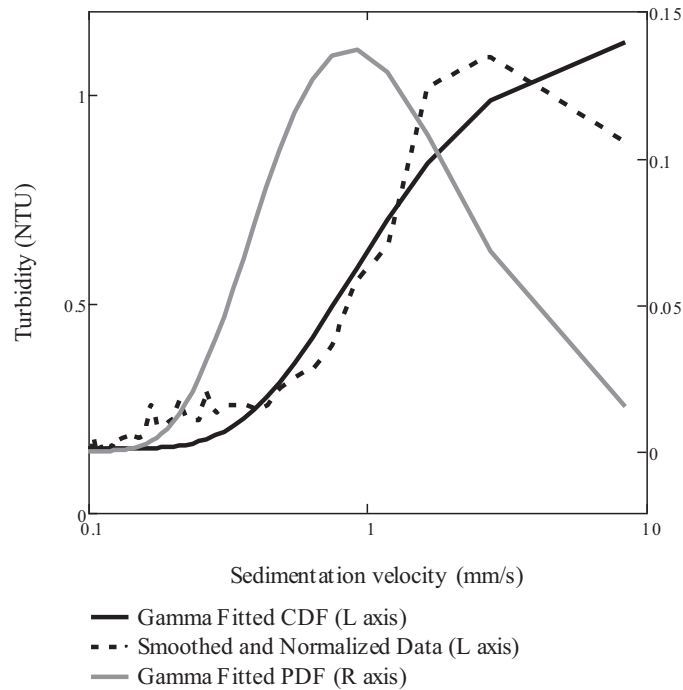
Figure 3.9: Smoothed/normalized data, fitted CDF and fitted PDF.

where log_{10} of the sedimentation velocity was used as the independent variable x. The derivative of the CDF of the gamma distribution provides a probability distribution of the particle population with respect to settling velocities (see Figure 3.9).

Curve fitting was performed using PTC's MathCAD 14.0, an engineering calculation program. MathCAD's curve fitting function (genfit) is capable of fitting a user defined equation to a set of data points using the optimized Levenberg-Marquardt method for minimization. MathCAD arrives at its best fit curve by optimizing the two variables (α and β) in Equation 3.13. The value for residual turbidity, γ, was fixed at the value of the last smoothed point, obtained by averaging the turbidity over the last 36 seconds of the data. The genfit function requires initial guess values for each of the parameters being fitted. A method for estimating α and β by estimating the mean and variance of V_s was developed in order to provide the genfit function with guess values that would allow

convergence. The mean and variance of a gamma distribution are defined as:

$$E\left[x\right] = \alpha\beta \tag{3.15}$$

$$Var\left[x\right] = \alpha\beta^2 \tag{3.16}$$

Therefore, the values of α and β can be estimated by approximating the mean and variance of the normalized turbidity versus sedimentation velocity. The estimate of the mean of $log(V_s)$ was obtained from the sedimentation velocity that corresponded to a normalized turbidity of 0.5. The variance was estimated by picking the two V_s data points with normalized turbidities of 0.25 and 0.75 respectively and computing the $\triangle V_s$ spanned by those two points.

When different datasets were analyzed, it was observed that the fitted CDF graph represented the data very well in some cases while fitting other data quite poorly, particularly at low sedimentation velocities. The occurrence of small flocs in the presence of large, well-formed, flocs that are produced by efficient flocculation is thought to be caused by floc breakup. Large flocs (i.e., those with high V_s) either have not undergone floc breakup or have regrown sufficiently after breakup, while the smaller colloids that have been sheared from the large flocs settle at much lower V_s. Thus, the result of significant floc breakup is to produce a bimodal distribution of settling velocities.

A poor fit of a gamma distribution to the normalized and smoothed data was taken as an indication that the data set was not unimodal. The mean square error (MSE) was calculated in each dataset to differentiate between unimodal and bimodal distributions. The MSE used for this distinction is a user selected parameter. Datasets identified as having bimodal distributions can be fit with a bimodal CDF fitting function. The data processing associated with bimodal fitting is complex and beyond the scope (and space constraints) of this paper.

FReTA is capable of capturing the settling characteristics of different flocculent suspensions. Figure 3.10 shows a very distinct quantitative difference in the settling characteristics of a flocculated 30 NTU raw water associated with different coagulant doses. It is easy to observe that the slight increase in alum dose from 2.25 $\frac{mg}{L}$ to 3.38 $\frac{mg}{L}$ causes rapid flocculation to occur, which is manifest in the significantly lower residual turbidity and higher mean V_s. Figure 3.11 shows the effects of varying $G\theta$ on flocculation at a low coagulant dose. The suspension that experienced a lower $G\theta$ (mean V_s is 1 $\frac{mm}{s}$, residual turbidity 4.4 NTU) has a similar mean sedimentation velocity but a residual turbidity almost twice that of the high $G\theta$ case (mean V_s is 0.92 $\frac{mm}{s}$, residual turbidity 2.3 NTU). This data was processed using the algorithms introduced above to give a more quantitative comparison between the two cases.

3.5 Conclusion

This work was motivated by a need to quantify the sedimentation properties of the effluent from flocculators. FReTA and its accompanying data analysis
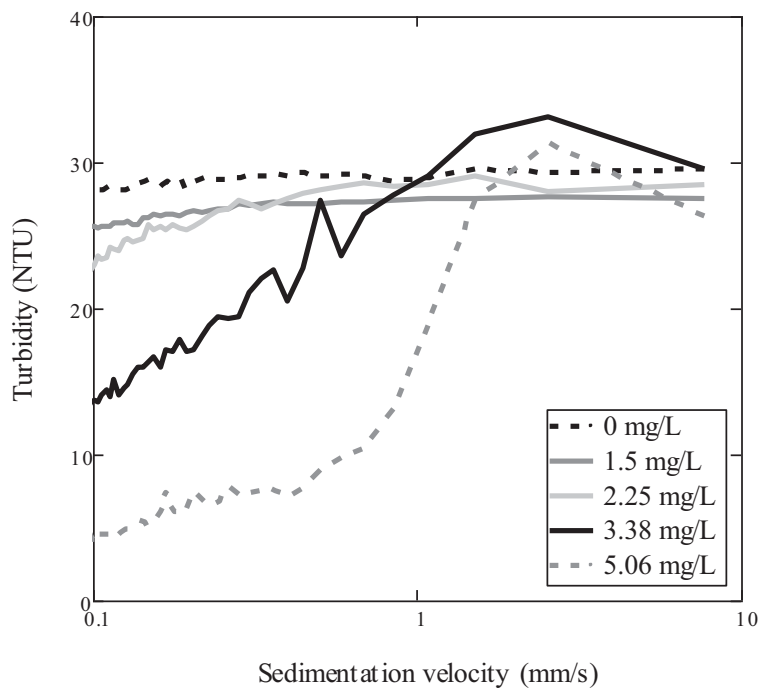
Figure 3.10: Smoothed data sets with varying alum doses.
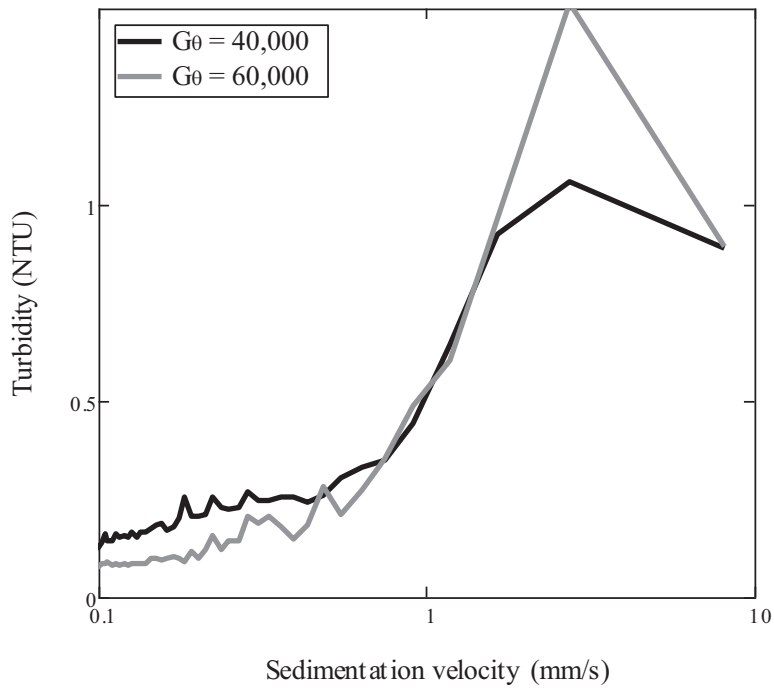
Figure 3.11: Effect of increased $G\theta$ on flocculation. Data is smoothed and normalized. Alum dose is 5.06 $\frac{mg}{L}$ in both cases. When $G\theta = 40,000$, mean V_s is 1.0 $\frac{mm}{s}$, residual turbidity 4.4 NTU. When $G\theta = 60,000$, mean V_s is 0.92 $\frac{mm}{s}$, residual turbidity 2.3 NTU.

methods were developed to quantify both V_s and residual turbidity as a method for comparing the performance of different flocculation conditions. The ability to identify and characterize sedimentation velocity distributions created by floc breakup is a demonstration of FReTA's capabilities. Although FReTA was used here to analyze and compare laminar flow tube flocculator parameters, it could readily be used to compare the performance of full-scale turbulent flow flocculators. FReTA is anticipated to be a very useful tool for engineers and plant operators alike. Experiments using FReTA are currently being carried out to evaluate the contribution of velocity gradients, residence time, and coagulant dose in the formation of rapidly settling suspensions with low residual turbidity.

3.6 References

Adachi, Y. and Tanaka, Y. (1997). "Settling velocity of an aluminum-kaolinite floc." *Water Res.*, 31(3), 449–454.

Berger, S. A., Talbot, L., and Yao, L. (1983). "Flow in curved pipes." *Annual Review of Fluid Mechanics*, 15, 461–512.

Bolton Point Water System (2012). "Drinking water quality report." *Report no.*, Southern Cayuga Lake Intermunicipal Water Commission.

Camp, T. R. and Stein, P. C. (1943). "Velocity gradients and internal work in fluid motion." *J. Boston Society of Civil Engineers*, 30, 219.

Cheng, W., Chang, J., Chen, P., R., Y. R., Huang, Y., and Hsieh, Y. (2010). "Monitoring floc formation to achieve optimal flocculation in water treatment plants." *Environ. Eng. Sci.*, 28(6), 523–530.

Ching, H., Tanaka, T. S., and Elimelech, M. (1994). "Dynamics of coagulation of kaolin particles with ferric chloride." *Water Res.*, 28(3), 559–569.

Cleasby, J. (1984). "Is velocity gradient a valid turbulent flocculation parameter?." *J. Environ. Eng. (Reston, VA, U. S.)*, 110(5), 875–897.

Gregory, J. (1981). "Flocculation in laminar tube flow." *Chem. Eng. Sci.*, 36(11), 1789–1796.

Gregory, J. (1985). "Turbidity fluctuations in flowing suspensions." *J. Colloid Interf. Sci.*, 105(2), 357–371.

McNown, J. S. and Malaika, J. (1950). "Effects of particle shape on settling velocity at low reynolds numbers." *Trans. Amer. Geophys. Union*, 31, 74–81.

Metcalf, L. and Eddy, H. P. (2003). *Wastewater Engineering, Treatment and Reuse*. McGraw-Hill, New York, 4 edition.

Mishra, P. and Gupta, S. N. (1979). "Momentum transfer in curved pipes. 1. Newtonian Fluids." *Ind. Eng. Chem. Proc. D. D.*, 18(1), 130–137.

Robertson, J. A., Cassidy, J. J., and Chaudhry, M. H. (1998). *Hydraulic Engineering*. John Wiley and Sons, Inc.

Tambo, N. and Watanabe, Y. (1979). "Physical characteristics of flocs. i. the floc density function and aluminum floc." *Water Res.*, 13(5), 409–419.

Tse, I. (2009). "Fluid shear influences on hydraulic flocculation systems characterized using a newly developed method for quantitative analysis of flocculation performance, <http://hdl.handle.net/1813/13770>.

Weber-Shirk, M. L. (2008). "An automated method for testing process parameters." *Report no.*, AguaClara Program at Cornell University.

Chapter 4

Influence of Polyaluminum Chloride Self-Aggregation on Flocculation Performance

4.1   Abstract[1]

Polyaluminum chloride (PACl) is a commonly used coagulant for water treatment. One mode of action of PACl ($(AlO_4Al_{12}(OH)_{24}(H_2O)_{12})^{7+}$) is reported to be through formation of aggregates that bridge between colloids. Although many studies have considered the effectiveness of PACl under a spectrum of conditions for influent suspensions, little is known about the rate of formation of PACl aggregates upon mixing with influent water and the effect of aggregate size on the subsequent formation of flocs that can be readily removed by sedimentation. PACl aggregates larger than $0.18\,\mu m$ in diameter were formed under controlled conditions. A kinetic aggregation model was developed and validated to give the aggregate size before mixing with a colloidal suspension and entering a flocculator. After flocculation, the ensuing floc sedimentation velocity and residual turbidity were non-destructively observed. Experimental and modeling results combined with geometric analysis show that, under the experimental conditions tested in this research, PACl self-aggregation consistently lowers attachment efficiency of the colloidal suspension, reduces the effectiveness of the flocculator, and reduces turbidity removal. Minimization of PACl aggregate size is best accomplished by immediate, rapid, and efficient mixing of PACl with the influent water. The relationship between residual turbidity and PACl dose is consistent with expectations based on a geometric adhesive model of coagulation.

4.2 Introduction

In water treatment, coagulation and flocculation are used to form particle aggregates or flocs that can be subsequently removed by sedimentation or filtration. Coagulation increases attachment efficiency, i.e., the fraction of particle collisions that result in aggregation.. Flocculation is the transport phase in which the particles collide and aggregate (Bache and Gregory, 2007). While coagulation in drinking water treatment always involves the addition of a coagulant, the particular chemical, dose, and other relevant conditions determine the attachment efficiency and the ensuing success of coagulation.

4.2.1 PACl Structure and Precipitation

Polyaluminum chloride (PACl) is an inorganic polymer coagulant that has gained wide acceptance for use in water treatment as a result of its efficacy over a broader pH range and at lower temperatures than the commonly used alternative, aluminum sulfate (alum) (Benschoten and Edzwald, 1990). PACl is commonly prepared by the controlled neutralization of aluminum chloride. The dominant stable species in dissolved PACl, $(AlO_4Al_{12}(OH)_{24}(H_2O)_{12})^{7+}$, commonly referred to as Al_{13}, has a Keggin-13 structure and a hydrated radius of $1.2\,nm$ (Ye et al., 2007). When the dose of coagulant exceeds the solubility limit, precipitation occurs. PACl precipitates, or aggregates, are composed of Al_{13} subunits. Benschoten and Edzwald (1990) proved through timed spectrophotometry that the precipitation products of alum and PACl were characteristically different and that PACl precipitates retained their polymeric structure.

Many mechanisms have been proposed for coagulation of suspensions by PACl including: (1) Destabilization of colloidal particles by the nucleation of positively charged Al_{13} precipitates on negatively charged colloidal surfaces, or precipitation charge neutralization (PCN) (Dentel, 1988). PCN is based on the observation that, under the circum-neutral pH of most natural waters, the precipitates of aluminum salts and polymers are positively charged. These species are thought to destabilize negatively charged colloids by attaching and neutralizing their surface charge, thereby decreasing electrostatic repulsion between colloids and inducing aggregation (Ye et al., 2007). (2) As a consequence of the relatively large size and stability of PACl aggregates and their positive charge, electrostatic patch coagulation (EPC) has also been proposed as a potential coagulation mechanism (Ye et al., 2007). EPC is characterized as a localized precipitation charge neutralization mechanism; patches of positive charge are created by aggregates of coagulant adsorbing to a small fraction of the surface of the colloid. Attractive electrostatic forces then attach the positively charged PACl patches to the "naked" surface of other colloids upon collision. It is hypothesized that large flocs can be formed in this manner (Ye et al., 2007; Lin et al., 2008,b). (3) At high coagulant doses, colloidal particles can be removed when they become enmeshed in the voluminous self-aggregated coagulant precipitate, a process called "sweep flocculation"(Bache and Gregory, 2007). The term sweep flocculation is best thought of as a description of the colloid and coagulant sus-

pension and does not provide a mechanistic understanding of why precipitated coagulant should interact with itself or colloids in the observed manner. Sweep flocculation is observed at coagulant doses that are higher than are commonly used in water treatment. Consequently, EPC and PCN are explored in more detail below.

4.2.2 DLVO Theory and Model

The interaction between charged particles in a suspension is cited as the driving mechanism in PCN and EPC and has been modeled by the Derjaguin-Landau-Verwey-Overbeek (DLVO) theory. In this model, Van der Waals interactions are responsible for the attractive force between particles, V_A. V_A is inversely proportional to separation distance between particles and is therefore effective at small separation distances (Equation 4.1) (van Oss et al., 1990).

$$V_A = \frac{-A_H a}{12h} \quad (4.1)$$

where A_H is the Hamaker constant, a is the radius of the particle, and h is the distance between the particles.

Repulsive forces in the DLVO model, V_R, originate when the similarly charged electrical double layers of particles overlap and are proportional to the surface charge squared (Equation 4.2).

$$V_R = 2\pi\epsilon a\zeta^2 exp\left(-\kappa h\right) \quad (4.2)$$

where ϵ is the dielectric constant of water at 298K, ζ is the zeta potential of the particle (see Section 4.2.3 for more detail), and κ is the inverse of the Debye-Huckel length and is given by Equation 4.3.

$$\kappa = \left(\frac{2e^2 N_A I}{\epsilon k_B T}\right)^{1/2} \quad (4.3)$$

where e is the elementary charge of an electron, N_A is Avogadro's number, I is the ionic strength of the solution, k_B is Boltzmann's constant, and T is the temperature.

Attractive and repulsive forces between particles can be summed to find the total force, V_T (Equation 4.4). When V_T is positive (V_R dominates), the area under the curve of V_T as a function of separation distance represents the activation energy, the energy that must be provided to allow two particles to get close enough so that the attractive Van der Waals force dominates.

$$V_T = V_R + V_A \quad (4.4)$$

Application of the DLVO theory to a colloidal suspension suggests that the electrostatic destabilization of colloidal suspensions occurs when the activation energy is reduced so colloids can approach one another. According to PCN and EPC, the goal of coagulation is the electrostatic destabilization of the colloidal

suspension. Electrostatic destabilization can be achieved by changing the surface charge of the colloids, which is incorporated into the DLVO theory by zeta potential, ζ, or through reducing the distance over which repulsive forces act by increasing the ionic strength, I, of the solution. The addition of positively charged coagulant aggregates that adsorb/attach to the surface of the colloid would reduce the surface charge and the resulting energy barrier. Electrostatic attraction would hold the PACl aggregates to the colloidal surface, and the Van der Waals forces accounted for in DLVO theory would be responsible for the inter-particle bond that holds the charge-neutralized colloidal particles together (Lin et al., 1990).

Figure 4.1 depicts the interaction energy of a suspension of kaolin clay at the solution conditions used for experiments in this research. DLVO theory suggests that kaolin clay particles in Cornell tap water would be able to aggregate with a spacing between particles of 10 nm because the van der Waals attractive force exceeds the electrostatic repulsive force at that separation distance. However, a kaolin suspension in Cornell tap water does not create flocs with sedimentation velocities that enable removal in a sedimentation tank without the addition of a coagulant (Figure 4.5 at $0\,\frac{mg}{L}$ coagulant dose). The inability of the DLVO theory to predict the failure of kaolin clay to aggregate suggests that an additional mechanism is important in determining the aggregation behavior of colloids undergoing flocculation.

4.2.3 Measuring charge

Precipitation-charge neutralization (PCN) is hypothesized to facilitate aggregation when the colloid's negative surface charge is near neutral. Surface charge, the electrical charge present at the surface, should be measured as a surface potential, the difference between the electrical potential of the surface and the bulk fluid (outside the electrical double layer). However, counter-ions and water molecules that are strongly bound to the surface of the charged particle interfere with a direct measurement. Zeta potential is the difference in electrical potential between the shear plane and the bulk fluid and is used as a surrogate parameter for surface potential (van Oss et al., 1990). The shear plane is defined as the position where bulk fluid can slip by a moving particle; fluid within the shear plane moves with the particle due to intermolecular forces. It has long been assumed that the shear plane lies near the Stern layer, the monolayer of positive ions from the solution that are attracted to the colloid surface, approximately $0.5\,nm$ from the surface of the colloid. Li et al. (2003) determined the shear plane's distance from the surface to be approximately the the same as the Guoy plane. The Guoy plane is defined by electrochemical composition and is located one Debye length from the colloid surface. The volume created one Debye length ($20-30\,nm$ in a $10^{-4}M$ 1:1 electrolyte solution, and $4.2\,nm$ in the Cornell tap water used for this study) from the surface of the colloid is the volume containing sufficient excess ions of opposite charge to counter act the charge of the particle. It should be noted that while EPC and PCN are based on electrostatic charge neutralization, zeta potential is not an appropriate param-
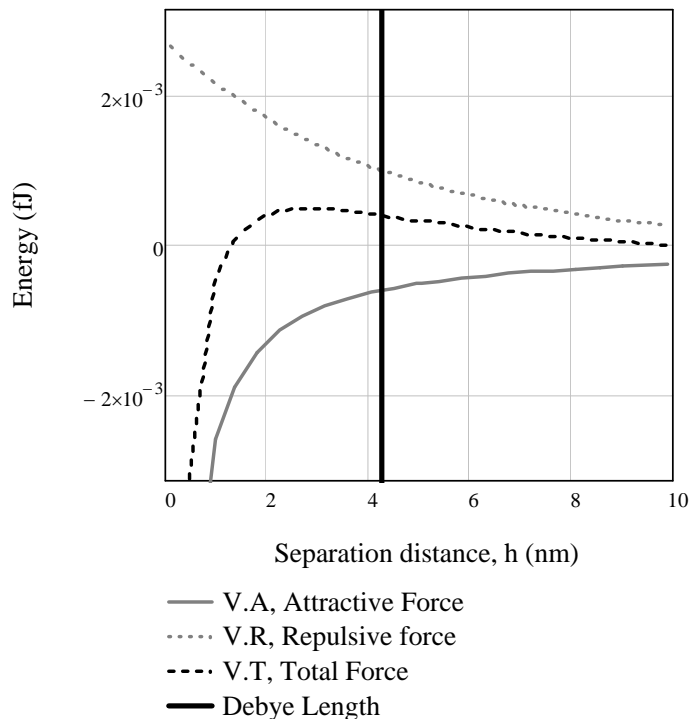
Figure 4.1: Interaction energy for $30\,\frac{mg}{L}$ kaolin clay in Cornell tap water, $\kappa = 0.237\,nm^{-1}$, $a = 1\,\mu m$, $\zeta = -25\,mV$, $0\,\mu M$ Al.

eter for determining the coagulant dose at which EPC will be effective because zeta potential is averaged over the whole surface of the colloid.

4.2.4 Diffusion Limited & Reaction Limited Colloid Aggregation (DLCA & RLCA)

Aggregation often begins with a suspension of mono-disperse particles that collide and form clusters due to Brownian motion (Lin et al., 1990; Asnaghi et al., 1992). These clusters continue colliding due to both Brownian motion and velocity gradients resulting in a suspension of polydisperse clusters. Through static and dynamic light scattering experiments, researchers have found that the aggregation kinetics of many different colloids follow the same pattern (Lin et al., 1990). As a result, colloidal aggregation kinetics have been conceptually divided into two distinct stages - diffusion limited (DLCA) and reaction limited colloid aggregation (RLCA). In DLCA, the aggregation rate is limited only by the rate

of collisions between the particles; this assumes an attachment efficiency near unity. To predict an attachment efficiency near unity for DLCA, the repulsive barrier between two approaching particles must be reduced to much less than $k_B T$, an approximation of the Brownian energy. If the energy barrier is reduced to near zero, the full extent of DLCA can be achieved. In RLCA, collisions are driven by velocity gradients and multiple collisions are required before two particles can stick together (attachment efficiency less than one) resulting in a slower aggregation rate. In all stages of colloid aggregation, the clusters of original colloids (primary particles) take on a fractal structure, with a fractal dimension $d_f \approx 1.8$ for DLCA and $d_f \approx 2.1$ for RLCA (Lin et al., 1990; Asnaghi et al., 1992).

4.2.5 PACl Self-Aggregation Model (DLCA & RLCA)

To interpret the impact of PACl self aggregation on flocculation, a physically-based model was generated to capture the kinetics of Al_{13} self-aggregation in a circum-neutral pH suspension in the absence of other colloids. The primary PACl molecule $((AlO_4Al_{12}(OH)_{24}(H_2O)_{12})^{7+})$ is estimated to be $1.2\,nm$ in diameter (O'Melia et al., 1989). However, because of its propensity to self-aggregate, PACl is rarely observed as individual molecules. PACl obtained from suppliers has already undergone some self aggregation. Therefore, the initial diameter, $d_{initial}$, used in the model was not the diameter of a single PACl molecule, but rather the observed average particle size, $180\,nm$ (determined using a Malvern Zetasizer Nano-ZS, for the PACl used in this research obtained from Zhengzhou City Jintai Water Treatment Raw Material Co., Ltd.). The model provides an estimate of the final size of a PACl aggregate after a specified period of mixing due to collisions resulting from both diffusion and shear (Equation 4.20).

To account for the fractal nature of aggregates (Asnaghi et al., 1992; Lin et al., 2008b; Nan et al., 2009; Weber-Shirk and Lion, 2010), a fractal growth equation was used to determine size of the aggregate particle after each consecutive collision (Equation 4.5). Inherent in this equation is the assumption that all collisions occur between identical particles; such that collisions double the number of the primary particles within the resulting aggregate.

$$d_n = d_{initial} 2^{\frac{n}{D_{Fractal}}} \qquad (4.5)$$

where n is the number of sequential collisions, $D_{Fractal}$ is the fractal dimension, d_n is the aggregate diameter after n collisions, and $d_{initial}$ is initial aggregate diameter. The initial floc volume fraction, $\phi_{initial}$ is calculated by (Equation 4.6).

$$\phi_{initial} = \frac{C_{PACl}}{\rho_{initial}} \qquad (4.6)$$

where C_{PACl} is the concentration of PACl in the PACl aggregation tube used in this research, and $\rho_{initial}$ is the observed density of PACl, $1.138\frac{gm}{mL}$ (see Section

4.2.6). The floc volume fraction for a given collision, ϕ_n, is then calculated as (Equation 4.7):

$$\phi_n = \phi_{initial} \left(\frac{d_n}{d_{initial}} \right)^{3 - D_{Fractal}} \tag{4.7}$$

The effective particle density number, N_n, is determined by dividing the floc volume fraction by the volume of a single aggregate (Equation 4.8).

$$N_n = \frac{\phi_n}{\frac{\pi}{6} d_n^3} \tag{4.8}$$

Given N_n, the model of Meibodi et al. (2010) that assumes Brownian motion and uses the Smoluchowski approach for the collision of particles in a dilute suspension is used to calculate the average time for a given collision, n, $(t_{n,diffusive})$ (Equation 4.9).

$$t_{n,diffusive} = \frac{3\nu}{8 k_B T N_n} \tag{4.9}$$

where ν is the dynamic viscosity of water at $298\,K$. Because of the initial $180\,nm$ aggregate size and concentration used in experiments, shear induced collisions also occur in the reactor and contribute significantly to the final aggregate size. Shear induced collisions are considered RLCA in nature and have an attachment efficiency less than unity. The time for a shear induced collision can be modeled by Equation 4.10, as derived by Weber-Shirk and Lion (2010).

$$t_{n,shear} = \frac{1}{6} \left(\frac{6}{\pi} \right)^{\frac{1}{3}} \left(\frac{\nu}{\varepsilon} \right)^{\frac{1}{2}} \frac{1}{\phi_n^{\frac{2}{3}}} \tag{4.10}$$

In the transitional range between DLCA and RLCA, diffusion and shear transport processes act in concert to cause collisions. Equation 4.11 calculates the collision time when both transport mechanisms are operative.

$$t_n = \frac{1}{\frac{1}{t_{n,diffusive}} + \frac{1}{t_{n,shear}}} \tag{4.11}$$

Each collision time is subtracted in the model from the total experimental reaction time available. Total reaction time was controlled in experiments through laminar flow in a microbore tube of defined length and diameter. When the available reaction time is depleted, the number of collisions is used in the fractal growth equation (Equation 4.5) to give the final aggregate size. The number of sequential collisions was not limited to integer values to obtain the best estimate of the average aggregate size.

The model for diffusion limited PACl aggregate growth was validated experimentally using a Malvern Zetasizer Nano-ZS. A $5\,mM\,Al$ suspension of PACl aggregates was filtered through a $0.2\,\mu m$ syringe filter to isolate a narrow size distribution so as to reduce variability in the observed sizes during aggregation. After filtration, initial aggregates were $55\,nm$ in diameter. As expected, this

is less than the average aggregate size in the unfiltered suspension, $180\,nm$. The suspension pH was adjusted to 7.5 by addition of dilute Na_2CO_3 and a series of size measurements was taken (final PACl concentration $2.5\,mM\,Al$). The sample cell was not mixed during the measurement phase and thus the only transport mechanism for collisions was Brownian motion. Observations of aggregate size immediately after pH neutralization were not obtained because initial collisions occurred at a time scale faster than the start-up detection time required for the Zetasizer ($10\,s$). However, even with the difficulties inherent in observing particle collisions over very short time and length scales, the results (Figure 4.2) suggest that the model based on DLCA is consistent with the observed self-aggregation for PACl.
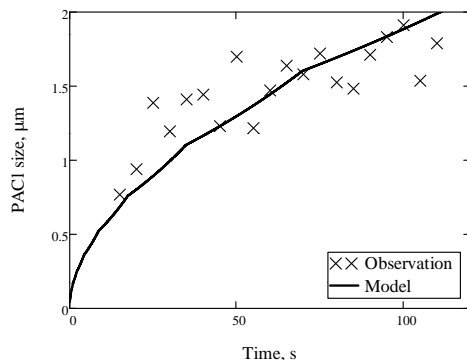
Figure 4.2: Diffusion limited PACl self-aggregation as a function of time at a neutral pH. PACl concentration was $2.5\,mM\,Al$. Measurements exhibit variability because of the polydisperse character of the suspension and because averaging of size measurements was eliminated to decrease the time interval between measurements. The model assumes a fractal dimension of 1.85 for DLCA in the quiescent sample and an initial particle size of $55\,nm$. $R^2 = 0.69$, $n = 20$

4.2.6   Coagulation Geometries

A careful geometric analysis for the attachment of coagulant particles to colloid surfaces can enlighten our understanding of the role of the coagulant on subsequent colloid aggregation. The effectiveness of PACl as a coagulant for negatively charged kaolin clay particles is generally attributed to charge neutralization based on its high positive charge density (Benschoten and Edzwald, 1990; Ye et al., 2007; Wu et al., 2007; Lin et al., 2008; Wu et al., 2009; Lin et al., 2009). However, if the diameter of PACl coagulant aggregates exceeds the Debye length, there is no reason to expect charge neutralization to be a prerequisite of aggregation. This is consistent with observations by Wu et al. (2007); Chu et al. (2008) of flocculation with negative zeta potential (see Section

4.2.7).

As an initial approximation, kaolin clay platelets were assumed to have the volume of a sphere with a diameter of $2\,\mu m$ (Ye et al., 2007; Lin et al., 2008). The platelets were assumed to be cylinders with a 10:1 diameter to height ratio, resulting in a diameter of $3.8\,\mu m$, height of $0.38\,\mu m$, and an initial surface area of $27\,\mu m^2$. The geometries used in Figure 4.3a correspond to a turbidity of 15 NTU ($30\,mg/L$ clay, relationship determined through laboratory observations) and a PACl concentration of $14.4\,\mu M\,Al$, at a pH of 7.5. The number of clay particles present assumes the density of kaolin clay, ρ_{Clay}, is $2.65\,\frac{gm}{mL}$. If initial PACl aggregate diameters are close to $180\,nm$ with a fractal dimension of 2.9 due to aggregation and dehydration that occurred during the manufacturing process (as was the case for the PACl used in this research) the precipitated PACl would cover 14% of the clay surface on average (Figure 4.3a) (Benschoten and Edzwald, 1990; Lin et al., 2011). This calculation assumes that all PACl molecules above the solubility limit precipitate and attach to a clay platelet. At pH 7.5 the solubility limit of PACl is $82\,nM\,Al$ (Benschoten and Edzwald, 1990). If the coagulant is allowed to self-aggregate at circum-neutral pH for 6.2 s under the conditions in this study, $1\,\mu m$ aggregates are formed (see aggregation model below), covering only 4% of the colloid surface (Figure 4.3b). For comparison, the Debye length corresponding to the ionic strength ($I = 5.2\frac{mol}{m^3}$) of Cornell University tap water is $4.2\,nm$. This coupled geometric and DLVO analysis suggests that charge neutralization may not be relevant for PACl dosages typically used in drinking water treatment.

The geometric analysis accounts for the observation that industrial grade PACl is not a monodisperse suspension of primary particles, but rather a suspension of preformed PACl aggregates (Malvern Zetasizer Nano-ZS). The size of these aggregates can vary greatly based on the chemical preparation techniques at the factory including aging times and handling (Benschoten and Edzwald, 1990; Hu et al., 2005; Yan et al., 2008). The industrial grade powdered PACl used in this study (source: Zhengzhou City Jintai Water Treatment Raw Material Co., Ltd) was found to produce a suspension with an initial mean particle size of $180\,nm$ when mixed with distilled water at a concentration of $5\,mM\,Al$ (Malvern Zetasizer Nano-ZS). The fractal dimension for the preformed aggregates was estimated from the bulk density of the PACl granules as described below.

Assuming a porosity, ε, of 0.40 for random packing of spherical particles, Equation 4.12 was used to find the density of the preformed aggregates, $\rho_{initial}$ (German, 1989).

$$\rho_{initial} = \frac{\frac{M_{obs}}{V_{obs}}}{1 - \varepsilon} \tag{4.12}$$

where M_{obs} is the observed mass of a dry sample of the preformed aggregates, and V_{obs} is the observed volume of the sample of preformed aggregates. The observed density, $\rho_{initial}$, was $1.138\,\frac{gm}{mL}$. Next, Equation 4.13 was used to calculate the number of primary particles in a single preformed aggregate, $N_{initial}$.
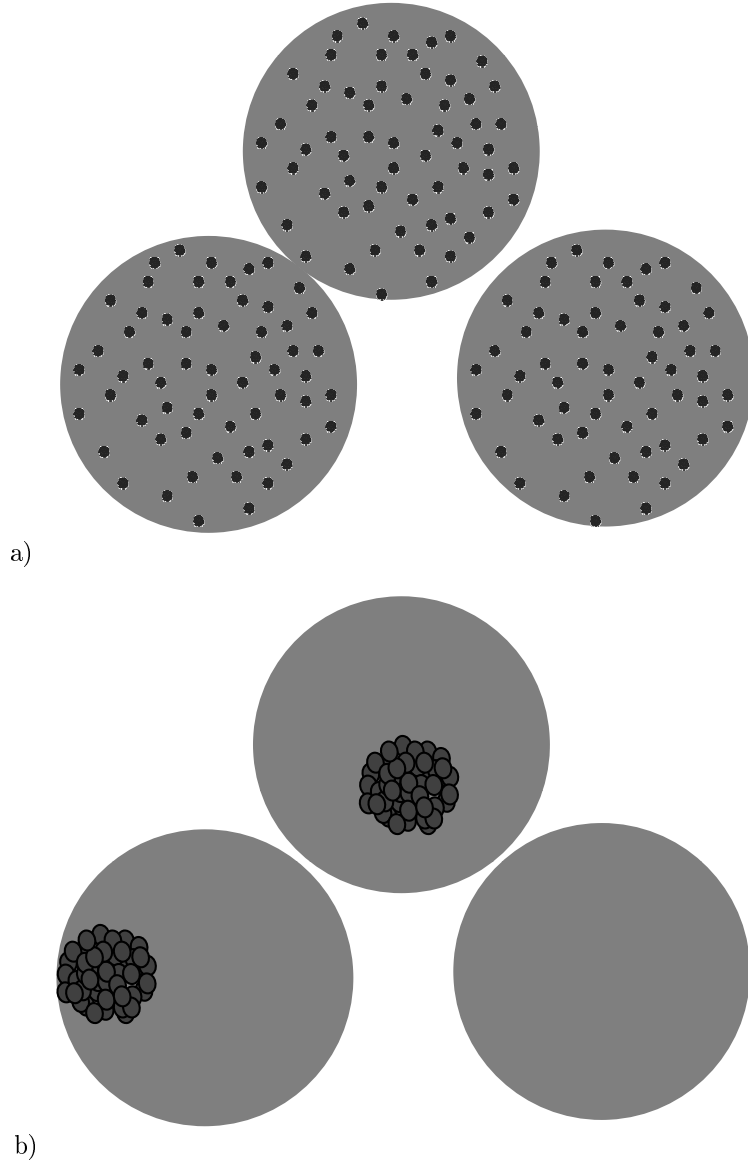
Figure 4.3: Visual geometries, approximately to scale for the experimental conditions in this study, 15 NTU ($30 \frac{mg}{L}$) and $14.4 \mu M$ Al. a) Small aggregates (180 nm) cover 14% of the clay surface with 113 PACl aggregates per clay particle representing the control experiment described in section 4.3, b) Large PACl aggregates (1076 nm) cover 2.4% of the clay surface with 0.65 PACl aggregates per clay particle representing the worst case observed in this study.

$$N_{initial} = \frac{\rho_{initial} V_{initial}}{\rho_0 V_0} \tag{4.13}$$

where $V_{initial}$ is the volume of a spherical preformed aggregate with a $180\,nm$ diameter, ρ_0 is the density of PACl primary particles, $1.907\,\frac{gm}{mL}$, and V_0 is the volume of a single primary particle with a $1.2\,nm$ diameter. The number of binary collisions that must have occurred to create the preformed aggregate was found by Equation 4.14 to be 20.9.

$$Collisions = \log_2(N_{initial}) \tag{4.14}$$

Finally, the fractal dimension, D_F for the factory based aggregation is determined by Equation 4.15.

$$D_F = \frac{Collisions}{\log_2\left(\frac{d_{initial}}{d_0}\right)} \tag{4.15}$$

The resulting fractal dimension determined for the conditions observed in this study is 2.9, signifying that the PACl density was nearly independent of aggregate size in the preliminary aggregation stage during production of the PACl granules at the manufacturer. With this information, it is possible to model the fractional coverage or depth of coagulant on the surface of each clay platelet for a given set of PACl concentrations and geometric considerations. Over the range of doses in this study, increased clay surface coverage causes an increase in attachment efficiency during flocculation, which could easily explain the improvement in turbidity removal (Figure 4.7b). Equations 4.16-4.19 outline the calculations in the geometric model for PACl aggregate coverage of clay.

$$N_{Clay} = Influent\,Turbidity\left(\frac{2\,mg}{L * NTU}\right)\left(\frac{1}{M_{Clay}}\right) \tag{4.16}$$

where N_{Clay} is the number of clay platelets per unit volume, $Influent\,Turbidity$ is the influent turbidity in NTU, $\frac{2\,mg}{L*NTU}$ is a conversion based on laboratory observations, M_{Clay} is the mass of each clay platelet, calculated from the volume given above and the density of kaolin clay, ρ_{Clay}, $2.65\,\frac{gm}{mL}$. The number of binary collisions that must have occurred to create an aggregate of the size dictated by the model, d_{final}, is calculated in Equation 4.17.

$$Collisions = D_{F,initial} \log_2\left(\frac{d_{initial}}{d_0}\right) + D_{F,final} \log_2\left(\frac{d_{final}}{d_{initial}}\right) \tag{4.17}$$

where $D_{F,initial}$ is the fractal dimension of the preformed aggregate, 2.9, d_0 is the diameter of the primary PACl molecule, $1.2\,nm$, $d_{initial}$ is the diameter of the preformed aggregate, $180\,nm$, $D_{F,final}$ is the fractal dimension of the aggregate, and d_{final} is the final diameter of the aggregate determined using Equation 4.5. $D_{F,final}$ is assumed to be equal to $D_{F,initial}$, 2.9, throughout the mixing chamber due to the high velocity gradients. The number of PACl

aggregates per unit volume in the flocculator, N_{PACl}, is calculated by Equation 4.18.

$$N_{PACl} = \frac{C_{PACl,SRW} * N_A}{MW_{PACl} * 2^{Collisions}}$$ (4.18)

where $C_{PACl,SRW}$ is the concentration of PACl in the flocculator, N_A is Avogadro's number, and MW_{PACl} is the molecular weight of PACl. The total volume of PACl aggregates on the surface of a single clay, $V_{PAClperClay}$ is found by (Equation 4.19).

$$V_{PAClperClay} = \frac{V_{PACl,final} * N_{PACl}}{N_{Clay} * (1 - \varepsilon)}$$ (4.19)

where $V_{PACl,final}$ is the volume of a spherical PACl aggregate of diameter d_{final}. The total volume of the PACl aggregates is then used to determine the fractional coverage of the clay platelets. The model output is shown below (see section 4.4). Because PACl aggregates are assumed to be spherical, as opposed to chain-like in structure, larger aggregates have a lower surface area to volume ratio, and will require a larger mass of coagulant to provide sufficient areal coverage of the clay platelets to obtain a high attachment efficiency. Therefore, as PACl aggregates increase in size they will be spaced further apart on the clay platelets, the attachment efficiency will decrease, and the overall particle removal efficiency in flocculation and sedimentation will decrease.

4.2.7 Plausible coagulation mechanisms for aggregated coagulant at low doses

The influence of coagulant dose on zeta potential is well documented in studies of the hypothesized PCN mechanism (Benschoten and Edzwald, 1990; Bache and Gregory, 2007; Li et al., 2007; Wu et al., 2009). The published data, shows that the zeta potential is not zero at the lowest residual turbidity. Results by Wu et al. (2007); Chu et al. (2008) show that residual turbidities drop precipitously at very low doses while the zeta potential remains negative. Similarly, efficient flocculation continues at highly positive zeta potential and the complete lack of correlation between zeta potential and residual turbidity are well documented (Chu et al., 2008). Thus, charge neutralization does not explain the observed results and there must be another mechanism leading to enhanced attachment efficiency.

PACl self-aggregation and the absence of restabilization at positive zeta potentials demonstrates that electrostatic neutrality is not required for aggregation and confirms that the PACl-PACl attachment mechanism is stronger than the electrostatic repulsion. Therefore, although the zeta potential of the colloids becomes more positive as PACl is added to a suspension, there is no evidence that the change in zeta potential or electrostatic charge is what causes the aggregation to be successful. Therefore a different attractive force must be operative to cause aggregation of either negatively or positively charged colloids. The precise nature of the attractive force between the coagulant precipitate and other

67

colloids is not the focus of this paper. However, it is hypothesized that trivalent cations bonded to hydroxides within the Al_{13} molecule have a strong polarity due to the large differences in electronegativity between the trivalent cation and oxygen. The atomic differences in electronegativity produce molecular level charge distributions that would provide strong intermolecular bonding. The attractive force would enable PACl to bond with itself and with clay even when there is electrostatic repulsion. If valid, this hypothesis suggests that the goal of coagulation may be to apply sufficient PACl adhesive to the colloidal particles so that a high fraction of the collision impact sites are coated with coagulant. The observed change in residual turbidity and floc size as the coagulant dose is increased may therefore be the result of the changing fractional coverage of the colloidal surfaces with the PACl adhesive. The geometric analysis given above shows that the PACl aggregates are approximately 40 (180 nm/4.2 nm) times larger than the Debye layer thickness and hence PACl aggregates extend beyond the electric double layer and electrostatic repulsion may not significantly influence the interaction between clay platelets with attached PACl aggregates.

As the geometric analysis in Figure 4.3 illustrates, self aggregation of PACl has a significant influence on the resulting geometry of the colloidal surfaces. If the PACl aggregate size can be kept small, then the coagulant can cover more of the colloid surface and potentially improve the attachment efficiency and turbidity removal. If the PACl is an adhesive, then the geometry of the adhesive on the colloidal surfaces is expected to influence attachment efficiency and there should be no improvement in attachment after the colloids are completely coated. The primary gain in attachment efficiency is expected to occur at low fractional coverage of the colloids.

4.3 Materials and methods

Experiments were conducted using an apparatus comprised of synthetic raw water and coagulant metering systems, a coiled tube hydraulic flocculator, and a flocculation residual turbidity analyzer (FReTA) (see Figure 4.4). Tse et al. (2011b) provide a complete description of the experimental apparatus and methods; only the method for coagulant addition was changed for the experimental data presented here.

Briefly, the synthetic raw water (SRW) metering system consisted of a concentrated stock suspension of kaolinite clay (R.T. Vanderbilt Co., Inc., Norwalk, CT) mixed with tap water to produce a feedback-regulated constant turbidity raw water source (Weber-Shirk, 2008). Reported Cornell University tap water characteristics are: total hardness $\approx 150 \frac{mg}{L}$ as $CaCO_3$, total alkalinity $\approx 136 \frac{mg}{L}$ as $CaCO_3$, pH ≈ 8.2, and dissolved organic carbon $\approx 1.8 \frac{mg}{L}$ (Bolton Point Water System, 2012). The concentrated clay stock and the SRW feedstock were each stirred to ensure homogeneous suspensions. For all of the experiments performed in this study, the SRW was maintained at a constant turbidity of 15 ± 1 NTU, which corresponded to a clay concentration of approximately $30 \frac{mg}{L}$, and a constant temperature, $25°C$. All influent chemicals were
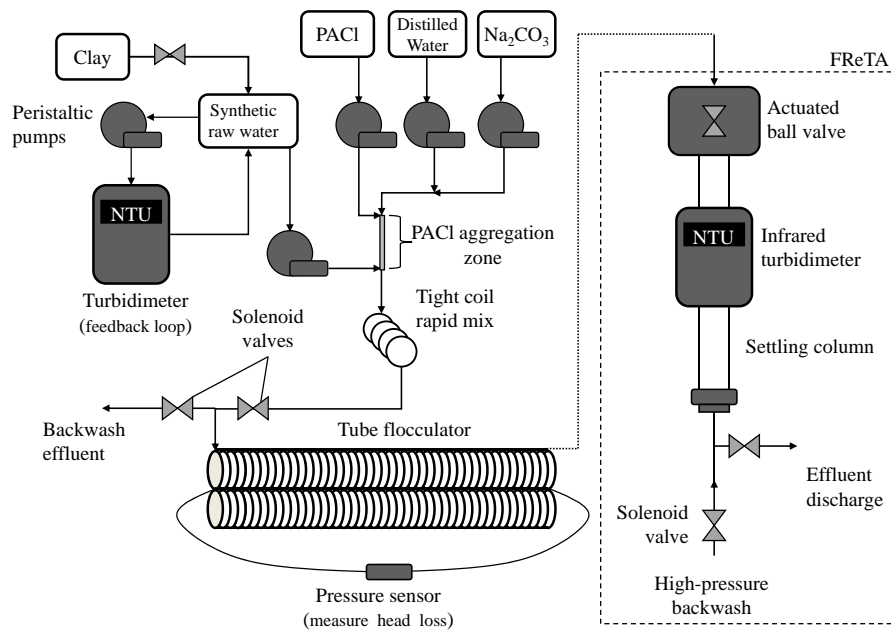
Figure 4.4: Schematic of the experimental assembly.

metered with computer controlled Cole Parmer MasterFlex L/S digital peristaltic pumps. Industry grade (31% as Al_2O_3) polyaluminum chloride (PACl), $(AlO_4Al_{12}(OH)_{24}(H_2O)_{12})^{7+}$, was used as the coagulant for all experiments (Zhengzhou City Jintai Water Treatment Raw Material Co., Ltd). The PACl was diluted with distilled water to give a stock concentration of $5\,mM\,Al$. A Na_2CO_3 stock was used to neutralize the acidic PACl stock and initiate precipitation. The Na_2CO_3 stock was prepared with distilled water at a concentration of $3.43\,mM$; this concentration was chosen because with 1 to 1 mixing it adjusted the PACl stock to pH 7.5. Dilution water was prepared with distilled water and was adjusted to pH 7.5 with $75\,\mu M\,Na_2CO_3$. The dilution water and Na_2CO_3 stock were combined first and then combined with the PACl stock in $0.8128\,mm$ inner diameter micro-bore tubing (Cole Parmer). The flow rate of the dilution stock was varied between experiments to alter the residence time and PACl concentration in the PACl aggregation tube (center of Figure 4.4).

The mixing time provided for PACl self-aggregation was determined by Equation 4.20.

$$t_{Mixing} = \frac{A_{Tube}L_{Tube}}{Q_{PACl} + Q_{Na_2CO_3} + Q_{Dilution}} \qquad (4.20)$$

where A_{Tube} is the cross-sectional area of the micro-bore tubing, $0.519\,mm^2$, L_{Tube} is the length of the micro-bore tubing, $5\,cm$ or $60\,cm$, Q_{PACl} is the flow rate of coagulant stock, $14.4\,\frac{\mu L}{s}$, found by using Equation 4.21, $Q_{Na_2CO_3}$ is the flow rate of base stock, $14.4\,\frac{\mu L}{s}$, and $Q_{Dilution}$ is the flow rate of pH adjusted distilled water stock, which was varied to produce a range of mixing times and concentrations. The micro-bore tubing length was either $5\,cm$ or $60\,cm$ to achieve the full range of mixing times without creating excessive head loss through the tube.

$$Q_{PACl} = \frac{PACl_{Dose}Q_{Plant}}{PACl_{Stock}} \qquad (4.21)$$

where Q_{Plant} is the total flow rate through the flocculator, $5\,\frac{mL}{s}$, $PACl_{Dose}$ is the concentration of PACl in the flocculator, $14.4\,\mu M\,Al$, $PACl_{Stock}$ is the concentration of PACl entering the microbore tubing, $5\,mM$.

The SRW and coagulant was passed through a rapid mix unit comprised of a $120\,cm$ segment of $4.3\,mm$ (0.17') ID tubing coiled around a cylinder with an outer diameter of 5 cm to ensure thorough mixing of the SRW and the PACl. Reynolds number in the rapid mix tube was approximately 1450. Results from a dye study showed that adequate mixing was achieved at this flow rate due to the secondary currents induced by the coiling. The coagulated SRW entered an $84\,m$ coiled tube flocculator. The average velocity gradient in the flocculator, G, was maintained at $50\,s^{-1}$, calculated by Equations 2-9 of Tse et al. (2011b), and the overall plant flow rate was maintained at $5\,\frac{mL}{s}$ resulting in a hydraulic residence time, θ, of $1200\,s$ in the flocculator. As Owen et al. (2008) note, flocculation is frequently studied in batch reactors with offline size measurements for aggregation processes, resulting in poor control over the energy dissipation

rate, reaction time, and questionable size measurements. A tube flocculator was used because it can be idealized as a high Peclet number reactor much like a baffled hydraulic flocculator and also because the average velocity gradient in laminar tube flow is well defined (Weber-Shirk and Lion, 2010). After two hydraulic residence times in the flocculator, $2400\,s$, the peristaltic pumps were ramped to a stop. The FReTA actuated ball valve closed, and the turbidity in the quiescent settling column was measured over a period of 30 minutes. The flocculation residual turbidity analyzer (FReTA) was used to non-destructively measure both the sedimentation velocity and the residual turbidity of the effluent from the flocculator. The settling velocity of the particles was calculated by dividing the 13.64 cm distance between the bottom of the ball valve and the center of the zone illuminated by the turbidimeter infrared LED by the time elapsed during settling. The residual turbidity is defined as the average effluent turbidity in the fifty second interval around the capture velocity of $0.12\,\frac{mm}{s}$ which is a conservatively designed lamellar settler capture velocity (Willis, 1978).

Based on control experiments performed with the tube flocculator at $G\theta = 60,000$, a coagulant dose of $14.4\,\mu M\,Al$ was determined to provide approximately 50% turbidity removal with an initial turbidity of 15 NTU (Figure 4.5). Residual turbidity is comprised of flocs that settle more slowly than the capture velocity, $0.12\frac{mm}{s}$. The $14.4\,\mu M\,Al$ dose was chosen for subsequent experiments. The sensitivity of residual turbidity to changes in coagulant dose enhanced the ability to observe changes in the effectiveness of PACl at different PACl aggregate sizes.

The fractional coverage of the clay by the PACl was calculated using the geometric model and the measured size of the PACl aggregates. The majority of the reduction in residual turbidity was obtained by the first 10% of clay surface coverage. There was negligible improvement in performance above a fractional coverage of approximately 40%. These results are consistent with the expectation that the effectiveness of an adhesive is related to the fractional coverage and that the significant improvement in attachment efficiency, as indirectly measured by residual turbidity, occurs when the colloids are not completely covered.

4.4 Results and discussion

The PACl aggregates ($180\,nm$ in diameter) are many times larger than the Debye length (calculated to be $4.2\,nm$ for the experimental conditions) and thus charge neutralization was not a significant factor in flocculation with powdered PACl. The geometric model and aggregation models were combined to demonstrate the potential role of clay platelet coverage on flocculation performance.

Figure 4.7a depicts the observed relationship between collision potential and turbidity for the tested conditions. In Figure 4.7d the y-axis is pC^*, defined by Equation 4.22. pC^* is the negative logarithm of the fraction of turbidity that remains.
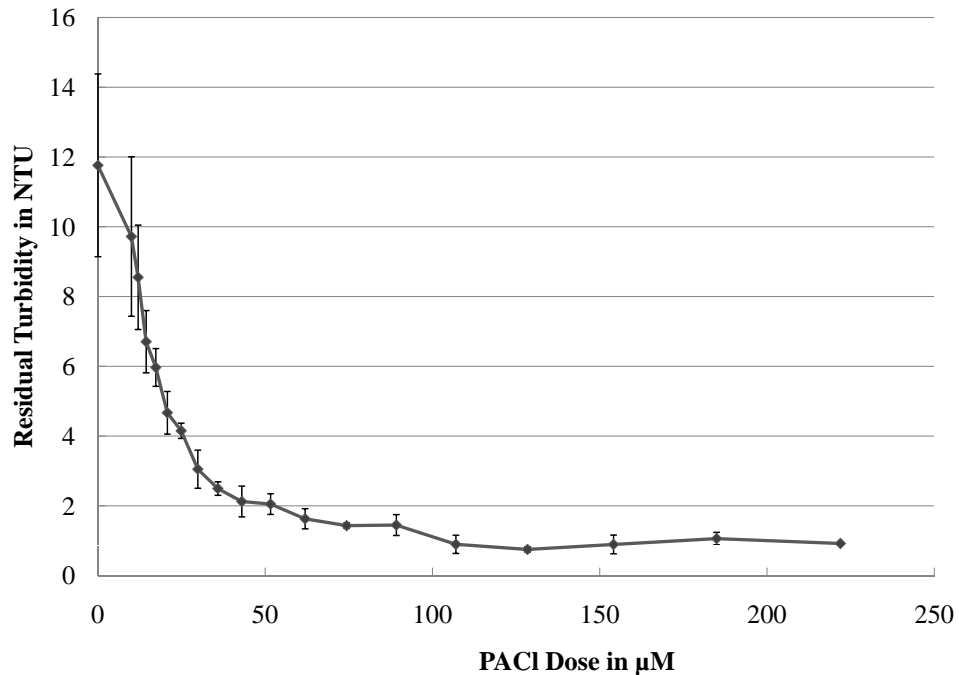
Figure 4.5: Control experiment used to choose the coagulant dose. Error bars represent a 95% confidence interval, n=4.

$$pC^* = -\log\left(\frac{Residual\,Turbidity}{Influent\,Turbidity}\right) \tag{4.22}$$

All calculations of size and fractional coverage incorporate a degree of uncertainty because the attachment efficiency, α, is unknown during self aggregation in the PACl mixing tube. The attachment efficiency term is expected to be low to account for curvilinear particle trajectories (Hendricks, 2009) which were not considered in the collision model. The PACl aggregates have a high fractal dimension and a low porosity and thus flow of water through the aggregate is small and trajectory deflection as particles approach could be significant. Attachment efficiency values ranging from 0.05 to 0.2 were used to calculate the results in Figures 4.7b, 4.7c, and 4.7d. Assumption of higher values of α resulted in the calculation of unreasonably sized PACl aggregates (of the same order of the clay particle size). Attachment efficiencies greater than 0.1 resulted in fewer than 1 PACl aggregate per clay particle and is thus inconsistent with

72
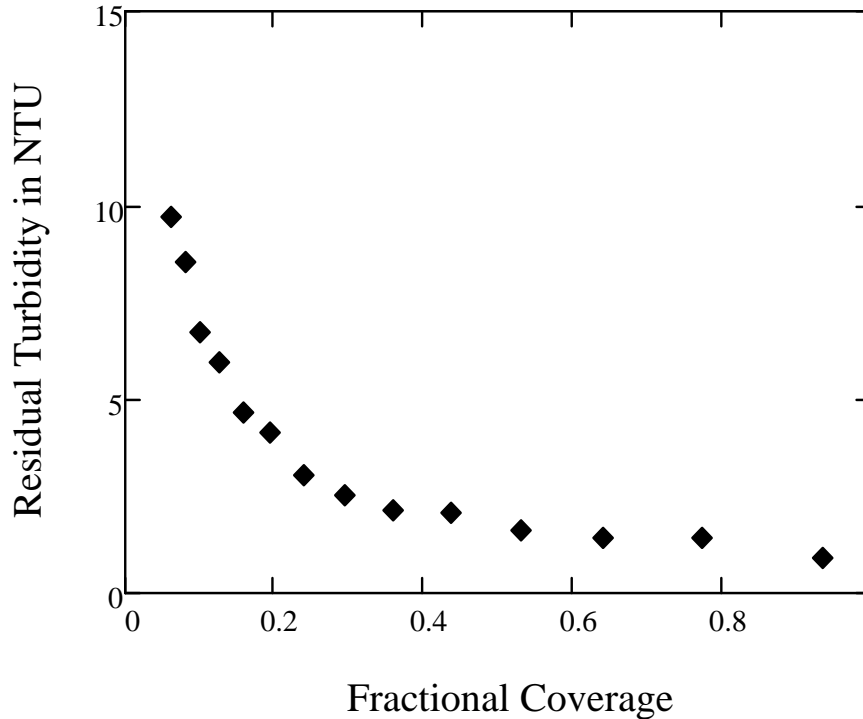
Figure 4.6: Residual turbidity as a function of fractional clay surface coverage by the PACl.

the observed flocculation and sedimentation.

Because mixing time was varied by the addition of dilution water, concentration of PACl in the PACl aggregation tube varied in each test. The parameter $G\theta\phi^{2/3}$, where G is the velocity gradient, θ is the mixing time or residence time in the PACl aggregation tube, and ϕ is the initial floc volume fraction, was chosen to represent collision potential in the mixing tube in accordance with Weber-Shirk and Lion (2010). Since longer mixing times and higher PACl concentrations allow more PACl self-aggregation, the experimental results can also be expressed as a function of model-calculated PACl aggregate size as shown in Figure 4.7b. It is clear that the performance of PACl as a coagulant is impaired by the formation of large PACl aggregates. Given the diameter of model-calculated PACl aggregates, the surface coverage of kaolin clay colloids can be calculated (Equation 4.23) and is shown in Figure 4.7c. For a constant PACl dose, increased aggregate size results in fewer PACl aggregates per clay, which in turn correlates with the decrease in fractional removal shown in Figure

4.7d.

$$Fractional\,Coverage = \frac{V_{PAClperClay}}{SA_{Clay}d_{final}} \qquad (4.23)$$

where SA_{Clay} is the surface area of a single clay platelet and $V_{PAClperClay}$ is the total volume of PACl aggregates per clay platelet given by Equation 4.19.
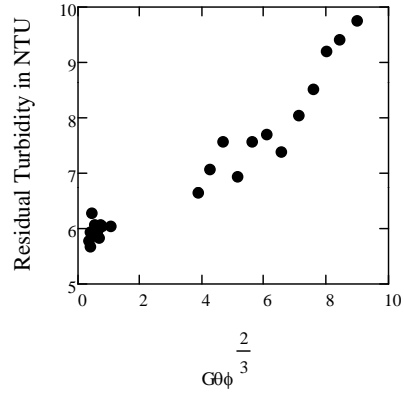
(a) Residual turbidity as a function of collision potential in the PACl aggregation tube, $G\theta\phi^{2/3}$.

◆◆ $\alpha = 0.05$
■■ $\alpha = 0.1$
●● $\alpha = 0.15$
▲▲ $\alpha = 0.25$
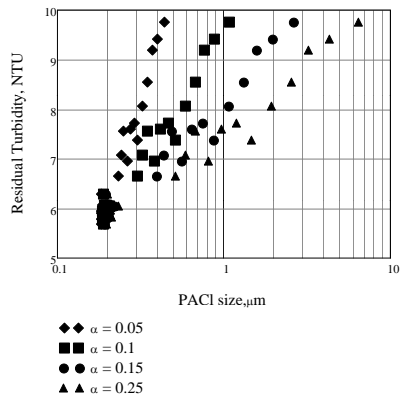
(b) Residual Turbidity as a function of PACl aggregate size for 4 assumed attachment efficiencies.
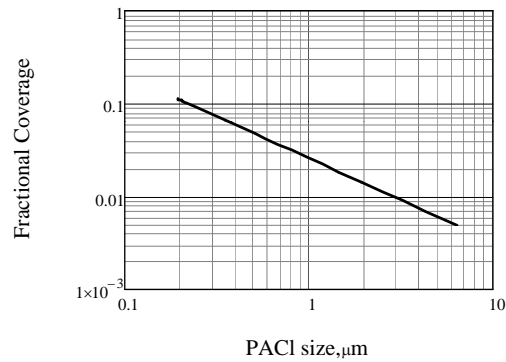
(c) Surface coverage as a function of PACl aggregate size.
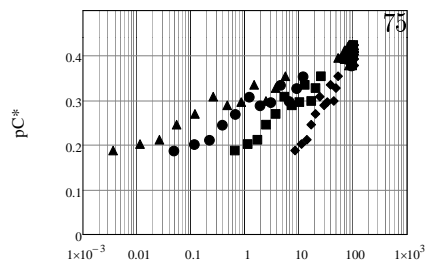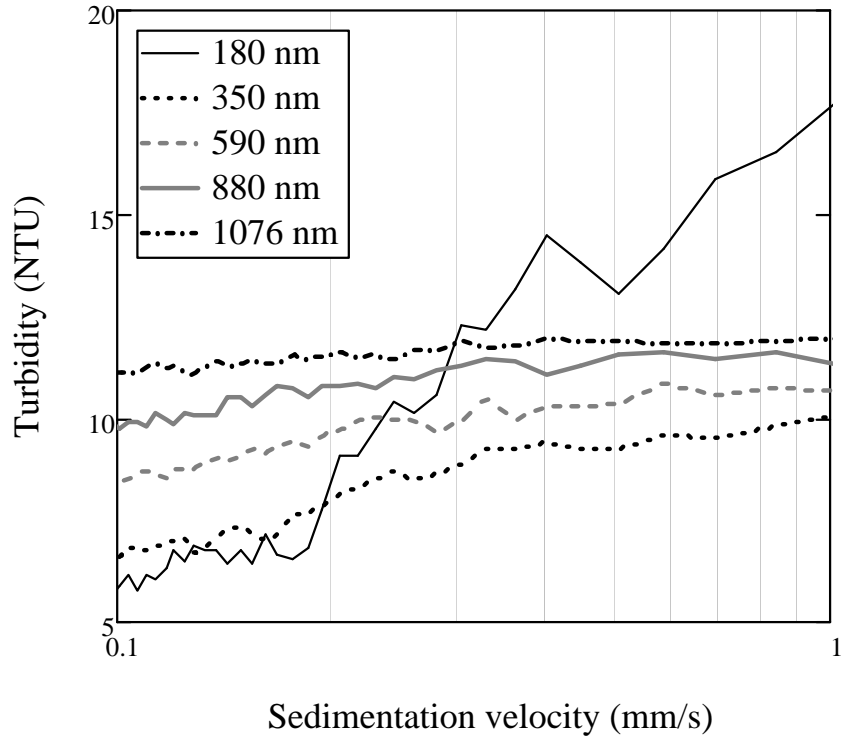
Figure 4.8: Sedimentation velocity from PACl aggregates of various sizes. The vertical line represents the capture velocity, the sedimentation velocity at which the residual turbidity measurement is taken. Data was collected at 1 second intervals for 30 minutes of settling. Each plot consists of 50 data points, each an average of 36 seconds of data.

The data collected from FReTA in each of these experiments can be used to calculate the distribution of sedimentation velocities for the flocs formed under the given conditions. Figure 4.8 shows turbidity as a function of sedimentation velocity for a sample of the aggregate sizes in the study, assuming $\alpha = 0.1$ to estimate the PACl aggregate sizes given in the legend. The sedimentation velocity is strongly correlated to the final floc size and determines the probability that a floc is removed. The slope of the curve represents the fraction of the flocs with the corresponding sedimentation velocity. Residual turbidity is comprised of flocs that settle more slowly than the capture velocity of a conservatively designed lamellar settler in a sedimentation tank, $0.12 \frac{mm}{s}$ in these experiments. Figure 4.8 shows that the fraction of particles with settling velocities lower than $0.12 \frac{mm}{s}$ increased at larger PACl aggregate sizes.

Starting with $180\,nm$ initial aggregates, formation of a $1076\,nm$ PACl aggregate requires approximately 6.2 seconds in the mixing chamber assuming a self-aggregation attachment efficiency of 0.1. As shown in Figure 4.7a, providing PACl time for self-aggregation will decrease the performance of the subsequent flocculation process by decreasing the attachment efficiency in the flocculation phase andincreasing residual turbidity. Therefore, rapid mixing of coagulant with colloid suspensions after coagulant addition is needed to ensure PACl does not self-aggregate before contacting colloids in the water to be treated. PACl will begin to self-aggregate as soon as the PACl stock blends with sufficient raw water to neutralize the pH of the mixture. The dilution required to begin self-aggregation is a function of the acid neutralizing capacity (ANC) of the PACl stock and the ANC and pH of the raw water. Self-aggregation will occur most readily for high pH and high ANC waters such as raw waters in equilibrium with calcium carbonate. Self-aggregation is also favored by high PACl dose and low raw water colloid concentration because the distance between PACl aggregates would be small and the probability of first colliding with a PACl over a clay platelet would be enhanced. If mixing does not occur at the point of coagulant application, the pH of the PACl stock will be neutralized upon entering the water and the local concentration of coagulant will remain high leading to self-aggregation. Self-aggregation after complete mixing with the raw water is expected to be insignificant because PACl aggregate interactions with clay platelets become highly favored over self-aggregation.

While rapid mix of coagulant with raw water has been a prerequisite to flocculation for decades, the results of this study suggest that coagulation with PACl requires immediate, rapid mixing to decrease the local concentration of coagulant at the point of addition. Although beyond the scope of the present study, mixing also aids in the uniform application of the PACl aggregates on the raw water colloid surfaces.

4.5 Conclusions

1. Electrostatic charge neutralization is not required for PACl coagulation because the PACl aggregates are much larger than the Debye length scale.

2. Geometric considerations show the reduction in residual turbidity as a function of PACl dose occurs over a dose range that is consistent with partial clay platelet coverage with adhesive PACl aggregates.

3. PACl will readily precipitate and aggregate at circum-neutral pH in short time scales ($\sim 5\,s$) to sizes that are significant to the performance of the whole water treatment plant.

4. At a constant dose, increased size of PACl aggregates decreases clay surface coverage and negatively affects the performance of subsequent flocculation and sedimentation processes.

5. PACl self-aggregation is not expected to be a factor in municipal water treatment plants once the coagulant is uniformly mixed with the raw water.

The quantitative turbidity removal - PACl aggregation relationships observed in this research are specific to the experimental test conditions and are expected to vary in magnitude with influent water quality and coagulant dose. However, the qualitative effect of coagulant self-aggregation can be generalized and it is clear that PACl aggregate size is a characteristic that should be considered when evaluating the results of flocculation performance experiments. From the perspective of the practical application of PACl to water treatment, this research shows that turbidity removal by flocculation and sedimentation is improved if vigorous mixing occurs at the point of PACl addition. Immediate mixing with a high energy dissipation rate, ε, will increase the separation distance between PACl aggregates and increase the probability that the closest particle which the PACl will attach to is a clay particle, as opposed to another PACl aggregate. Some methods of coagulant addition such as a drip feed into an entrance tank of standing water are expected to not be effective means for rapid dispersal of coagulant. These dosing methods are anticipated to allow self-aggregation of coagulant and necessitate a higher coagulant dose than would be needed if efficient mixing were achieved.

4.6 References

Asnaghi, D., Carpineti, M., Giglio, M., and Sozzi, M. (1992). "Coagulation kinetics and aggregate morphology in the intermediate regimes between diffusion-limited and reaction-limited cluster aggregation." *Phys. Rev. A*, 45(2), 1018–23.

Bache, D. and Gregory, R. (2007). *Flocs in Water Treatment*. IWA Publishing, London, UK.

Benschoten, J. E. V. and Edzwald, J. K. (1990). "Chemical aspects of coagulation using aluminum salts - I. Hydrolytic reactions of alum and polyaluminum chloride." *Water Res.*, 24(12), 1519–1526.

Bolton Point Water System (2012). "Drinking water quality report." *Report no.*, Southern Cayuga Lake Intermunicipal Water Commission.

Chu, Y. B., Gao, B. Y., Yue, Q. Y., and Wang, Y. (2008). "Investigation of dynamic processing on aluminum floc aggregation: Cyclic shearing recovery and effect of sulfate ion." *Sci. China, Ser. B: Chem.*, 51, 386–392.

Dentel, S. K. (1988). "Application of the precipitation-charge neutralization model of coagulation." *Environ. Sci. and Technol.*, 22, 825–832.

German, R. M. (1989). *Particle Packing Characteristics*. Metal Powder Industries Federation, Princeton, NJ.

Hendricks, D. W. (2009). *Fundamentals of Water Treatment Unit Processes: Physical, Chemical, and Biological*. Taylor and Francis 2010036943.

Hu, C., Liu, H., and Qu, J. (2005). "Preparation and characterization of polyaluminum chloride containing high content of Al13 and active chlorine." *Colloids Surf., A*, 260(1-3), 109–117.

Li, H., Wei, S., Qing, C., and Yang, J. (2003). "Discussion on the position of the shear plane." *J. Colloid Interf. Sci.*, 258(1), 40–44.

Li, T., Zhu, Z., Wang, D., Yao, C., and Tang, H. (2007). "The strength and fractal dimension characteristics of alum-kaolin flocs." *Int. J. Miner. Process.*, 82(1), 23–29.

Lin, J.-L., Chin, C.-J. M., Huang, C., Pan, J. R., and Wang, D. (2008a). "Coagulation behavior of Al13 aggregates." *Water Res.*, 42(16), 4281–4290.

Lin, J.-L., Huang, C., Chin, C.-J. M., and Pan, J. R. (2008b). "Coagulation dynamics of fractal flocs induced by enmeshment and electrostatic patch mechanisms." *Water Res.*, 42(17), 4457–4466.

Lin, J.-L., Huang, C., Chin, C.-J. M., and Pan, J. R. (2009). "The origin of Al(OH)3-rich and Al13-aggregate flocs composition in PACl coagulation." *Water Res.*, 43(17), 4285–4295.

Lin, M. Y., Lindsay, H. M., Weitz, D. A., Ball, R. C., Klein, R., and Meakin, P. (1990). "Universal reaction-limited colloid aggregation." *Phys. Rev. A*, 41(4), 2005–20.

Lin, P., Lion, L., and Weber-Shirk, M. (2011). "Comparison of the ability of three coagulants to enhance filter performance." *J. Environ. Eng. (Reston, VA, U.S.)*, 137(5), 371–376.

Meibodi, M. E., Vafaie-Sefti, M., Rashidi, A. M., Amrollahi, A., Tabasi, M., and Kalal, H. S. (2010). "Simple model for thermal conductivity of nanofluids using resistance model approach." *Int. Commun. Heat Mass Transfer*, 37(5), 555–559.

Nan, J., He, W., Song, J., and Song, X. (2009). "Fractal growth characteristics of flocs in flocculation process in water treatment." *2009 Int. Conf. Energy Environ. Technol.*, Vol. 2, State Key Lab. of Urban Water Resource Environ., Harbin Inst. of Technol., Harbin, China, Piscataway, NJ, USA, IEEE, 582–8.

O'Melia, C. R., Gray, K. A., and Yao, C. (1989). "Polymeric inorganic coagulants." *Report no.*, American Water Works Association.

Owen, A. T., Fawell, P. D., Swift, J. D., Labbett, D. M., Benn, F. A., and Farrow, J. B. (2008). "Using turbulent pipe flow to study the factors affecting polymer-bridging flocculation of mineral systems." *Int. J. Miner. Process.*, 87(3-4), 90–99.

Tse, I. C., Swetland, K., Weber-Shirk, M. L., and Lion, L. W. (2011). "Method for quantitative analysis of flocculation performance." *Water Res.*, 45(10), 3075–3084.

van Oss, C. J., Giese, R. F., and Costanzo, P. M. (1990). "Dlvo and non-dlvo interactions in hectorite." *Clays Clay Miner.*, 38(2), 151–159.

Weber-Shirk, M. L. (2008). "An automated method for testing process parameters." *Report no.*, AguaClara Program at Cornell University.

Weber-Shirk, M. L. and Lion, L. W. (2010). "Flocculation model and collision potential for reactors with flows characterized by high peclet numbers." *Water Res.*, 44(18), 5180–5187.

Willis, R. M. (1978). "Tubular settlers-a technical review." *J. - Am. Water Works Assoc.*, June, 331–335.

Wu, X., Ge, X., Wang, D., and Tang, H. (2007). "Distinct coagulation mechanism and model between alum and high Al13-PACl." *Colloids Surf., A*, 305(1-3), 89–96.

Wu, X., Ge, X., Wang, D., and Tang, H. (2009). "Distinct mechanisms of particle aggregation induced by alum and PACl: Floc structure and DLVO evaluation." *Colloids Surf., A*, 347(1-3), 56–63.

Yan, M., Wang, D., Ni, J., Qu, J., Chow, C. W. K., and Liu, H. (2008). "Mechanism of natural organic matter removal by polyaluminum chloride: Effect of coagulant particle size and hydrolysis kinetics." *Water Res.*, 42(13), 3361–3370.

Ye, C., Wang, D., Shi, B., Yu, J., Qu, J., Edwards, M., and Tang, H. (2007). "Alkalinity effect of coagulation with polyaluminum chlorides: Role of electrostatic patch." *Colloids Surf., A*, 294(1-3), 163–173.

Chapter 5

Predictive Performance Model for Hydraulic Flocculator Design with Polyaluminum Chloride and Aluminum Sulfate Coagulants

5.1   Abstract[1]

Mechanistically-based scalable algorithms for design and operation of hydraulic flocculators were developed in this research based on observations of residual turbidity for a range of influent turbidities ($5 - 500\,NTU$) and coagulant doses ($0.01 - 0.15mM\,Al$), for two hydraulic residence times ($800\,s$ and $1200\,s$) and for two coagulant types (polyaluminum chloride and aluminum sulfate). Data were obtained over a range of sedimentation capture velocities using a bench-scale laminar flow tube flocculator and quiescent settling column. Seemingly disparate results were unified through creation of a composite design parameter that considers collision potential in the flocculator and coagulant surface coverage of colloids. One adjustable model parameter was used to fit data ($R^2 \approx 0.9$) from over 136 experiments to create a model for each of the two coagulants. The model is applicable over a range of sedimentation tank capture velocities and accurately reflects the effects of coagulant dose, raw water turbidity, flocculator residence time, and coagulant type. The model was validated by successfully predicting results from independent data sets. When calibrated properly to the coagulant and source water to be treated, the predictive model is expected to

---

[1]The contents of this chapter have been submitted to *Journal of Environmental Engineering*, with co-authors M.L. Weber-Shirk and L.W. Lion.

be a useful tool in the design and operation of hydraulic flocculators.

5.2   Introduction

One objective of flocculation research is to enhance the performance of flocculators in concert with subsequent unit processes (e.g., sedimentation and filtration) while minimizing overall construction and operation costs. Multiple variables influence the performance of hydraulic flocculators in drinking water treatment, including but not limited to: the concentration and type of colloids in the raw water, the concentration of dissolved organic matter, coagulant type and dose, and hydraulic residence time and energy dissipation rate in the flocculator (Kawamura, 1991). Quantifying the effect of varying flocculator design and operational parameters on the post-sedimentation residual turbidity that corresponds to a selected sedimentation tank capture velocity (often referred to as the critical velocity) is a necessary step in differentiating the role each of these parameters play in flocculator performance.

The design and operation of hydraulic flocculators (e.g., units where colloid transport and mixing are achieved by fluid flow rather than by mechanical means) would be aided by a predictive model that can characterize performance of alternative designs under reasonable operating conditions. A general model would be scalable and utilize dimensionally-correct relationships that are based upon relevant flocculation mechanisms. Existing design guidelines for flocculators are predominantly based on empiricism rather than a fundamental understanding of the underlying physical and chemical processes (Hendricks, 2009) and design guidelines for gravity-powered hydraulic flocculators are inadequate (Schulz and Okun, 1984). The evidence for empiricism can be seen in the use of guidelines that are not dimensionless and that cannot be easily made dimensionless. For example, in the Ten State Standards the guidance for the design of flocculator states "The flow through velocity should be not less than 0.5 nor greater than 1.5 feet per second" (Water Supply Committee of the Great Lakes–Upper Mississippi River Board of State and Provincial Public Health and Environmental Managers, 2007). It is well established that floc size is correlated with energy dissipation rate (not velocity) (Cleasby, 1984; Akers et al., 1987; Weber-Shirk and Lion, 2010) and thus, if the goal of these guidelines is to be able to deliver flocs of a certain size to the sedimentation tank, then the design specification should be a maximum energy dissipation rate. Since the relationship between energy dissipation rate and velocity is dependent on the scale of the flow, velocity guidelines result in design failure for small scale facilities. The pervasive lack of scalable design guidelines provides an opportunity for research to significantly improve conventional flocculator designs.

In this research a spectrum of coagulant doses (which control colloid surface coverage), and influent turbidities, were evaluated for two alternative coagulants and two hydraulic residence times with respect to their influence on floc settling properties (as manifested by residual turbidity) at multiple sedimentation capture velocities. The observations from these experiments are utilized

to formulate a comprehensive model that is able to predict settled water turbidity as a function of flocculator design and operation for laminar flow tube flocculators.

5.3   Experimental Methods

Experiments were conducted using an apparatus comprised of synthetic raw water and coagulant metering systems, a coiled tube hydraulic flocculator, and a flocculation residual turbidity analyzer (FReTA) (see Figure 5.1). Tse et al. (2011b) provide a complete description of the experimental apparatus and methods; only the length of the flocculator was changed for the experimental results presented here.
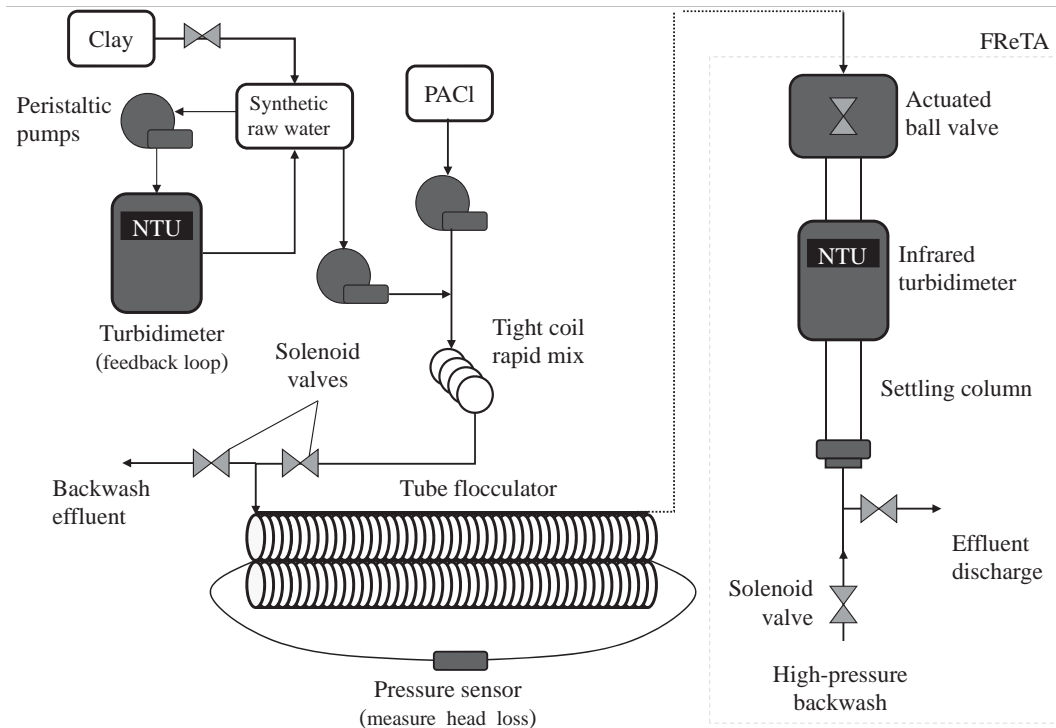
Figure 5.1: Schematic of the experimental assembly.

Briefly, the synthetic raw water (SRW) metering system consisted of a concentrated stock suspension of kaolinite clay (R.T. Vanderbilt Co., Inc., Norwalk, CT) mixed with tap water to produce a feedback-regulated constant turbidity raw water source (Weber-Shirk, 2008). Reported Cornell University tap water characteristics are: total hardness $\approx 150\,\frac{mg}{L}$ as $CaCO_3$, total alkalinity $\approx 121\,\frac{mg}{L}$ as $CaCO_3$, pH ≈ 7.6, aluminum $= 0\,to\,0.17\,\frac{mg}{L}$, and dissolved organic carbon $\approx 1.7\,\frac{mg}{L}$ (Bolton Point Water System, 2012). The concentrated clay stock and the SRW feedstock were each continuously stirred to ensure homogeneous suspensions. Influent turbidities of 5, 15, 50, 150, and 500 NTU were tested with both PACl and alum over a range of coagulant doses ($\sim 0.01-0.15\,mM\,Al$). All influent chemicals were metered with computer controlled Cole Parmer MasterFlex L/S digital peristaltic pumps. To better mimic coagulants used in water treatment practice, industry grade (31% as Al_2O_3) polyaluminum chloride (PACl), $(AlO_4Al_{12}(OH)_{24}(H_2O)_{12})^{7+}$ (Zhengzhou City Jintai Water Treatment Raw Material Co., Ltd.), and technical grade aluminum sulfate, $Al_2\,(SO_4)_3{\cdot}14.3H_2O$, (PTI Process Chemicals) were used as coagulants for all experiments. Each coagulant was diluted with distilled water to make the stock solutions.

The SRW and coagulant were passed through a rapid mix unit comprised of a $120\,cm$ segment of $4.3\,mm$ (0.17") ID tubing coiled around a cylinder with an outer diameter of 5 cm to ensure thorough mixing. Reynolds number in the rapid mix tube was approximately 1450. Results from a dye study showed that adequate mixing was achieved at this flow rate due to the secondary currents induced by the coiling.

The mixed coagulant and SRW entered a coiled tube flocculator ($56\,m$ or $84\,m$). The average velocity gradient in the flocculator, G, was maintained at $51\,s^{-1}$, calculated using relationships for laminar flow in coiled tubes described by Tse et al. (2011b) (see equations 5.1-5.4 below). The overall plant flow rate, Q_{Plant}, was maintained at $5\,\frac{mL}{s}$ resulting in flocculator hydraulic residence times, of $800\,s$ and $1200\,s$ respectively. As Owen et al. (2008) note, flocculation is frequently studied in batch reactors with offline size measurements for aggregation processes, resulting in poor control over the energy dissipation rate, reaction time, and questionable size measurements. A tube flocculator was used in this research because it can be idealized as a high Peclet number reactor much like a baffled hydraulic flocculator and also because the average velocity gradient in laminar tube flow is well defined (Weber-Shirk and Lion, 2010).

After two hydraulic residence times in the flocculator, the flow was ramped to a stop, the FReTA actuated ball valve shown in Figure 1 closed, and the turbidity in the quiescent settling column was measured over a period of 30 minutes. FReTA was used to non-destructively measure both the sedimentation velocity and the residual turbidity of the effluent from the flocculator. The settling velocity of the particles was calculated by dividing the 13.6 cm distance between the bottom of the ball valve and the center of the zone illuminated by the turbidimeter's infrared LED by the time elapsed during settling. The residual turbidity was defined as the average settled turbidity in the fifty second interval around the selected capture velocity. Because turbidity was recorded continuously as the suspension settled, capture velocities between $2.7\,\frac{mm}{s}$ and $0.08\,\frac{mm}{s}$ can be specified when the data is analyzed.

5.4   Model

Conceptually, a successful flocculation model would determine effective collisions, collisions that result in particle aggregation, as a function of floc size for a given set of conditions. Since these parameters are not readily observable within a flocculator, measurable alternatives must be used. The dimensionless term $G\theta$ has been used as a measure of the collision potential provided by a flocculator that experiences laminar flow, where G is proportional to the rate of collisions and θ is the total time over which collisions occur (Cleasby, 1984). Equations 5.1 through 5.4 can be used to calculate G for a coiled flocculator, as described in Tse et al. (2011b).

$$\bar{G} = \frac{64 Q_{Plant}}{3\pi d_{Tube}^3} \tag{5.1}$$

$$Re = \frac{4Q_{Plant}}{\pi d_{Tube} \nu} \tag{5.2}$$

$$De = \sqrt{\frac{0.5 d_{Tube}}{R_{Bend}}} Re \tag{5.3}$$

$$G = \bar{G} \left(1 + 0.033 log(De)^4\right)^{0.5} \tag{5.4}$$

where: $\bar{G}$ is the average velocity gradient in a straight tube, Q_{Plant} is the plant flow rate, d_{Tube} is the diameter of the tube flocculator, Re is the Reynolds number, ν is the viscosity of water, De is the Dean number, and R_{Bend} is the radius of the coil in the flocculator. In laminar flow G is related to the energy dissipation rate , ε, by Equation 5.5. The experimental G of $51\,s^{-1}$ corresponds to $\varepsilon = 2.6 \frac{mW}{kg}$.

$$\varepsilon = \nu G^2 \tag{5.5}$$

It is well known that not all collisions between suspended particles are effective, i.e., they do not all result in aggregation. Attachment efficiency, α, has been used to designate the fraction of collisions which result in aggregation. Unfortunately, α is not directly measurable or easily estimated. However, the fractional coverage of the colloid surface by coagulant can be estimated based on the geometric properties of the colloids and coagulant and is used here as an alternative for attachment efficiency. Given the influent clay concentration, $C_{Influent}$, the coagulant concentration, C_{PACl} or $C_{Al(OH)_3}$, and the coagulant aggregate size, d_{PACl} or $d_{Al(OH)_3}$, the number of coagulant aggregates per clay platelet can be calculated (see Equation 5.6). As an initial approximation, kaolin clay platelets were assumed to have the volume of a sphere with a diameter of $2\,\mu m$ (Ye et al., 2007; Lin et al., 2008). The platelets were assumed to be cylinders with a 10:1 diameter to height ratio, resulting in a diameter of $3.8\,\mu m$, height of $0.38\,\mu m$, and an initial surface area of $27\,\mu m^2$. PACl aggregate diameters were determined experimentally to be approximately $180\,nm$ (using a Malvern Zetasizer Nano-ZS). Amorphous $Al(OH)_3$ precipitate particles were estimated to be $100\,nm$ in diameter, but model calculations were not sensitive to this assumption (see discussion below). Since PACl is used as a coagulant by the Cornell water treatment plant, the solubility limit for aluminum was satisfied for the tap water entering the experimental system (Bolton Point Water System, 2012). The experiments used to create the model were performed over several months and the soluble aluminum concentration in the source water likely varied as indicated in the reported water characteristics ($0 - 0.17 \frac{mg}{L}$), which may contribute to the spread of the data. As a result, the solubility limit was assumed to be satisfied and was not subtracted from the dose administered in experiments. However, this adjustment should be made in cases where the raw water has yet to be dosed with coagulant as is shown in Equation 5.6. Benschoten and Edzwald (1990) report the pH-dependent solubility of PACl and amorphous $Al(OH)_3$.

$$N_{perClay} = \frac{\left(C_{Coag} - C_{Coag(aq)}\right) V_{Clay}\rho_{Clay}}{\frac{\pi}{6}d_{Coag}^3 \rho_{Coag} C_{Influent}} \tag{5.6}$$

where $N_{perClay}$ is the number of coagulant aggregates per clay, C_{Coag} is the concentration of coagulant, $C_{Coag(aq)}$ is the solubility of the coagulant at the appropriate pH, V_{Clay} is the volume of a clay platelet, ρ_{Clay} is the density of clay, $2.65\,\frac{gm}{mL}$, d_{Coag} is the diameter of a coagulant aggregate, $d_{PACl} = 180\,nm$ and $d_{Al(OH)_3} = 100\,nm$, ρ_{Coag} is the density of the coagulant, $\rho_{PACl} = 1.138\,\frac{gm}{mL}$ based on laboratory measurement and $\rho_{Al(OH)_3} = 2.42\,\frac{gm}{mL}$ as reported by IPCS (1998), and $C_{Influent}$ is the influent turbidity in $\frac{mg}{L}$. Turbidities were translated from NTU to $\frac{mg}{L}\,Clay$ using a conversion based on laboratory observations, $2\,\frac{mg}{L*NTU}$.

The above calculation of coagulant aggregates per clay colloid does not account for the possible attachment of coagulant to the walls of the experimental flocculation tube. In the bench-scale of laboratory experiments the inner surface of the flocculation tube can be a significant coagulant sink, a place where the coagulant will adhere and be removed from all subsequent processes. The fraction of coagulant aggregates that adhere to colloids in the suspension, R_{Clay}, (i.e. those that do not adhere to the flocculator tube wall) can be estimated by Equation 5.7.

$$R_{Clay} = \frac{SA_{ClayTotal}}{SA_{ClayTotal} + SA_{Wall}} \tag{5.7}$$

where SA_{Wall} is the surface area of the tube wall of the flocculator, $SA_{ClayTotal}$ is the surface area of all the clay colloids in a liquid volume equal to that of the flocculator (Equation 5.8). SA_{Wall} is a function of the length of flocculator tube, L_{Tube}, and the circumference of the flocculator tube, πd_{Tube} (Equation 5.10).

$$SA_{ClayTotal} = L_{Tube}\frac{\pi}{4}d_{Tube}^2 SA_{Clay} N_{Clay} \tag{5.8}$$

$$N_{Clay} = \frac{C_{Influent}}{\rho_{Clay}V_{Clay}} \tag{5.9}$$

$$SA_{Wall} = L_{Tube}\pi d_{Tube} \tag{5.10}$$

where $C_{Influent}$ is the raw water clay concentration, N_{Clay} is number of clay colloids per unit volume of suspension, and SA_{Clay} is the surface area of a single clay platelet.

After substitution, Equation 5.7 becomes:

$$R_{Clay} = \frac{SA_{ClayTotal}}{SA_{ClayTotal} + SA_{Wall}} = \frac{\frac{1}{4}d_{Tube}SA_{Clay}N_{Clay}}{\frac{1}{4}d_{Tube}SA_{Clay}N_{Clay} + 1} = \frac{1}{1 + \frac{4}{d_{Tube}SA_{Clay}N_{Clay}}} \tag{5.11}$$
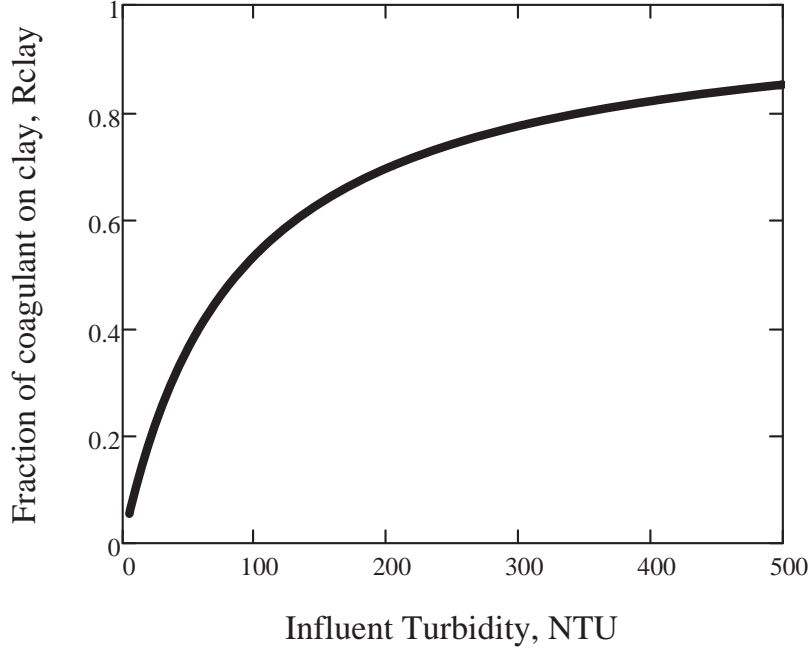
Figure 5.2: The fraction of coagulant aggregates that adhere to the surface of clay colloids in the experimental apparatus, R_{Clay}, as a function of influent turbidity

The length of the flocculator tube drops out of the equation and thus the length of the zone where free coagulant aggregates are present is not needed to determine the distribution of the coagulant between the flocculator tube and the clay. The correction for wall losses expressed as fraction of coagulant available to react with clay is shown in Figure 5.2 as a function of influent turbidity.

Surface coverage of clay can also be reduced if coagulant particles stick to a clay surface that is already occupied by coagulant. A Poisson distribution was used to estimate the reduction in coverage due to coagulant aggregates stacking on top of one another instead of attaching to uncovered clay surface (Equation 5.12).

$$\Gamma = 1 - e^{\frac{-d^2_{Coag}}{SA_{Clay}}N_{perClay}R_{Clay}} \tag{5.12}$$

where SA_{Clay} is the surface area of a single clay platelet. A parallel analysis was performed using a random number generator to consecutively place each coagulant aggregate on a discretized grid. The ratio of occupied to total spaces on the grid gave an estimate of the fractional clay coverage that agreed with Equation 5.12. The effect of stacking is shown in Figure 5.3 and becomes significant at

89

high coagulant doses.
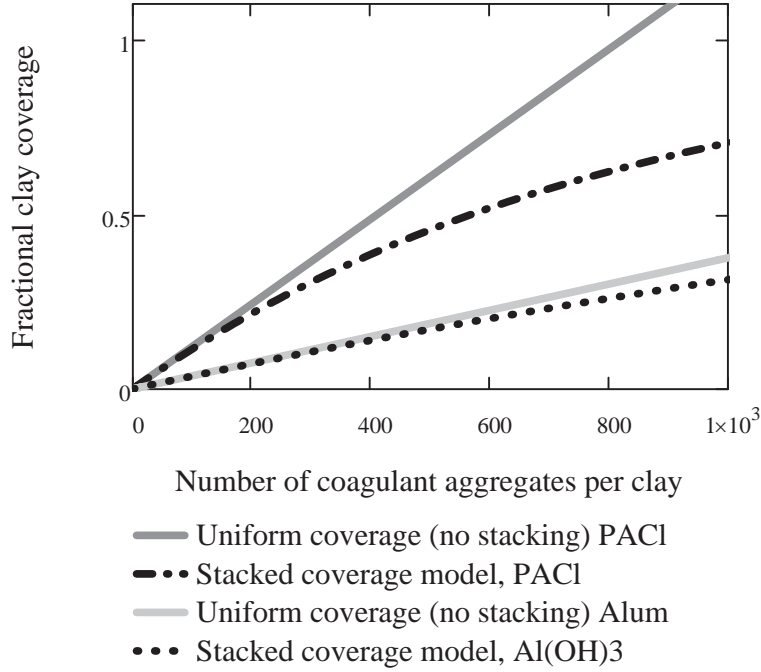
Figure 5.3: Fractional clay surface coverage for PACl and $Al(OH)_3$.

With quantifiable parameters for collisions provided by the flocculator ($G\theta$) and surface coverage (Γ) as a measure of the probability of attachment, the properties of the suspension must be incorporated into the model. The floc volume fraction, ϕ, gives the fraction of the volume of the suspension occupied by the combination of influent particles and precipitated coagulant. (Equation 5.13).

$$\phi = \frac{C_{Coag}R_{Clay}}{\rho_{Coag}} + \frac{C_{Influent}}{\rho_{Clay}} \tag{5.13}$$

The coagulant doses used in experiments contributed less than 2.5% to the floc volume fraction and thus Equation 5.13 can be simplified to:

$$\phi = \frac{C_{Influent}}{\rho_{Clay}} \tag{5.14}$$

In laminar flow flocculators the velocity between flocs scales with the average separation distance between flocs. The time between floc collisions is inversely proportional to ϕ and directly proportional to the velocity between flocs (or the separation distance or $\phi^{1/3}$). The result is that for laminar flow the average time for floc collisions scales with $\phi^{2/3}$ (Weber-Shirk and Lion, 2010).

Based on the above analysis, the product of the dimensionless model parameters, $G\theta\Gamma\phi^{2/3}$ was selected to characterize the number of effective collisions provided by a laminar flow tube flocculator. The dependent parameter of interest is the negative log of the fraction of clay particles remaining after the combined flocculation/sedimentation processes (Equation 5.15).

$$pC^* = -log\left(C^*\right) = -log\left(\frac{C_{Settled}}{C_{Influent}}\right) \qquad (5.15)$$

where $C_{Influent}$ is the raw water clay concentration and $C_{Settled}$ is the settled water clay concentration after a settling time, $t_{Capture}$. In practice $t_{Capture}$ is set by the hydraulic residence time and geometry of the tube or plate settlers in the sedimentation tank. Experimentally $t_{Capture}$ was set in data analysis by the selection of a capture velocity, $V_{Capture}$ (Equation 5.16).

$$t_{Capture} = \frac{h_{column}}{V_{Capture}} \qquad (5.16)$$

where h_{Column} is the distance between the top of the settling column and the point within the turbidimeter where turbidity was measured. Tse et al. (2011b) provide a detailed description of analysis of the data acquired by FReTA.

The experimental results were first modeled by Equation 5.17 where m is the slope, and b is the intercept.

$$pC^* = m\,log\left(G\theta\Gamma\phi^{2/3}\right) + b \qquad (5.17)$$

The fraction of clay particles remaining as residual turbidity was inversely proportional to $G\theta\Gamma\phi^{2/3}$ allowing the value of m to be set equal to 1. Using a slope of 1 for the model reduced the number of fitted parameters and did not significantly affect the model fit ($R^2 \geq 0.90$ for both PACl and alum). Equation 5.17 can be simplified to:

$$C^* = \left(\beta G\theta\Gamma\phi^{2/3}\right)^{-1} \qquad (5.18)$$

where the coefficient, $\beta = 10^b$.

5.5 Results

The results from 136 experiments are shown in Figure 5.4 for a capture velocity of 0.12 $\frac{mm}{s}$ which is a conservatively designed lamellar settler capture velocity (Willis, 1978). The capture velocity is an input parameter to the data analysis model and model application can be generalized for a range of capture velocities between 0.1 $\frac{mm}{s}$ and 0.22 $\frac{mm}{s}$ as described below. The raw data for all influent turbidities, hydraulic residence times, and doses are shown in Figure 5.4 for both PACl and alum. The data has significant spread, but generally shows a negative slope, indicating that increased coagulant dose is positively correlated to turbidity removal.

PACl

Alum

Residual Turbidity, NTU

Residual Turbidity, NTU

PACl Dose in mol/L Al

Alum Dose in mol/L Al

+++ θ=1200s, 5 NTU
■■■ θ=1200s, 15 NTU
◆◆◆ θ=1200s, 50 NTU
●●● θ=1200s, 150 NTU
▲▲▲ θ=1200s, 500 NTU
××× θ=800s, 5 NTU
□□□ θ=800s, 15 NTU
◇◇◇ θ=800s, 50 NTU
ooo θ=800s, 150 NTU
△△△ θ=800s, 500 NTU

+++ θ=1200s, 5 NTU
■■■ θ=1200s, 15 NTU
◆◆◆ θ=1200s, 50 NTU
●●● θ=1200s, 150 NTU
▲▲▲ θ=1200s, 500 NTU
××× θ=800s, 5 NTU
□□□ θ=800s, 15 NTU
◇◇◇ θ=800s, 50 NTU
ooo θ=800s, 150 NTU
△△△ θ=800s, 500 NTU
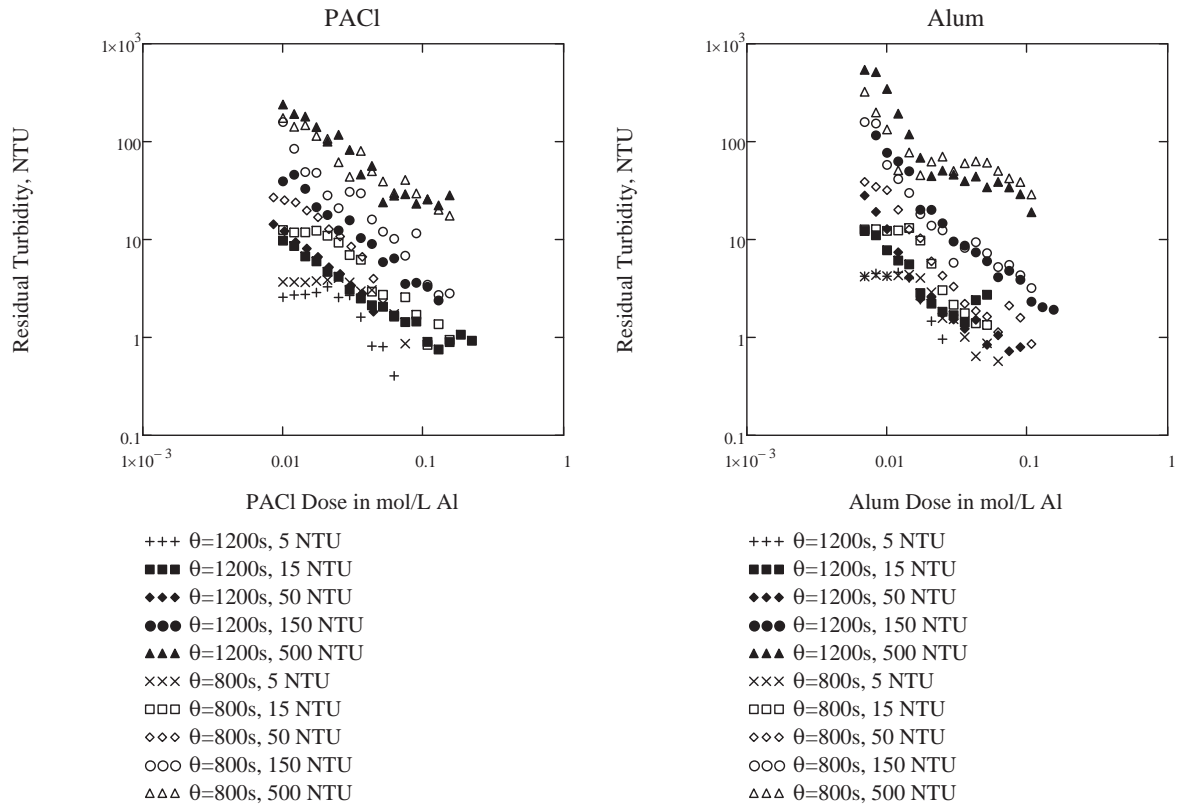
Figure 5.4: Residual turbidity as a function of coagulant dose for $V_{Capture} = 0.12 \frac{mm}{s}$

Transforming the residual turbidity by Equation 5.15 aggregates the data and complicated trends are seen between the different influent turbidities (Figure 5.5). Given the same coagulant dose the highest removal efficiency is obtained by samples with turbidities of 50 and 150 NTU. Higher and lower influent turbidities both perform more poorly. This optimal influent turbidity suggests that there are two competing mechanisms that cause performance to worsen for both very high and very low influent turbidities. The two competing mechanisms at a constant coagulant dose are the fractional coverage of clay that decreases with increasing influent turbidity and the floc volume fraction that increases with influent turbidity.

PACl

Alum

pC*

+++ θ=1200s, 5 NTU
■■■ θ=1200s, 15 NTU
◆◆◆ θ=1200s, 50 NTU
●●● θ=1200s, 150 NTU
▲▲▲ θ=1200s, 500 NTU
××× θ=800s, 5 NTU
□□□ θ=800s, 15 NTU
◇◇◇ θ=800s, 50 NTU
ooo θ=800s, 150 NTU
△△△ θ=800s, 500 NTU

+++ θ=1200s, 5 NTU
■■■ θ=1200s, 15 NTU
◆◆◆ θ=1200s, 50 NTU
●●● θ=1200s, 150 NTU
▲▲▲ θ=1200s, 500 NTU
××× θ=800s, 5 NTU
□□□ θ=800s, 15 NTU
◇◇◇ θ=800s, 50 NTU
ooo θ=800s, 150 NTU
△△△ θ=800s, 500 NTU

PACl Dose in mol/L Al

Alum Dose in mol/L Al
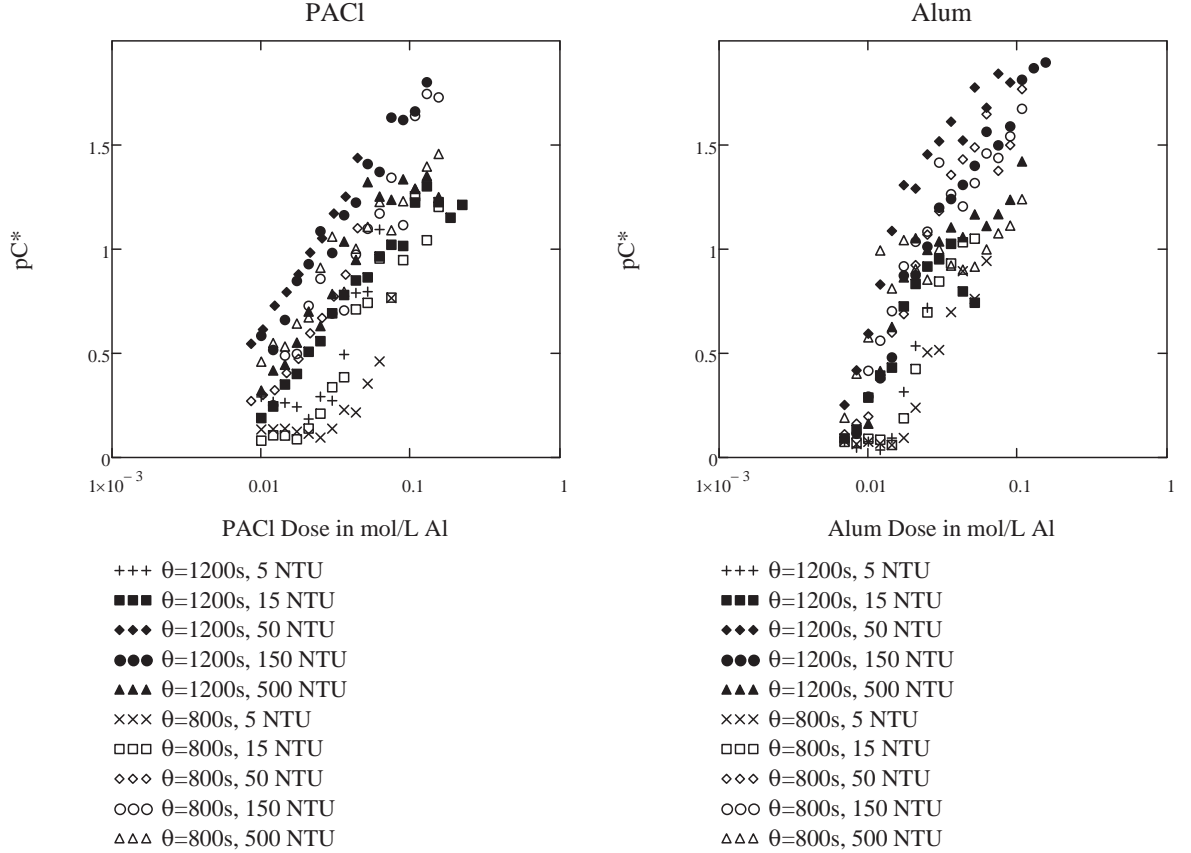
Figure 5.5: pC^* as a function of coagulant dose for $V_{Capture} = 0.12 \frac{mm}{s}$

When the coagulant dose in Figure 5.5 was replaced with $G\theta\Gamma\phi^{2/3}$ from Equation 5.18 the data collapses to a narrow band indicating that the composite independent parameter, $G\theta\Gamma\phi^{2/3}$, captures a large fraction of the trends present in the data (see Figure 5.6). The coefficient β was fit to the data by using the mean of the intercept for the lines with slope of 1 defined by each data point The data for very low effective collision potential ($\Gamma G\theta\phi^{2/3} < 0.2$ for PACl and $\Gamma G\theta\phi^{2/3} < 0.12$ for alum) was removed before calculating β to eliminate suspensions that had insignificant sedimentation during the experimental settling time. The flocs created at such low effective collision potentials all have settling velocities lower than the capture velocity and negligible removal of turbidity was observed.

The data analysis outputs β for each selected capture velocity (Table 5.1). The relationship between β and capture velocity is shown in Figure 5.7 and was

Table 5.1: Correlation coefficient, R^2, and fitted parameter, β, for PACl and Alum as a function of capture velocity. Sample size, N, is 133 for PACl and 136 for Alum.

$V_{Capture}$	β_{PACl}	R^2_{PACl}	β_{Alum}	R^2_{Alum}
$0.1\,mm/s$	4.37	0.93	6.99	0.90
$0.12\,mm/s$	3.65	0.92	5.82	0.89
$0.14\,mm/s$	3.12	0.91	4.99	0.88
$0.16\,mm/s$	2.73	0.90	4.37	0.88
$0.18\,mm/s$	2.43	0.90	3.88	0.88
$0.20\,mm/s$	2.19	0.85	3.49	0.84
$0.22\,mm/s$	1.99	0.83	3.18	0.84

modeled very well by an equation of the form $\beta = \frac{\eta_{Coag}}{V_{Capture}}$ (Equations 5.19 and 5.20).

$$\beta_{PACl} = \frac{\eta_{PACl}}{V_{Capture}}; \ R^2 = .999, \ N = 13 \tag{5.19}$$

$$\beta_{Alum} = \frac{\eta_{Alum}}{V_{Capture}}; \ R^2 = .997, \ N = 13 \tag{5.20}$$

where $\eta_{PACl} = 0.49\,\frac{mm}{s}$ and $\eta_{Alum} = 0.818\,\frac{mm}{s}$. The lower bound of the capture velocity range was set by the duration of settling in the experiments, and the upper bound is likely set by the maximum sedimentation velocity of the flocs given the velocity gradient in the flocculator.

To generalize the flocculation model within the range of tested capture velocities, Equations 5.19 and 5.20 were incorporated into Equation 5.18. Since surface coverage, Γ, is a function of the the coagulant dose , C_{Coag}, this relationship can be used to predict the dose required to reduce the settled water turbidity to a desired value for a sedimentation tank with a specified capture velocity (Equation 5.22). As an example, the PACl and alum doses required to achieve a settled turbidity of 3 NTU, a common influent turbidity for a rapid sand filter, are shown in Figure 5.8 for a range of influent turbidities and capture velocities.

$$C^* = \left(\frac{\eta_{Coag}}{V_{Capture}} G\theta\Gamma\phi^{2/3} \right)^{-1} \tag{5.21}$$

$$C_{Coag} = ln\left(1 - \left(\frac{C_{Influent}}{\frac{\eta_{Coag}}{V_{Capture}}C_{Settled}}\right)\frac{1}{G\theta}\left(\frac{\rho_{Clay}}{C_{Influent}}\right)^{\frac{2}{3}}\right)\frac{-d_{Coag}\pi\rho_{Coag}\left(1 + d_{Tube}SA_{Clay}\frac{C_{Influent}}{V_{Clay}\rho_{Clay}}\right)}{6d_{Tube}} + C_{Coag(aq)} \tag{5.22}$$

The model was validated by using it to predict residual turbidity for different experimental conditions than those used to obtain the model (i.e., different influent turbidity, velocity gradient, flocculation time, coagulant dose and capture velocity). The predicted residual turbidity and measured residual turbidity are compared in Figure 5.9.

5.6   Discussion

A mechanistically-based hydraulic flocculation model has been created and validated for laminar flows. The form and parameterization of the model led to several useful findings. The influence of coagulant dose on flocculation performance can be explained by the fractional coverage of the colloid surface without regard for previously hypothesized coagulation mechanisms (charge-neutralization, electrostatic patch, sweep floc, etc). The change in required coagulant dose for the range of capture velocities embodied in the design of downstream sedimentation tanks is predictable and is incorporated into the flocculation model, increasing its flexibility and utility.

The flocculation model utilizes experimental observations obtained over wide operational ranges for many parameters. The inherent dimensionless relationships embodied in the model are mechanistic and the model fits are well-correlated to the data. The predictive capability of the model is excellent. The reader is cautioned that some model assumptions may not hold for all applications. While the PACl aggregate diameter was experimentally measured, the aluminum hydroxide aggregate diameter was estimated; $100\,nm$ was chosen to maximize the R^2 value for the model fit. However, the model is not sensitive to this input; changing the diameter of precipitated aluminum hydroxide to $50\,nm$ or $150\,nm$ only reduced the R^2 by 0.06.

In contrast to rapid sand filtration where pC^* is linearly proportional to filter depth, the flocculation model definitively shows that pC^* is directly proportional to the log of the effective collision potential $\left(log\left(\Gamma G\theta\phi^{2/3}\right)\right)$. While a particle in a sand filter has an equal probability of being removed in the first and last centimeter of the filter, colloids are much more likely to be incorporated into a floc in the first centimeter of the flocculator than in the last centimeter. Because flocs incorporate water as they grow, the floc volume fraction increases with floc size and the frequency of collisions increases. Thus, the proportion of collisions that result in aggregation, must decrease as flocs grow. Selective removal of colloids with high coagulant surface coverage is hypothesized to contribute to the diminishing rate of turbidity removal. The adhesive properties of the coagulant do not change, but as the colloids aggregate, the most adhesive surfaces are preferentially buried within the growing floc. Furthermore, due to the random distribution of coagulant aggregates to the surface of the colloids during coagulation, some statistical portion of the colloids will have a lower fractional surface coverage of coagulant. These colloids would be more likely to remain unaggregated in flocculation because their ability to adhere was lower.

The fitted parameter, η_{Coag}, has units of velocity, therefore it must be a function of parameters that give units of length per time. It is hypothesized that η_{Coag} may be proportional to the mean sedimentation velocity of the suspension after coagulation and flocculation. Tse et al. (2011a) describe the influence of G on final floc sedimentation velocity and observed that residual turbidity tends to decrease as G decreases. This relationship merits additional research.

The flocculation model provides a fundamental basis for the non-stoichiometric relationship between coagulant dose and the suspended solids concentration of

the raw water. The five terms in flocculation equation set the interactions between raw water properties (ϕ and colloid surface area which contributes to Γ), coagulant size and dose (which also contribute to Γ), flocculator design ($G\theta$), and sedimentation tank design ($V_{Capture}$). In a given water treatment plant operating at constant flow rate the flocculator and sedimentation tank parameters are constant. An increase in turbidity causes an increase in ϕ, which improves C^*, and at constant coagulant dose causes a decrease in Γ, which decreases C^*. The competing influences of ϕ and Γ cause both very high and very low turbidity waters to be difficult to flocculate. High turbidity water is difficult to treat because the required coagulant dose becomes very large. Low turbidity water is hard to treat because ϕ is small and thus collisions are infrequent.

The important role of coagulant loss to reactor surfaces is characterized and provides insight into optimal flocculator geometry to reduce wall losses. Reactor geometry should minimize the surface area of the flocculator walls by using flow passages that are close to square. This is especially important for small scale hydraulic flocculators where distances between flocculator baffles are reduced and coagulant loss is more significant.

The form of the model indicates that increasing the residence time in the flocculator leads to quantifiable improvements in performance or a reduction in the coagulant demand. This information can be used to optimize reactor design, minimize costs, and forecast chemical costs. While not the focus of this study, the influence of sedimentation tank capture velocity on required coagulant dose is depicted in Figure 5.8. With this information, capture velocity can be chosen in the same way that hydraulic residence time in the flocculator can be chosen, by comparing construction costs and site considerations to coagulant costs.

It is noteworthy that the predictive success of the model is achieved without incorporating the charge of the colloids or coagulant. The lack of a stoichiometric relationship between raw water turbidity and required coagulant dose in these experiments suggested that surface charge neutralization was not a controlling factor in flocculation. There are also reports in the literature where successful flocculation has been achieved when particle surface charge had not been neutralized (Gao et al., 2005; Wu et al., 2007; Chu et al., 2008). The experimental data do not provide any evidence of a shift in particle removal that could be attributed to charge neutralization, as this effect would be expected to be reflected by a large incremental change in pC^* over a small incremental change in coagulant dose where charge neutralization occurs. In addition no decrease in pC^* was observed at high coagulant dose, as would be expected with charge reversal. Thus, inclusion of surface charge in the model was not justified by the data.

The model is a powerful predictor of flocculation behavior under the tested conditions. Further tests should be done to expand the reach of the model from laminar flow (bench-scale) flocculators to turbulent flow (field-scale) hydraulic flocculators. It is expected that the same mechanistic relationships will be present with the exception of G which is not expected to characterize turbulent flow flocculation. Flocculator properties characterized by G in laminar flow can be described by $\varepsilon^{1/3}$ in turbulent flow (Weber-Shirk and Lion, 2010).

97

Similarly, natural waters with varying water chemistry and colloid types should be tested to elucidate the impact of natural organic matter, pH, and alkalinity on flocculation performance. The importance of surface area as a coagulant sink suggests that small diameter particulate matter would be significant sinks for coagulant. In addition, complexation of added coagulant by natural dissolved organic matter can also act as a coagulant sink and increase the required dose. It is reasonable to believe that with additional testing this model could be the basis for flocculation design and operation for a wide range of hydraulic flocculators and source waters. Mechanistically based predictive models for flocculator design and operation are possible and merit further development for synthesis into scalable guidelines for engineers and plant operators.

5.7 References

Akers, R., Rushton, A., and Stenhouse, J. (1987). "Floc breakage: The dynamic response of the particle size distribution in a flocculated suspension to a step change in turbulent energy dissipation." *Chem. Eng. Sci.*, 42(4), 787 − 798.

Benschoten, J. E. V. and Edzwald, J. K. (1990). "Chemical aspects of coagulation using aluminum salts - I. Hydrolytic reactions of alum and polyaluminum chloride." *Water Res.*, 24(12), 1519–1526.

Bolton Point Water System (2012). "Drinking water quality report." *Report no.*, Southern Cayuga Lake Intermunicipal Water Commission.

Chu, Y. B., Gao, B. Y., Yue, Q. Y., and Wang, Y. (2008). "Investigation of dynamic processing on aluminum floc aggregation: Cyclic shearing recovery and effect of sulfate ion." *Sci. China, Ser. B: Chem.*, 51, 386–392.

Cleasby, J. (1984). "Is velocity gradient a valid turbulent flocculation parameter?." *J. Environ. Eng. (Reston, VA, U. S.)*, 110(5), 875–897.

Gao, B. Y., Chu, Y. B., Yue, Q. Y., Wang, B. J., and Wang, S. G. (2005). "Characterization and coagulation of a polyaluminum chloride (PAC) coagulant with high Al13 content." *J. Environ. Manage.*, 76(2), 143–147.

Hendricks, D. W. (2009). *Fundamentals of Water Treatment Unit Processes: Physical, Chemical, and Biological.* Taylor and Francis.

International Program on Chemical Safety (1998). "Aluminum hydroxide." *Report no.*

Kawamura, S. (1991). *Integrated design of water treatment facilities.* Wiley, New York.

Lin, J.-L., Chin, C.-J. M., Huang, C., Pan, J. R., and Wang, D. (2008). "Coagulation behavior of Al13 aggregates." *Water Res.*, 42(16), 4281–4290.

Owen, A. T., Fawell, P. D., Swift, J. D., Labbett, D. M., Benn, F. A., and Farrow, J. B. (2008). "Using turbulent pipe flow to study the factors affecting polymer-bridging flocculation of mineral systems." *Int. J. Miner. Process.*, 87(3-4), 90–99.

Schulz, C. R. and Okun, D. A. (1984). *Surface Water Treatment for Communities in Developing Countries.* John Wiley and Sons Inc., Great Britain.

The Great Lakes - Upper Mississippi River Board of State and Provincial Public Health and Environmental Managers (2007). "Recommended standards for water works." *Report no.*, Health Research Inc.

Tse, I. C., Swetland, K., Weber-Shirk, M. L., and Lion, L. W. (2011a). "Fluid shear influences on the performance of hydraulic flocculation systems." *Water Res.*, 45(17), 5412–5418.

Tse, I. C., Swetland, K., Weber-Shirk, M. L., and Lion, L. W. (2011b). "Method for quantitative analysis of flocculation performance." *Water Res.*, 45(10), 3075–3084.

Weber-Shirk, M. L. (2008). "An automated method for testing process parameters." *Report no.*, AguaClara Program at Cornell University.

Willis, R. M. (1978). "Tubular settlers-a technical review." *J. - Am. Water Works Assoc.*, June, 331–335.

Wu, X., Ge, X., Wang, D., and Tang, H. (2007). "Distinct coagulation mechanism and model between alum and high Al13-PACl." *Colloids Surf., A*, 305(1-3), 89–96.

Ye, C., Wang, D., Shi, B., Yu, J., Qu, J., Edwards, M., and Tang, H. (2007). "Alkalinity effect of coagulation with polyaluminum chlorides: Role of electrostatic patch." *Colloids Surf., A*, 294(1-3), 163–173.
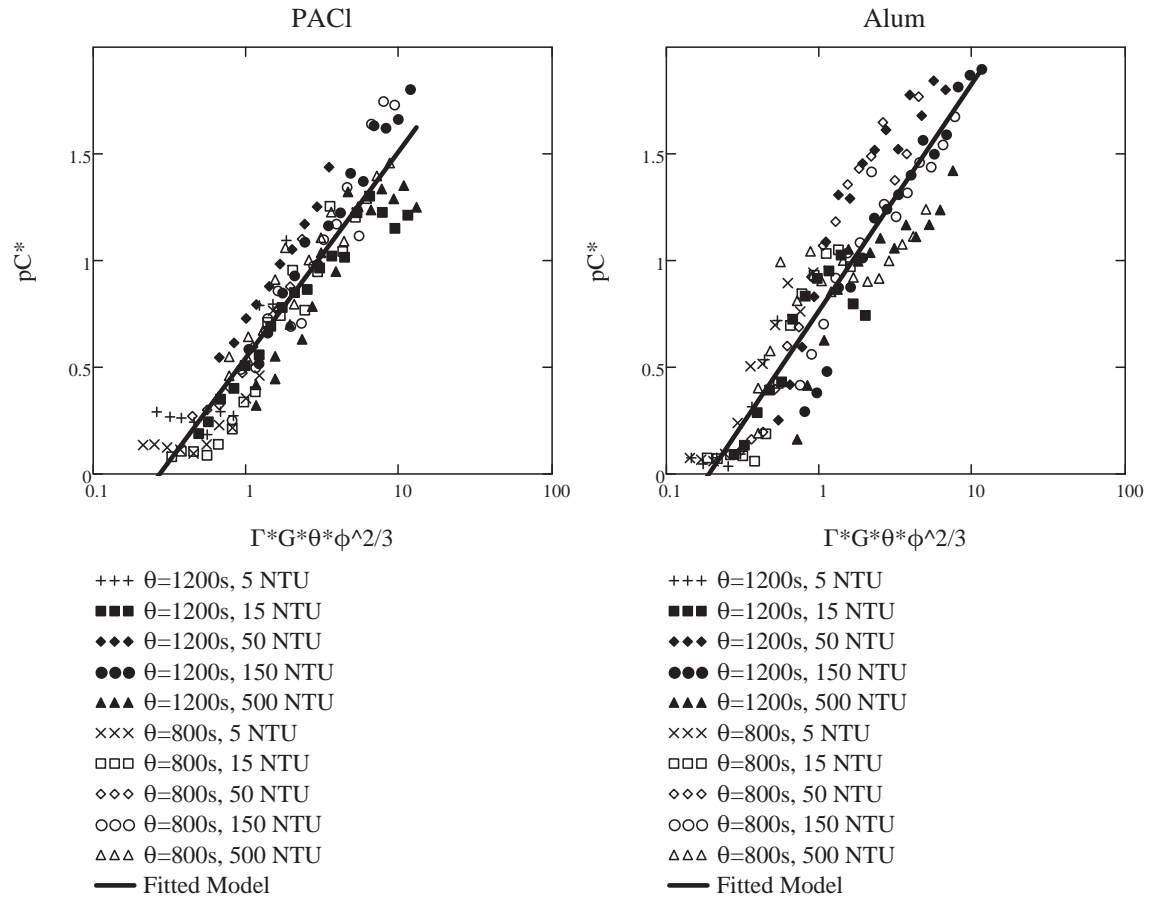
Figure 5.6: Model fit for pC^* as a function of effective collision potential for $V_{Capture} = 0.12 \frac{mm}{s}$. Sample size, N, is 136 for PACl and 140 for Alum. $R^2_{PACl} = 0.92$ and $R^2_{Alum} = 0.89$.
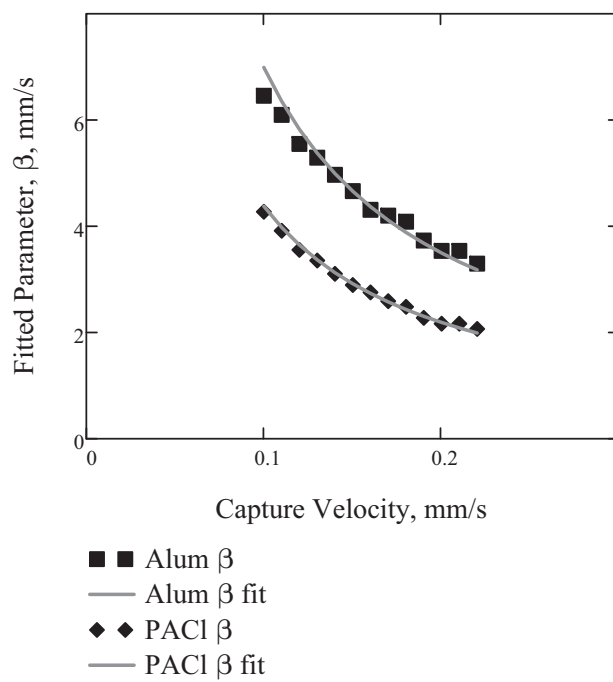
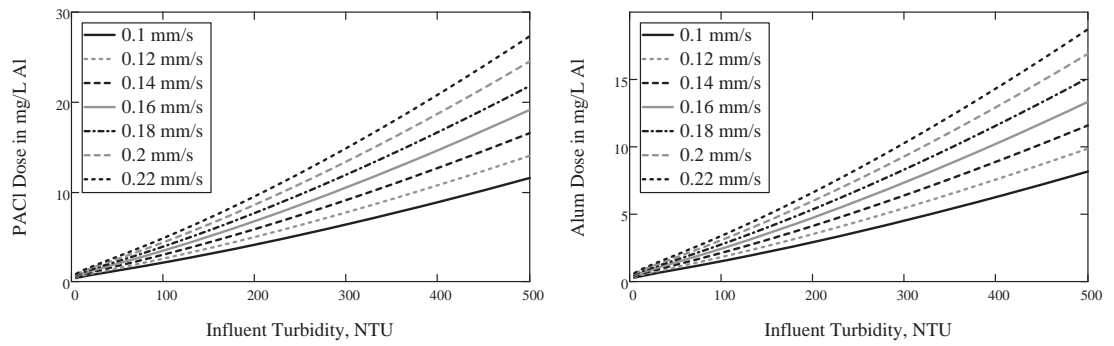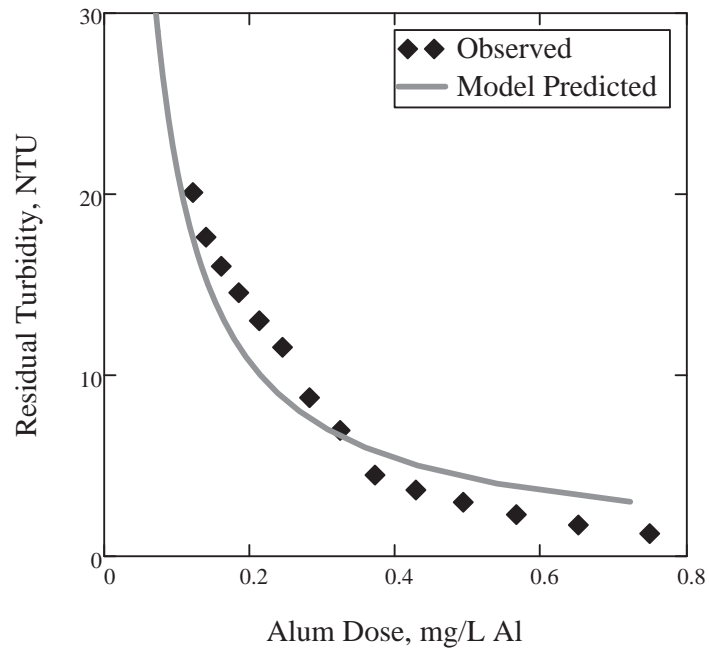Figure 5.7: Model parameters as a function of capture velocity.

Figure 5.8: Model predictions using coagulant dose needed to achieve a settled turbidity of 3 NTU as a function of influent turbidity for a range of capture velocities. $\theta = 1200\,s$, $C_{Settled} = 3\,NTU$.

a)

b)

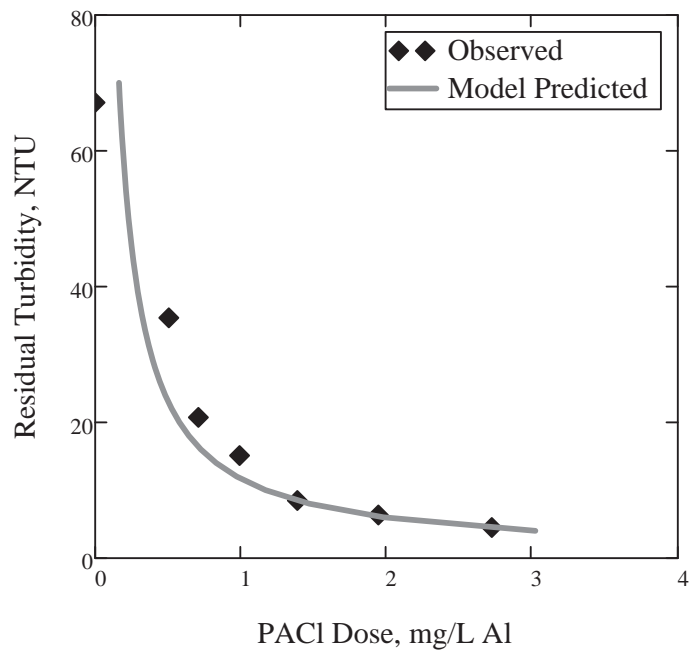Figure 5.9: Model validation using a) alum, $C_{Influent} = 30\,NTU$, $\theta = 1087\,s$, $G = 57.2\,s^{-1}$ for $V_{Capture} = 0.10\,\frac{mm}{s}$. $R^2 = 0.97$ and b) PACl, $C_{Influent} = 75\,NTU$, $\theta = 997\,s$, and $G = 63.3\,s^{-1}$ for $V_{Capture} = 0.22\,\frac{mm}{s}$. $R^2 = 0.99$

104

Chapter 6

Conclusions and Recommendations for Future Research

The AguaClara Program at Cornell University has a track record that demonstrates it provides innovations and improved designs to enhance the performance of the water treatment plants. Feedback from the laboratory and plant operators provides the impetus for new research questions and insights into on-going research.

One of the foremost hurdles in the development of AguaClara technology has been devising a method for accurately and precisely administering process chemicals while adhering to the fundamental AguaClara design constraint of creating simple, robust, sustainable solutions that do not rely on electricity. Modern water treatment plants have computerized control and precise metering pumps at their disposal. AguaClara designs also demand accurate metering. The author in conjunction with students in the AguaClara program has developed a Chemical Dose Controller (CDC) that utilizes gravity, hydrostatic pressure, and head loss to predictably meter process chemicals, such as aluminum sulfate or polyaluminum chloride (PACl) for coagulation, and chlorine for disinfection. The Linear Flow Orifice Meter invented by the AguaClara team compliments the linear CDC. The orifice meter provides accurate flow measurement of the plant flow rate and creates a linear relationship between depth of water in the entrance tank and plant flow rate. This linear response is used as an input to the linear CDC.

The existing design guidelines for gravity-powered hydraulic flocculators are empirical and are based on design parameters that are known to be incorrect for turbulent flow. The dynamics of how physical parameters affect flocculation are also not well understood. The goal of AguaClara's flocculation research is to determine the parameters (such as optimal energy dissipation rate, hydraulic residence time, coagulant dose, conditions for rapid mix, etc.) that will produce

quickly settling flocs for a variety of influent water qualities and to provide rational mechanistically-based guidelines for design of flocculation systems. Through extensive testing with the bench-scale FReTA apparatus, a predictive flocculation model was created which uses directly observable parameters to predict flocculation performance. The potential applications of this model cannot be understated. The strong correlation between turbidity removal (pC^*) and effective collisions ($\Gamma G \theta \phi^{2/3}$) in a model which is based on 136 experiments and includes only one fitted parameter is the basis for its commendation. Future experiments concerning the effect of organic matter on coagulant behavior, for example, could allow the model to be generalized to a wide array of source waters.

While the specific conditions tested in the research presented here are relatively common and the knowledge gained is applicable, the true value in these systems are their flexibility. The scalable design algorithms for the LFOM and LCDC posted online make those systems available and useful to billions of people. The FReTA apparatus and data processing system can be used to test many types of influent conditions, flocculator designs, and sedimentation tank geometries (via capture velocity). The basic mechanisms of coagulant behavior are much closer to being fully understood. Finally, the robust flocculation model with it's strong fit to an extensive data set and few fitted parameters will change the collective understanding of flocculation and permit optimization of flocculator design.